

## INFORMATION TO USERS

This manuscript has been reproduced from the microfilm master. UMI films the text directly from the original or copy submitted. Thus, some thesis and dissertation copies are in typewriter face, while others may be from any type of computer printer.

**The quality of this reproduction is dependent upon the quality of the copy submitted.** Broken or indistinct print, colored or poor quality illustrations and photographs, print bleedthrough, substandard margins, and improper alignment can adversely affect reproduction.

In the unlikely event that the author did not send UMI a complete manuscript and there are missing pages, these will be noted. Also, if unauthorized copyright material had to be removed, a note will indicate the deletion.

Oversize materials (e.g., maps, drawings, charts) are reproduced by sectioning the original, beginning at the upper left-hand corner and continuing from left to right in equal sections with small overlaps. Each original is also photographed in one exposure and is included in reduced form at the back of the book.

Photographs included in the original manuscript have been reproduced xerographically in this copy. Higher quality 6" x 9" black and white photographic prints are available for any photographs or illustrations appearing in this copy for an additional charge. Contact UMI directly to order.

**UMI<sup>®</sup>**

Bell & Howell Information and Learning  
300 North Zeeb Road, Ann Arbor, MI 48106-1346 USA  
800-521-0600



# Characterization of the Physical Properties of Iron Polyimide Nanocomposites

---

A Dissertation

Presented to The Faculty of the Department of Physics  
The College of William and Mary

In Partial Fulfillment  
Of the Requirements for the Degree of  
Doctor of Philosophy

---

By

**Russell A. Wincheski**

December 1999

UMI Number: 9961704

**UMI<sup>®</sup>**

---

UMI Microform 9961704

Copyright 2000 by Bell & Howell Information and Learning Company.

All rights reserved. This microform edition is protected against  
unauthorized copying under Title 17, United States Code.


---

Bell & Howell Information and Learning Company  
300 North Zeeb Road  
P.O. Box 1346  
Ann Arbor, MI 48106-1346

## APPROVAL SHEET

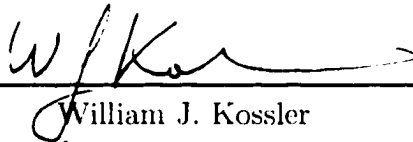
This dissertation is submitted in partial fulfillment  
of the requirements for the degree of

Doctor of Philosophy.

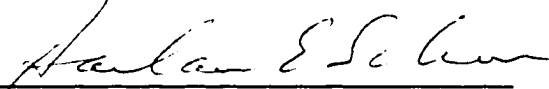


Russell A. Wincheski

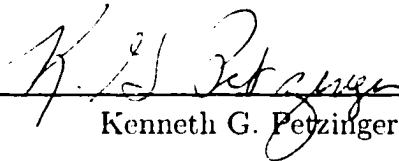
Approved, December 1999



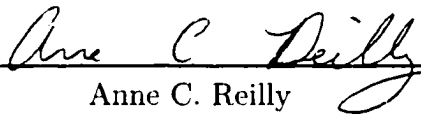
William J. Kossler



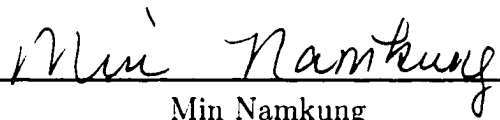
Harlan E. Schone



Kenneth G. Petzinger



Anne C. Reilly



Min Namkung

National Aeronautics and Space Administration

# Contents

<b>List of Tables</b>	<b>v</b>
<b>List of Figures</b>	<b>vi</b>
<b>Abstract</b>	<b>ix</b>
<b>Chapter 1 Introduction</b>	<b>2</b>
<b>Chapter 2 Tunneling Magnetoresistance</b>	<b>7</b>
2.1 Original Model . . . . .	7
2.2 Connection to Electronic Band Structure . . . . .	9
2.3 Barrier Height Effects . . . . .	12
2.4 Barrier Thickness Effects . . . . .	15
<b>Chapter 3 Variable Range Hopping</b>	<b>24</b>
3.1 Electronic Conduction and Localization . . . . .	24
3.2 Hopping Conduction . . . . .	27
3.3 Variable Range Hopping in Granular Metals . . . . .	29
<b>Chapter 4 Computer Simulation</b>	<b>33</b>
4.1 Two-Dimensional Percolation Simulation . . . . .	34
4.2 Three-Dimensional Percolation Simulation . . . . .	39
4.3 Resistance Calculations in Iron Polyimide Composites . . . . .	43
4.4 Model and Simulation Results for Tunneling Magnetoresistance . . . . .	49
<b>Chapter 5 Experiment</b>	<b>53</b>
5.1 Sample Fabrication Procedure . . . . .	54
5.2 Optical and Scanning Electron Microscopy . . . . .	56

5.3	Magnetic Force Microscopy Measurement System . . . . .	57
5.4	Magnetization Measurement System . . . . .	64
5.5	Magnetoresistance Measurement System . . . . .	64
5.6	Experimental Setup for Temperature Dependence Measurements . . .	66
5.7	Material Processing through High Energy Ball Milling . . . . .	68
<b>Chapter 6 Results and Discussion</b>		<b>70</b>
6.1	Microscopy Studies . . . . .	71
6.2	Magnetization Data . . . . .	82
6.3	Magnetoresistance Data . . . . .	84
6.4	Variable Range Hopping . . . . .	88
6.5	Temperature Dependence of Magnetoresistance . . . . .	92
6.6	Material Processing Results . . . . .	94
<b>Chapter 7 Summary and Conclusions</b>		<b>101</b>
7.1	Summary . . . . .	101
7.2	Future Perspectives . . . . .	103
<b>Bibliography</b>		<b>104</b>
<b>Vita</b>		<b>109</b>

# List of Tables

2.1	Estimates of the Fermi wave vectors for the $d_i$ like electrons and the calculated spin polarization from equation (2.5). . . . .	11
2.2	Calculated conductance variation between ferromagnetic and antiferromagnetic spin alignments in iron across a tunneling gap. . . . .	20
4.1	Calculated results of average percolation threshold and standard deviation for trigonal lattices. . . . .	38
4.2	Calculated results of average percolation threshold and standard deviation for hexagonal close-packed lattices. . . . .	42
4.3	Calculated tunneling magnetoresistance in two dimensional iron polyimide composites at the percolation threshold. . . . .	51
6.1	Magnetization data of iron polyimide composites with varying Fe volume concentration. . . . .	84
6.2	Room temperature resistivity and magnetoresistance at 0.5 Tesla of iron polyimide composite samples. . . . .	85
6.3	Magnetization data of 20% iron powders with varying ball milling times. . . . .	96

# List of Figures

2.1	Calculated band structure of Fe. The electron states which correspond to the $d_i$ electrons are drawn in bold. $E_f$ is indicated by the dashed line.	10
2.2	Simplified energy level diagram for 2 band ferromagnet with parabolic energy bands. . . . .	11
2.3	Schematic potential diagram for tunneling between two metallic ferromagnets separated by an insulating barrier. The angle between the molecular fields in the two ferromagnets is given by $\theta$ . . . . .	13
2.4	Plot of conductance ratio $\frac{\Delta G}{G}$ for iron-barrier-iron tunneling as a function of barrier height and thickness . . . . .	21
2.5	Plot of conductance ratio for iron-insulator-iron tunneling as a function of barrier thickness at a barrier height of 4.31 eV. . . . .	22
3.1	Electron density of states for normal metal (a) and insulator (b). . . .	25
3.2	Anderson localized states inside conduction band. . . . .	26
4.1	Percolation simulation results for 50x50 trigonal array. Calculated percolation threshold $p_c = 50.5\%$ . . . . .	35
4.2	Percolation simulation results for 50x50 trigonal array. Calculated percolation threshold $p_c = 49.1\%$ . . . . .	36
4.3	Percolation simulation results for 50x50 trigonal array. Calculated percolation threshold $p_c = 49.96\%$ . . . . .	37
4.4	Graph of calculated average percolation threshold and standard deviation for trigonal lattices. . . . .	38
4.5	HCP lattice composed of five stacked 10x10 trigonal lattices. . . . .	40
4.6	Percolation simulation results for 4x4x4 HCP array. Calculated percolation threshold $p_c = 28.12\%$ . . . . .	41

4.7	Percolation simulation results for 4x4x4 HCP array. Calculated percolation threshold $p_c = 18.75\%$ . . . . .	41
4.8	Graph of calculated average percolation threshold and standard deviation for HCP lattices. . . . .	42
4.9	Mesh current analysis for 3x3 trigonal array. . . . .	44
4.10	Mesh current analysis for 3x3 trigonal array with external drive. . . .	45
4.11	Percolation simulation for 20x20 trigonal lattice. Calculated $p_c = 52.5\%$ and calculated $R/R_{nn} = 13.4$ . . . . .	47
4.12	Percolation simulation for 20x20 trigonal lattice. Calculated $p_c = 48.25\%$ and calculated $R/R_{nn} = 19.5$ . . . . .	48
4.13	Calculated resistance as a function of grid size. . . . .	49
4.14	Calculated magnetoresistance as a function of grid size. . . . .	52
5.1	Experimentally measured density and full packing density as a function of iron volume percent for iron polyimide composite samples . . . . .	56
5.2	Schematic diagram of experimental setup for magnetic force microscopy. 58	
5.3	Amplitude and phase of cantilever oscillation as a function of drive frequency. . . . .	61
5.4	Calculated MFM frequency shift for 100 nm diameter iron particle with $\vec{M}$ perpendicular to surface. . . . .	63
5.5	Calculated MFM frequency shift for 100 nm diameter iron particle with $\vec{M}$ parallel to surface. . . . .	64
5.6	Experimental setup for magnetization measurements with vibrating sample magnetometer. . . . .	65
5.7	Simplified experimental setup for magnetoresistance measurements. . .	65
5.8	Experimental setup for measurement of temperature dependence of magnetoresistance. . . . .	67
6.1	Optical micrograph of 20% Fe volume percent composite. . . . .	71
6.2	High magnification optical micrograph of 20% Fe volume percent composite. . . . .	72
6.3	SEM and EDS images of iron polyimide composite. . . . .	73
6.4	Scanning probe topographic and magnetic force images for 34% Fe Vol. sample. External field applied perpendicular to sample surface. . . . .	74
6.5	Optical and magnetic force images for 20% Fe Vol. sample. MFM data acquired in absence of external field. . . . .	76

6.6	Magnetic force image of 20% Fe Vol. sample over $35^2\mu\text{m}^2$ area with 150 nm lift-off. . . . .	77
6.7	Magnetic force image of 20% Fe Vol. sample over $15^2\mu\text{m}^2$ area with 100 nm lift-off. . . . .	78
6.8	Magnetic force image of 20% Fe Vol. sample over $2.5^2\mu\text{m}^2$ area with 75 nm lift-off. . . . .	79
6.9	Magnetic force image and line scan across single particle identified in Figure 5.11. . . . .	80
6.10	Identification of closely spaced nanophase iron particles in iron polyimide composite with 20% Fe Vol. . . . .	81
6.11	Magnetization curves for iron polyimide composite samples with varying Fe volume percentage. . . . .	83
6.12	Hysteresis loop for 20% Fe Vol. composite sample. . . . .	83
6.13	Magnetoresistance curves for iron polyimide composite samples. . . . .	86
6.14	Magnetization and magnetoresistance for 20% Vol. Fe composite sample. . . . .	88
6.15	Resistivity versus temperature for iron polyimide composite samples. . . . .	89
6.16	Curve fit of the temperature dependence of resistivity for 20% iron sample. . . . .	91
6.17	Effect of sample orientation on measured magnetoresistance. . . . .	92
6.18	Temperature dependence of magnetoresistance for iron polyimide composite with 20% Fe Vol. . . . .	95
6.19	Optical micrographs of milled and unmilled 20% Fe composite samples. . . . .	97
6.20	Magnetoresistance of milled and unmilled 20% Fe composite samples. . . . .	98
6.21	Low field magnetoresistance of milled and unmilled 20% Fe composite samples. . . . .	99

# Abstract

The discovery of tunneling magneto-resistance has led to a great deal of interest in the study of ferromagnet-insulator-ferromagnet (FIF) systems due to potential sensor and magnetic storage applications. An analysis of the band structure of the 3d ferromagnets shows that the conduction electrons become spin polarized by the molecular field. The transmission coefficient of these electrons across a tunneling gap therefore depends upon the relative alignment of the molecular field between the two ferromagnets.

In this work the manufacture of such tunneling gaps through compression molding of powdered ferromagnetic iron with a high performance polyimide has been studied for the first time. The percent change in the resistance with applied magnetic field depends critically on the volume percentage of ferromagnetic material in the composite. A peak in the tunneling magnetoresistance (TMR) occurs at a volume concentration just beneath the percolation threshold of the ferromagnetic material. The change in resistance relative to the resistance at zero field,  $\Delta R/R_0$ , obtains a room temperature peak value of -4.5% at 20% iron volume concentration.

Granular conducting systems near the percolation threshold are also subject to variable range hopping (VRH) conduction. The charging energy of small metallic grains results in an energy barrier for the acceptance of an additional electron. Electronic conduction requires thermal activation over this barrier along with tunneling through the insulating regime. The result of these two combined processes is a temperature dependent tunneling distance and a conductivity of the form  $\ln \sigma \propto T^{-x}$ , with  $1/4 \leq x \leq 1/2$ .

The theoretical development and experimental measurements of TMR and VRH in iron polyimide nanocomposites are thoroughly developed and analyzed in this work. Ferromagnet particle size and band structure effects on TMR are also explored in an effort to optimize the material for sensor applications.

Characterization of the Physical Properties of Iron Polyimide  
Nanocomposites

# Chapter 1

## Introduction

In the classical limit conduction across a system containing randomly situated conducting particles in an insulating matrix will occur only when a continuous cluster of the conducting particles spans the system. Percolation theory provides a tool for the study of such systems [1]. The volume concentration at which a spanning cluster is formed across an infinite system is called the percolation threshold,  $p_c$ . Below this critical concentration there will be no conducting paths across the system so that the material will be an insulator. Experimental measurements on iron polyimide composites confirm this general behavior. Increasing the volume concentration of the fine iron particles across the percolation threshold causes the conductivity of the composite to change by several orders of magnitude. The system, however, continues to conduct beneath  $p_c$ . Quantum mechanical tunneling across small insulating gaps allows electrons to continue to flow across the system. Of particular interest is the case when the conducting particles are also ferromagnetic. These systems have been studied since 1975, when Julliere first showed that the transmission coefficient for this tunneling process varies with the angle between the magnetic moments of the ferromagnets on either side of the barrier [2]. The conduction across the gap decreases

with increasing angle between the moments. In other words, the conduction is a maximum when the spins of the majority electrons are aligned and is a minimum when the moments of the two ferromagnets are antiparallel. This general result has been verified repeatedly and the theory of the conduction mechanism more fully developed as interest in the phenomenon has grown [3-12]. The search for a tunneling magnetoresistance sensor, in which a natural antiferromagnetic alignment can be overcome by a small external field, is now well under way. In such devices an external field is detected by a sharp decrease in the resistance of the sensor.

Production and optimization of tunneling magnetoresistance (TMR) devices have been focused on thin film materials [7-10], where careful fabrication techniques have led to room temperature TMR values ( $\Delta R/R_0$ ) of greater than 20% [10]. Granular TMR devices have also been explored through cosputtering a ferromagnetic material with an insulator [11, 12]. This technique has produced much more modest room temperature TMR values of approximately 0.6% for Ni based systems and 4.5% for Co based systems [12]. An alternate method of production of TMR junctions first explored here is compression molding of fine ferromagnetic powders in a nonconducting polyimide matrix. At a volume concentration of the ferromagnetic material just beneath the percolation threshold tunneling gaps exist throughout the bulk material. In the completely demagnetized state the electron spins will be randomly oriented. The presence of an external field, however, will create a favored magnetization direction. As the magnetic moments rotate to this lower energy state the resistance of the material decreases. Advantages of compression molded TMR devices over sputtered systems include lowered production cost and the possibility of better control of some fabrication variables, including grain size and molecular concentration of constituent materials.

In order to investigate the possible applications of TMR devices manufactured through compression molding a detailed study of the physical properties of compres-

sion molded iron polyimide composites has been performed. Samples were fabricated by compression molding micron sized iron particles with a high performance polyimide [13] in powdered form. The distribution of the iron particles throughout the composite was then studied with various microscopy techniques, including optical, scanning electron, atomic force, and magnetic force. These microscopy studies verified the required interparticle distances of tens of nanometers for samples with iron volume concentrations near the percolation threshold.

The electronic transport properties of the samples, as a function of iron volume fraction, was determined through 4 lead resistivity measurements. Measurements as a function of applied magnetic field confirmed TMR for samples with iron volume concentrations near the percolation threshold. A peak room temperature TMR of 4.5% was recorded for a sample containing 20% iron volume concentration, just beneath the predicted percolation threshold of 20.1%. Lowering the iron volume concentration leads to a decrease in the TMR to approximately 3% for 15% iron volume concentration as the thickness of the average tunneling gap increases. Increasing the volume concentration of iron above the percolation threshold again lowers the TMR. This is due to the formation of percolating paths across the system acting in parallel with the paths containing tunneling gaps. For iron volume concentrations above 60% the magnetoresistance of the system changes sign as bulk anisotropic magnetoresistance begins to dominate.

Measurements of the conductivity of the composites as a function of temperature verified the existence of variable range hopping conduction. The charging energy of individual iron grains in the composite produces a barrier for the acceptance of additional electrons. Thermal activation over this barrier is required in addition to tunneling through the insulating gap. The result of these two combined processes is a temperature dependence of the conductivity of the form,  $\ln \sigma \propto T^{-x}$ , with  $1/4 \leq x \leq 1/2$ , which has been observed for samples near the percolation

threshold [14, 15].

As the iron volume concentration increases, percolating paths across the system are formed and begin to dominate the conduction mechanism. This is observed in the temperature dependence of the resistivity as a function of iron volume concentration. The temperature dependence makes a transition from the variable range hopping form given above to that expected for a bulk metal, with the conductivity increasing with decreasing temperature as scattering due to phonon vibrations are inhibited.

In this dissertation the theory of both tunneling magnetoresistance and variable range hopping in iron-insulator composites are thoroughly developed. Percolation theory is used to define the critical concentration around which these effects are expected in the randomly mixed samples of the present study. These theories are then tied together in a computer simulation in order to predict the physical properties of iron polyimide nanocomposites.

In the following chapters the theory of the electronic conduction mechanisms introduced above are fully developed. A computer model based upon the developed theory is then presented and used to predict some of the transport properties of iron-insulator composite systems. Of particular interest in these calculations will be the electrical resistance of the material at the percolation threshold and the change in this resistance caused by an external magnetic field.

The theoretical and modeling results are followed by experimental data, beginning with the detailed sample preparation and fabrication procedure. Experimental measurements of the density, particle size and distribution, interparticle separation distances, magnetization, resistivity, and magnetoresistance are then presented for samples with Fe volume concentrations of 15, 20, 23, 34, 44, 54, and 64%. In addition, the temperature dependencies of the magnetization, resistivity and magnetoresistance are experimentally determined. A discussion of the experimental results based upon the previously developed theoretical background is presented.

A summary of this dissertation is presented in the final chapter. Conclusions are also drawn as to the potential of iron polyimide nanocomposites for magnetic field sensing and digital storage applications. Areas of future study that could improve the sensing capabilities of compression molded TMR devices beyond that which is presented here are also suggested.

# Chapter 2

## Tunneling Magnetoresistance

The basis for the theory of TMR begins with the work of Julliere [2] in the 1970's and is followed shortly thereafter by M.B. Stearns [3], J.C. Slonczewski [4], and most recently by J.M. MacLaren [5]. Each of these authors considers, to a heightening degree of complexity, the transmission coefficient of a spin polarized electron across a potential barrier. In this chapter the theory of tunneling magnetoresistance will be developed based upon the work of these authors and specialized to the iron polyimide nanocomposites of the present study.

### 2.1 Original Model

The theory of tunneling magnetoresistance was proposed by Julliere [2] based upon the superconductor-insulator-ferromagnet tunneling work of Tedrow and Meservey [16,17]. The hypothesis of spin conservation across a tunneling gap was invoked to yield a relationship with the conductance proportional to the product of some effective tunneling density of states in each spin channel. Julliere used the fraction of conduction electrons whose magnetic moments are aligned in the direction of the

external field as this effective tunneling density of states. The variables  $a$  and  $a'$  are used to represent this density of states in the first and second ferromagnets respectively. The conductance for parallel magnetization of the two ferromagnets is then given by summing the majority to majority and minority to minority contributions and can be written as:

$$G_{\parallel} \propto aa' + (1 - a)(1 - a') \quad (2.1)$$

Similarly, the conductance for antiparallel magnetization is given by summing the majority to minority and minority to majority contributions:

$$G_{\#} \propto a(1 - a') + a'(1 - a) \quad (2.2)$$

The change in conductance between parallel and antiparallel spin alignments relative to the conductance of the parallel alignment is then:

$$\begin{aligned} \frac{\Delta G}{G} &= \frac{G_{\parallel} - G_{\#}}{G_{\parallel}} = \frac{[aa' + (1 - a)(1 - a')] - [a(1 - a') + a'(1 - a)]}{aa' + (1 - a)(1 - a')} \\ &= \frac{(2aa' - a - a' + 1) - (a + a' - 2aa')}{2aa' - a - a' + 1} \\ &= \frac{4aa' - 2a - 2a' + 1}{2aa' - a - a' + 1} \\ &= \frac{2(4aa' - 2a - 2a' + 1)}{2(2aa' - a - a' + 1)} \\ &= \frac{2(2a - 1)(2a' - 1)}{1 + (2a - 1)(2a' - 1)} \\ &= \frac{2PP'}{1 + PP'} \end{aligned} \quad (2.3)$$

Here  $P = (2a - 1)$  and  $P' = (2a' - 1)$  are the conduction electrons spin polarizations of the two ferromagnetic materials. Tedrow and Meservey [17] have calculated this spin polarization for many ferromagnetic materials based upon superconductor-insulator-ferromagnet tunneling experiments. The value they quote for iron is  $P = 44\%$ . Based upon equation (2.3), this corresponds to a conductance variation  $\Delta G/G = 32\%$ .

## 2.2 Connection to Electronic Band Structure

M.B. Stearns [3] expanded upon the Julliere theory by making a connection between the spin polarization of the 3d ferromagnets and the band structure of the itinerant d-like,  $d_i$ , electrons. The calculated band structure of the majority and minority spin electrons is shown in Figure 2.1 [18]. Note the parabolic, free electron like structure of the bands which cross the Fermi energy level. These bands correspond to the  $d_i$  electrons with effective mass of about that of a free electron. This leads to the simplifying approximation of treating the  $d_i$  Fermi surfaces as spheres of radius  $k_f$ . The energy level diagram for tunneling between two ferromagnets in this approximation is given in Figure 2.2. A physical interpretation of the quantity  $a$  of Julliere and Tedrow et al. [2, 16, 17] is thus given by:

$$a = k_f^\uparrow / (k_f^\uparrow + k_f^\downarrow) \quad (2.4)$$

and the spin polarization  $P = (2a - 1)$  is:

$$P = (k_f^\uparrow - k_f^\downarrow) / (k_f^\uparrow + k_f^\downarrow) \quad (2.5)$$

The treatment given by Stearns has reduced the problem of finding the change in conductance for tunneling between parallel and antiparallel magnetizations to that of finding the Fermi surface wave vectors of the majority and minority electrons. Table 2.1 shows the calculated results for Fe, Ni (in units of  $\frac{2\pi}{a}$ ) and Co (in units of  $\frac{2\pi}{a\sqrt{3}}$ ), where  $a$  is the lattice constant of the metal. [3, 18]. The results for the spin polarizations are in close agreement with the experimental results of Tedrow and Meservey who found  $P_{Fe} = 44\%$  and  $P_{Co} = 34\%$  [17].

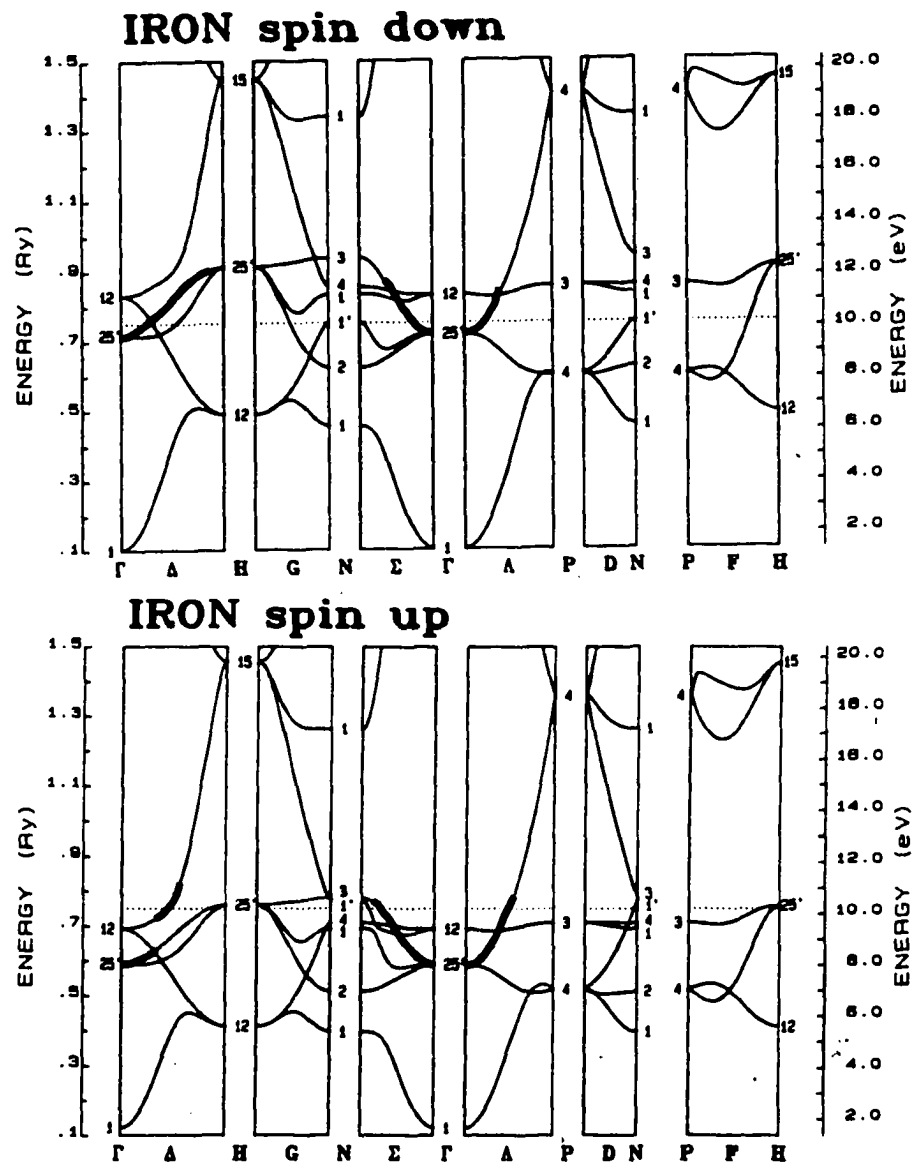


Figure 2.1: Calculated band structure of Fe. The electron states which correspond to the  $d_i$  electrons are drawn in bold.  $E_f$  is indicated by the dashed line.

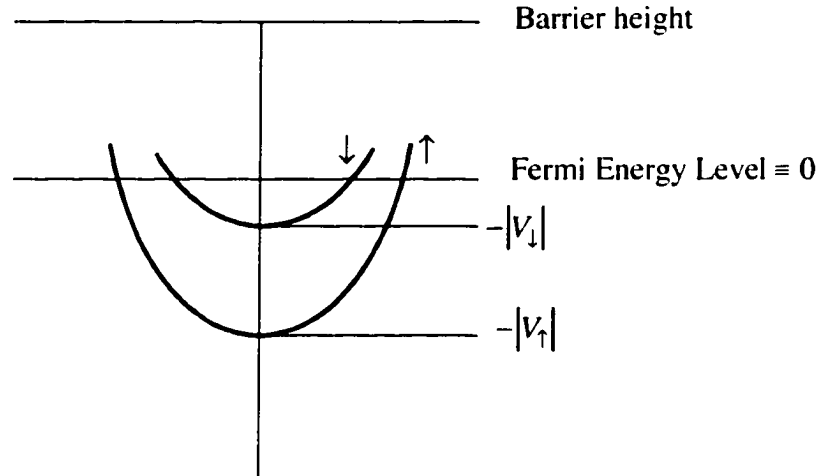


Figure 2.2: Simplified energy level diagram for 2 band ferromagnet with parabolic energy bands.

Table 2.1: Estimates of the Fermi wave vectors for the  $d_i$  like electrons and the calculated spin polarization from equation (2.5).

	$k_f^{\downarrow}$	$k_f^{\uparrow}$	Calculated $P$
Fe	0.5	0.19	0.45
Ni	0.65	0.53	0.10
Co	0.9	0.45	0.33

## 2.3 Barrier Height Effects

The theory of tunneling magneto-resistance set forth above still appears inadequate. A major inconsistency is the invariance of the barrier effects on the change in conductance due to the relative spin alignments across the barrier. The work of Slonczewski [4] helps to remedy this problem. Slonczewski considers two ferromagnetic conductors separated by a plane nonmagnetic barrier, and solves for the quantum mechanical tunneling coefficient. The geometry of the problem is shown in Figure 2.3.

Based upon the results of Stearns, the free electron approximation is again used for the spin polarized conduction electrons inside each ferromagnet. The effective one-electron Hamiltonian can then be written:

$$H_{\xi} = -\frac{1}{2} \left( \frac{d}{d\xi} \right)^2 + U(\xi) - \vec{h}(\xi) \cdot \vec{\sigma} \quad (2.6)$$

Here the system of units incorporates unit electron mass and unit Planck constant.  $U$  is the potential energy.  $\vec{h}$  is the molecular field, and  $\vec{\sigma}$  the Pauli spin operator. Considering a spin up incident plane wave having unit particle flux in ferromagnet 1, the solution to the Hamiltonian in each layer is given by the following wave functions:

$$\begin{aligned} \psi_{11} &= r_1 e^{-ik_1 \xi} \\ \psi'_{\uparrow 1} &= k_{\uparrow}^{-1/2} e^{ik_1 \xi} + r_{\uparrow} e^{-ik_1 \xi} \\ \psi_{\sigma b} &= A_{\sigma} e^{-\kappa \xi} + B_{\sigma} e^{\kappa \xi} \\ \psi_{\sigma 2} &= t_{\sigma} e^{ik_{\sigma}(\xi-d)} \end{aligned} \quad (2.7)$$

Here  $\sigma = \uparrow, \downarrow$ , and  $r_{\uparrow}, r_{\downarrow}, A_{\sigma}, B_{\sigma}$ , and  $t_{\sigma}$  are coefficients to be determined by matching the wave functions and derivatives at the boundaries. The change in spin quantization

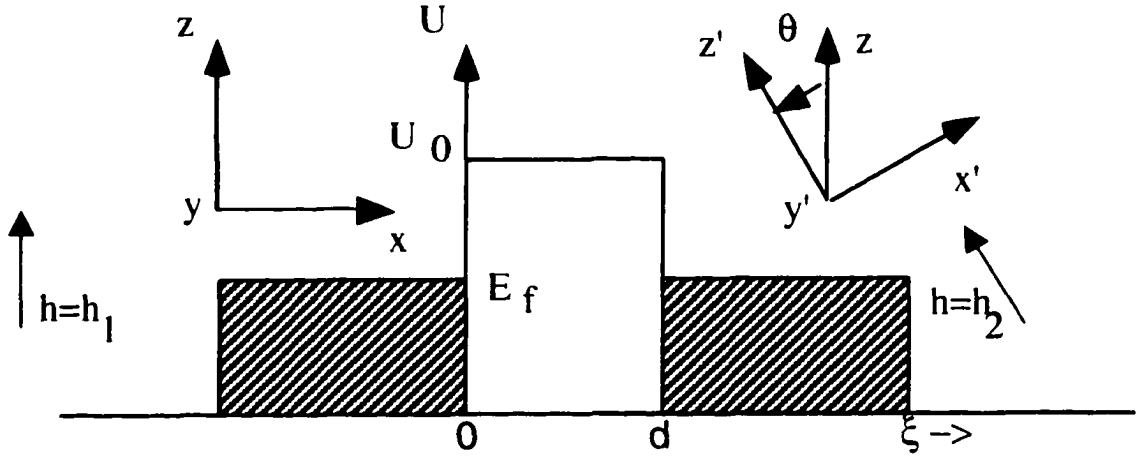


Figure 2.3: Schematic potential diagram for tunneling between two metallic ferromagnets separated by an insulating barrier. The angle between the molecular fields in the two ferromagnets is given by  $\theta$ .

direction at  $\xi = d$  requires that the wave functions satisfy the spinor transformations

$$\psi'_{1b} = \psi_{12} \cos(\theta/2) + \psi_{12} \sin(\theta/2) \quad (2.8)$$

$$\psi'_{1b} = -\psi_{12} \sin(\theta/2) + \psi_{12} \cos(\theta/2)$$

with similar relationships for the derivatives.

The set of equations to be solved for the unknown coefficients, in matrix notation, is

$$\begin{pmatrix} -1 & 0 & 1 & 0 & 1 & 0 & 0 & 0 \\ ik_{\uparrow} & 0 & -\kappa & 0 & \kappa & 0 & 0 & 0 \\ 0 & 0 & e^{-\kappa d} & 0 & e^{\kappa d} & 0 & -\cos \frac{\theta}{2} & -\sin \frac{\theta}{2} \\ 0 & 0 & -\kappa e^{-\kappa d} & 0 & \kappa e^{\kappa d} & 0 & -ik_{\uparrow} \cos \frac{\theta}{2} & -ik_{\uparrow} \sin \frac{\theta}{2} \\ 0 & -1 & 0 & 1 & 0 & 1 & 0 & 0 \\ 0 & ik_{\downarrow} & 0 & -\kappa & 0 & \kappa & 0 & 0 \\ 0 & 0 & 0 & e^{-\kappa d} & 0 & e^{\kappa d} & \sin \frac{\theta}{2} & -\cos \frac{\theta}{2} \\ 0 & 0 & 0 & -\kappa e^{-\kappa d} & 0 & \kappa e^{\kappa d} & ik_{\uparrow} \sin \frac{\theta}{2} & -ik_{\downarrow} \cos \frac{\theta}{2} \end{pmatrix} \begin{pmatrix} r_{\uparrow} \\ r_{\downarrow} \\ A_{\uparrow} \\ A_{\downarrow} \\ B_{\uparrow} \\ B_{\downarrow} \\ t_{\uparrow} \\ t_{\downarrow} \end{pmatrix} = \begin{pmatrix} k_{\uparrow}^{-1/2} \\ ik_{\downarrow}^{1/2} \\ 0 \\ 0 \\ 0 \\ 0 \\ 0 \\ 0 \end{pmatrix}. \quad (2.9)$$

Slonczewski solves this set of equations in the limit of large barrier thickness  $d$ . He is then able to get an approximate solution for the coefficients, accurate to leading order in  $e^{-\kappa d}$ . The solutions for the coefficients are available in the literature [4]. They are not reproduced here as little insight is gained due to the complicated form of the solutions. The existence of the approximate solution, however, allows for the calculation of the probability flux across the barrier [19],

$$\vec{j}(\vec{x}, t) = \frac{\hbar}{m} \Im(\psi^* \nabla \psi). \quad (2.10)$$

Generalizing this result to the spin transmissivity in one dimension, in the system of units defined earlier, yields

$$T_z = \Im \sum_{\sigma} \sigma \psi_{\sigma}^* \frac{d\psi_{\sigma}}{d\xi}. \quad (2.11)$$

Slonczewski shows that the ratio of the magnitudes of the spin up to spin down wave functions in the barrier region, for a spin up wave incident from ferromagnet 1, is approximately equal to  $e^{-2\kappa d}$ . In the limit of large  $d$ , the  $\sigma = -1$  contribution can therefore be neglected giving

$$T_p = \Im \left( \psi_{\uparrow}^* \frac{d\psi_{\uparrow}}{d\xi} \right) \quad (2.12)$$

for the particle transmissivity across the barrier. The tunneling conductance for a two-band ferromagnet as pictured in Figure 2.2 is calculated using [4]

$$G = \left( \frac{e^2}{8\pi^2 \hbar} \right) \left( \frac{\kappa}{d} \right) (T_{p\uparrow} + T_{p\downarrow}) \quad (2.13)$$

where  $T_{p\uparrow}, T_{p\downarrow}$  are the transmissivities for the majority and minority electrons incident from ferromagnet 1 respectively.

The solution to this equation is of the form

$$G = G_{fbf} (1 + P_{fb}^2 \cos \theta) \quad (2.14)$$

with the ferromagnet-barrier effective spin polarization given by

$$P_{fb} = \frac{(k_{\uparrow} - k_{\downarrow})(\kappa^2 - k_{\uparrow}k_{\downarrow})}{(k_{\uparrow} + k_{\downarrow})(\kappa^2 + k_{\uparrow}k_{\downarrow})} \quad (2.15)$$

and the mean ferromagnet-barrier-ferromagnet tunneling conductance given by

$$G_{fbf} = \frac{\kappa}{hd} \left( \frac{e\kappa(\kappa^2 + k_{\uparrow}k_{\downarrow})(k_{\uparrow} + k_{\downarrow})}{\pi(\kappa^2 + k_{\uparrow}^2)(\kappa^2 + k_{\downarrow}^2)} \right)^2 e^{-2\kappa d}. \quad (2.16)$$

The treatment given here which follows that of Slonczewski has added a second term to the spin polarization defined by M.B. Stearns in equation (2.5). This new second term gives the barrier height effect. For any value  $0 < \kappa < \infty$ , equation (2.15) predicts a diminished spin polarization and therefore, from equation (2.3), a diminished TMR due to the barrier or interfacial factor.

In an Fe-Insulator-Fe junction, the values of  $k_f^{\uparrow}$  and  $k_f^{\downarrow}$  are given in Table 2.1 as 0.5 and 0.19, in units of  $\frac{2\pi}{a}$ . The energy required to remove an electron from iron, the work function of iron, can be used as a rough estimate for the barrier height. The work function of iron is 4.31 eV [20], giving  $\kappa = 0.486\frac{2\pi}{a}$ . The effective spin polarization for an Fe-Insulator-Fe barrier in the Slonczewski approximation is then:

$$P_{fb} = \frac{(k_{\uparrow} - k_{\downarrow})}{(k_{\uparrow} + k_{\downarrow})} \times \frac{(\kappa^2 - k_{\uparrow}k_{\downarrow})}{(\kappa^2 + k_{\uparrow}k_{\downarrow})} = 0.45 \times 0.43 = 0.19. \quad (2.17)$$

This result, by equation (2.3), predicts a conductance variation  $\Delta G/G$  of 7.0%. This is much lower than the result of 32% found when barrier effects were ignored.

## 2.4 Barrier Thickness Effects

Slonczewski's result has come under question as experimental results have obtained TMR values much greater than that given by the theory described above. An obvious point of contention is the large  $d$  approximation used in solving the matrix equation (2.9). This issue has been addressed recently in the work of J. M. MacLaren [5]. MacLaren looks at the same tunneling geometry as Slonczewski, shown in

Figure (2.3), but makes an initial simplification by looking for solutions only at  $\theta = 0$  and  $180^\circ$ . His approach also differs from Slonczewski's in that a closed form solution is not sought. The set of equations generated by matching wave functions and derivatives at the boundaries is instead solved numerically for given values of  $k_f^\uparrow, k_f^\downarrow, \kappa$ , and barrier thickness. This work, described below, remedies many of the inconsistencies of the earlier results and matches well with experimental measurements.

MacLaren's approach of calculating the conductivity only for parallel and antiparallel spin alignments reduces the wave functions given in equation (2.7) to

$$\begin{aligned}\psi_1 &= k_1^{-1/2} e^{ik_1\xi} + r e^{-ik_1\xi} \\ \psi_b &= A e^{-\kappa\xi} + B e^{\kappa\xi} \\ \psi_2 &= t e^{ik_2(\xi-d)}\end{aligned}\tag{2.18}$$

The transmission coefficients for majority to majority, minority to minority, and majority to minority conductance are then calculated by letting  $k_1 = k_2 = k_\uparrow$ ,  $k_1 = k_2 = k_\downarrow$ , and  $k_1 = k_\uparrow; k_2 = k_\downarrow$ , respectively.

The matrix equation to be solved for the unknown coefficients is now

$$\begin{pmatrix} 1 & 1 & -1 & 0 \\ -\kappa & \kappa & ik_1 & 0 \\ e^{-\kappa d} & e^{\kappa d} & 0 & -1 \\ -\kappa e^{-\kappa d} & \kappa e^{\kappa d} & 0 & -ik_2 \end{pmatrix} \begin{pmatrix} A \\ B \\ r \\ t \end{pmatrix} = \begin{pmatrix} k_1^{-1/2} \\ ik_1^{1/2} \\ 0 \\ 0 \end{pmatrix}.\tag{2.19}$$

Inverting the matrix to solve for the transmission coefficient yields

$$\begin{pmatrix} 1 & 1 & -1 & 0 \\ -\kappa & \kappa & ik_1 & 0 \\ e^{-\kappa d} & e^{\kappa d} & 0 & -1 \\ -\kappa e^{-\kappa d} & \kappa e^{\kappa d} & 0 & -ik_2 \end{pmatrix}^{-1} = \alpha \begin{pmatrix} e^{d\kappa}k_1(-k_2 - i\kappa) & e^{d\kappa}(-\kappa + ik_2) & k_1k_2 + i\kappa k_2 & \kappa + ik_1 \\ e^{-d\kappa}k_1(k_2 - i\kappa) & e^{-d\kappa}(-\kappa - ik_2) & -k_1k_2 - i\kappa k_2 & \kappa - ik_1 \\ -\zeta\kappa^2 + i\gamma\kappa k_2 & -\gamma\kappa + i\zeta k_2 & 2i\kappa k_2 & 2\kappa \\ 2i\kappa k_1 & 2\kappa & -\zeta\kappa^2 + i\gamma\kappa k_1 & \gamma\kappa - i\zeta k_1 \end{pmatrix} \quad (2.20)$$

with  $\alpha = \frac{1}{\zeta(\kappa^2 - k_1k_2) - i\gamma(\kappa(k_1 + k_2))}$ ,  $\zeta = e^{\kappa d} - e^{-\kappa d}$ , and  $\gamma = e^{\kappa d} + e^{-\kappa d}$ .

Multiplying the inverse matrix through equation (2.19) gives

$$\begin{pmatrix} A \\ B \\ r \\ t \end{pmatrix} = \alpha \begin{pmatrix} e^{d\kappa}k_1(-k_2 - i\kappa) & e^{d\kappa}(-\kappa + ik_2) & k_1k_2 + i\kappa k_2 & \kappa + ik_1 \\ e^{-d\kappa}k_1(k_2 - i\kappa) & e^{-d\kappa}(-\kappa - ik_2) & -k_1k_2 - i\kappa k_2 & \kappa - ik_1 \\ -\zeta\kappa^2 + i\gamma\kappa k_2 & -\gamma\kappa + i\zeta k_2 & 2i\kappa k_2 & 2\kappa \\ 2i\kappa k_1 & 2\kappa & -\zeta\kappa^2 + i\gamma\kappa k_1 & \gamma\kappa - i\zeta k_1 \end{pmatrix} \begin{pmatrix} k_1^{-1/2} \\ ik_1^{1/2} \\ 0 \\ 0 \end{pmatrix}. \quad (2.21)$$

The coefficient of the wave function in ferromagnet 2 is then

$$t = \frac{4i\kappa k_1^{1/2}}{(e^{\kappa d} - e^{-\kappa d})(\kappa^2 - k_1k_2) - i(e^{\kappa d} + e^{-\kappa d})(\kappa(k_1 + k_2))}. \quad (2.22)$$

The normalization condition on  $\psi_1$  gives unit probability flux input from ferromagnet 1. The transmission coefficient is therefore given by the probability flux in

ferromagnet 2.

$$\begin{aligned}
T &= \Im(\psi_2^* \nabla \psi_2) \\
&= tt^* k_2 \\
&= \frac{16k_1 \kappa^2 k_2}{\{(e^{\kappa d} - e^{-\kappa d})(\kappa^2 - k_1 k_2)\}^2 + \{(e^{\kappa d} + e^{-\kappa d})(\kappa(k_1 + k_2))\}^2} \\
&= \frac{16k_1 \kappa^2 k_2 e^{2d\kappa}}{\{(1 - e^{2d\kappa})(\kappa^2 - k_1 k_2)\}^2 + \{(1 + e^{2d\kappa})(\kappa(k_1 + k_2))\}^2},
\end{aligned} \tag{2.23}$$

where the wave vectors are assumed to point perpendicular to the barrier.

Equation (2.23) can be simplified by taking the limit  $e^{2d\kappa} \gg 1$ . This limit will be accurate for most tunneling situations, where the reflection coefficient is close to unity. Applying this limit yields

$$T = \frac{16k_1 \kappa^2 k_2 e^{-2d\kappa}}{(\kappa^2 - k_1 k_2)^2 + [\kappa(k_1 + k_2)]^2}. \tag{2.24}$$

Equation (2.24) is the transmission coefficient used by MacLaren [5] to numerically solve for the conductance ratio between ferromagnetically and antiferromagnetically aligned systems.

The tunneling conductance is calculated using the Landauer-Büttiger formula [21, 22]

$$G = \frac{e^2}{(2\pi)^2 h} \int d^2 k_{\parallel} T(k_{\parallel}) \tag{2.25}$$

where  $k_{\parallel}$  is the component of the wave vector parallel to the boundary and is considered conserved during the tunneling. The wave vectors,  $k_1$ ,  $k_2$ , and  $\kappa$ , can be written as a function of  $k_{\parallel}$  as  $k_1 = \sqrt{(2m/\hbar^2)V_1 - k_{\parallel}^2}$ ,  $k_2 = \sqrt{(2m/\hbar^2)V_2 - k_{\parallel}^2}$ , and  $\kappa = \sqrt{(2m/\hbar^2)V_b + k_{\parallel}^2}$ . Here, the zero point energy is defined to be the Fermi energy level, consistent with Figure 2.2.

The calculation for the conductance variation across an Fe-insulator-Fe barrier with parallel and antiparallel spin alignments can now be performed. The conductance for parallel alignment of spins is given as the sum of majority to majority and

minority to minority conductance, while that for antiparallel alignment is the sum of majority to minority and minority to majority conductance. From equation (2.24) we have

$$\begin{aligned}
T_{\uparrow\uparrow} &= \frac{16k_{\uparrow}^2\kappa^2e^{-2d\kappa}}{(\kappa^2 - k_{\uparrow}^2)^2 + (2\kappa k_{\uparrow})^2} = \frac{16k_{\uparrow}^2\kappa^2e^{-2d\kappa}}{(\kappa^2 + k_{\uparrow}^2)^2} \\
T_{\downarrow\downarrow} &= \frac{16k_{\downarrow}^2\kappa^2e^{-2d\kappa}}{(\kappa^2 - k_{\downarrow}^2)^2 + (2\kappa k_{\downarrow})^2} = \frac{16k_{\downarrow}^2\kappa^2e^{-2d\kappa}}{(\kappa^2 + k_{\downarrow}^2)^2} \\
T_{\uparrow\downarrow} = T_{\downarrow\uparrow} &= \frac{16k_{\uparrow}\kappa^2k_{\downarrow}e^{-2d\kappa}}{(\kappa^2 - k_{\uparrow}k_{\downarrow})^2 + [\kappa(k_{\uparrow} + k_{\downarrow})]^2} = \frac{16k_{\uparrow}\kappa^2k_{\downarrow}e^{-2d\kappa}}{\kappa^4 + \kappa^2(k_{\uparrow}^2 + k_{\downarrow}^2) + k_{\uparrow}^2k_{\downarrow}^2}
\end{aligned} \tag{2.26}$$

where  $k_{\uparrow} = \sqrt{k_f^{\uparrow 2} - k_{\parallel}^2}$ ,  $k_{\downarrow} = \sqrt{k_f^{\downarrow 2} - k_{\parallel}^2}$ ,  $\kappa = \sqrt{V_b + k_{\parallel}^2}$ , and  $V_b$  is the barrier height above the fermi energy level.

Substituting these values into (2.25) yields

$$\begin{aligned}
G_{\uparrow\uparrow} &= \frac{e^2}{(2\pi)^2h} \int d^2k_{\parallel} \frac{16(k_f^{\uparrow 2} - k_{\parallel}^2)(V_b + k_{\parallel}^2)e^{-2d\sqrt{V_b+k_{\parallel}^2}}}{(k_f^{\uparrow 2} + V_b)^2} \\
&= \frac{16e^2}{2\pi h(k_f^{\uparrow 2} + V_b)^2} \int_0^{k_f^{\uparrow}} k_{\parallel} dk_{\parallel} (k_f^{\uparrow 2} - k_{\parallel}^2)(V_b + k_{\parallel}^2)e^{-2d\sqrt{V_b+k_{\parallel}^2}},
\end{aligned} \tag{2.27}$$

$$\begin{aligned}
G_{\downarrow\downarrow} &= \frac{e^2}{(2\pi)^2h} \int d^2k_{\parallel} \frac{16(k_f^{\downarrow 2} - k_{\parallel}^2)(V_b + k_{\parallel}^2)e^{-2d\sqrt{V_b+k_{\parallel}^2}}}{(k_f^{\downarrow 2} + V_b)^2} \\
&= \frac{16e^2}{2\pi h(k_f^{\downarrow 2} + V_b)^2} \int_0^{k_f^{\downarrow}} k_{\parallel} dk_{\parallel} (k_f^{\downarrow 2} - k_{\parallel}^2)(V_b + k_{\parallel}^2)e^{-2d\sqrt{V_b+k_{\parallel}^2}},
\end{aligned} \tag{2.28}$$

and

$$\begin{aligned}
G_{\uparrow\downarrow} &= \frac{e^2}{(2\pi)^2h} \int d^2k_{\parallel} \frac{16(V_b + k_{\parallel}^2)\sqrt{(k_f^{\uparrow 2} - k_{\parallel}^2)(k_f^{\downarrow 2} - k_{\parallel}^2)}e^{-2d\sqrt{V_b+k_{\parallel}^2}}}{(V_b + k_{\parallel}^2)^2 + (V_b + k_{\parallel}^2)(k_f^{\uparrow 2} + k_f^{\downarrow 2} - 2k_{\parallel}^2) + (k_f^{\uparrow 2} - k_{\parallel}^2)(k_f^{\downarrow 2} - k_{\parallel}^2)} \\
&= \frac{16e^2}{2\pi h} \int_0^{k_f^{\downarrow}} k_{\parallel} dk_{\parallel} \frac{(V_b + k_{\parallel}^2)\sqrt{(k_f^{\uparrow 2} - k_{\parallel}^2)(k_f^{\downarrow 2} - k_{\parallel}^2)}e^{-2d\sqrt{V_b+k_{\parallel}^2}}}{(V_b^2 + V_b(k_f^{\uparrow 2} + k_f^{\downarrow 2}) + k_f^{\uparrow 2}k_f^{\downarrow 2})}.
\end{aligned} \tag{2.29}$$

Table 2.2: Calculated conductance variation between ferromagnetic and antiferromagnetic spin alignments in iron across a tunneling gap.

Barrier Height (eV)	Barrier Thickness (nm)						Slonczewski Model
	1	5	10	50	100	500	
0.1	23.0%	26.9%	27.2%	27.4%	27.4%	27.4%	27.6%
0.5	9.51%	10.6%	11.1%	11.4%	11.4%	11.5%	11.6%
1.0	6.41%	2.20%	2.48%	2.72%	2.74%	2.77%	2.86%
2.0	13.9%	0.60%	0.32%	0.18%	0.17%	0.16%	0.21%
3.0	23.1%	4.22%	3.41%	2.93%	2.87%	2.83%	2.85%
4.0	30.4%	8.28%	7.03%	6.27%	6.18%	6.12%	6.12%
4.31	32.4%	9.46%	8.09%	7.25%	7.16%	7.08%	7.08%
5.0	36.2%	11.9%	10.3%	9.28%	9.17%	9.08%	9.07%
10.0	51.7%	23.3%	20.4%	18.6%	18.4%	18.2%	18.2%

Equations (2.27) - (2.29) can be used to solve for the conductance variation between ferromagnetic and antiferromagnetic spin alignments for any any tunneling gap given the values of  $k_f^\uparrow, k_f^\downarrow$ , barrier height, and barrier thickness.

Solving for the specific case of iron to iron tunneling we have, from Table 2.1,  $k_f^\uparrow = 0.5$ , and  $k_f^\downarrow = 0.19$ . As a first approximation the barrier height can be taken as the work function of iron, assuming that the polyimide is a perfect insulator. This approximation gives  $V_b = \kappa^2 = 4.31eV = 0.486^2(\frac{2\pi}{a})^2$ . Finally, as a reasonable tunneling gap thickness take  $d = 10nm = 218(\frac{a}{2\pi})$ . Substituting these values into equations (2.27) - (2.29) gives  $\frac{\Delta G}{G} = 8.1\%$ .

Table 2.2 displays the calculated conductance variation over a wide range of barrier heights and thicknesses. The Slonczewski results, which are independent of barrier thickness, are displayed for comparison. The Julliere Model predicts a conductance ratio 33.6% independent of the barrier thickness and height.

Figure 2.4 displays a three-dimensional plot of the resultant conductance ratio for iron-barrier-iron tunneling as a function of barrier height and thickness, and Figure 2.5 shows a plot of the ratio for a fixed barrier height of 4.31 eV.

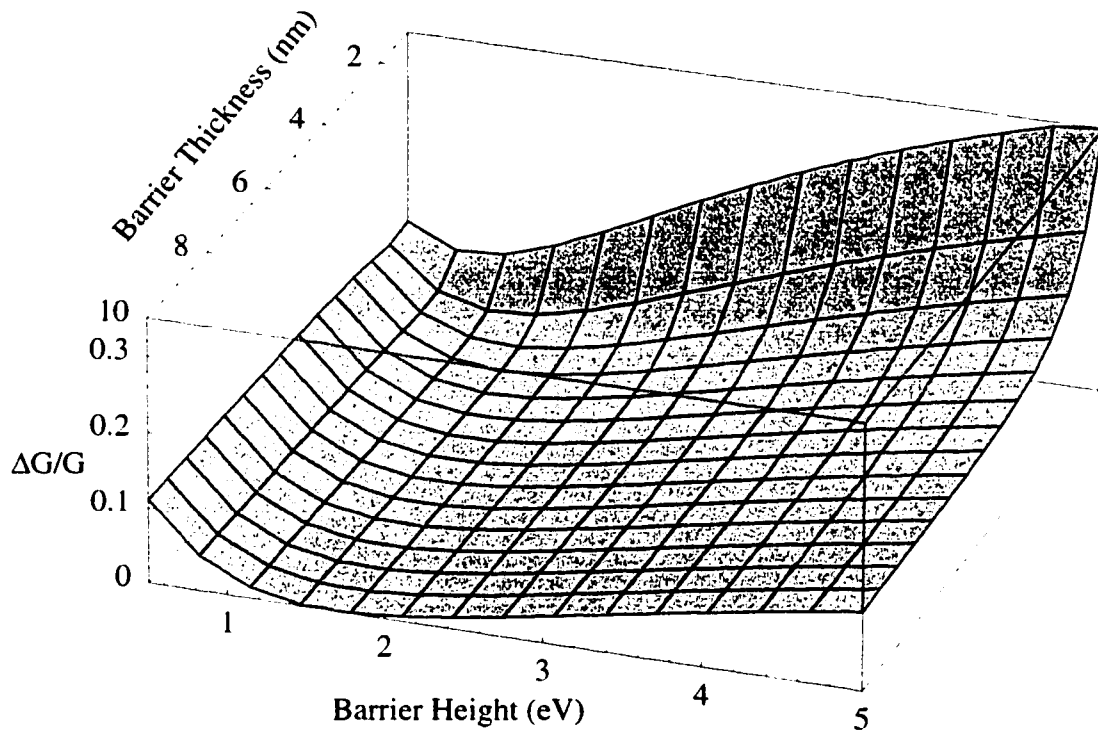


Figure 2.4: Plot of conductance ratio  $\frac{\Delta G}{G}$  for iron-barrier-iron tunneling as a function of barrier height and thickness .

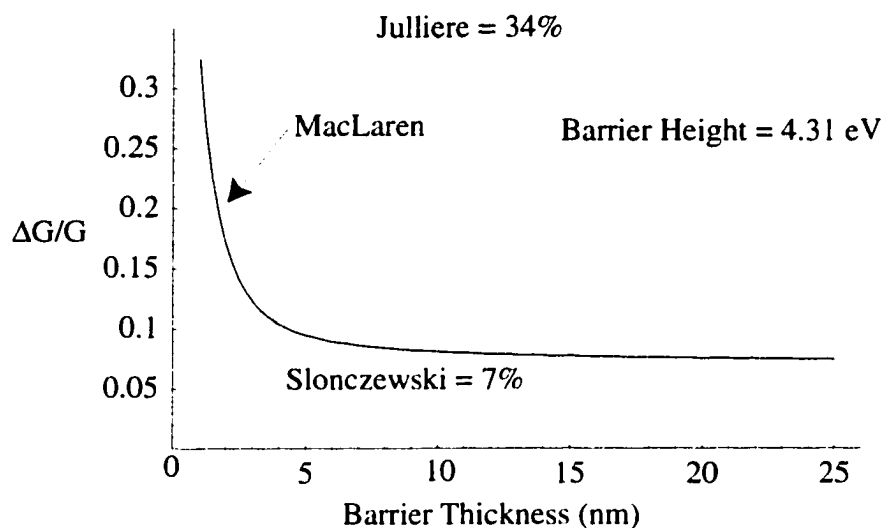


Figure 2.5: Plot of conductance ratio for iron-insulator-iron tunneling as a function of barrier thickness at a barrier height of 4.31 eV.

It is clear from this treatment of spin dependent tunneling through an insulating barrier that the properties of the barrier layer are critical. The results in Table 2.2 for the specific case of iron to iron tunneling show a dramatic variation in the conductance ratio, from less than 0.2% to over 50%, depending upon the barrier properties. The Slonczewski results, based upon the large barrier thickness approximation, agree relatively well for barrier thicknesses greater than approximately 10 nm. As the barrier thicknesses decrease below 10 nm the results of the Slonczewski and MacLaren models quickly diverge. The Julliere results provide an adequate approximation of Fe-Barrier-Fe tunneling only in a narrow regime of barrier heights near the work function of iron and barrier thicknesses near 1 nm.

It must be noted that this model of spin dependent tunneling is also a vast simplification of the physical realities. The free electron model and a simple step barrier have been assumed throughout this work. A more accurate account of spin dependent tunneling must account for the actual band structure of the ferromagnet.

Research in this area is ongoing [5], although conductance ratios calculated using this approach agree rather poorly with experimental data. Surface effects on both the band structure and the barrier qualities must also be considered in a full theory of the phenomena. Research in these areas is in its infancy.

# Chapter 3

## Variable Range Hopping

This chapter details the theory of variable range hopping (VRH). This theory was originally proposed by Mott [23] in 1968 to explain conduction of electrons in insulators near the metal-insulator transition, and has since been expanded upon by many authors. Of particular interest to the present study is variable range hopping in granular systems, which has recently been summarized by T.G. Castner [24] and P. Sheng [25]. The conduction mechanism is a result of the combined processes of thermal activation and tunneling, and plays a strong role in the transport properties of the iron polyimide composites with iron volume fractions near the percolation threshold.

### 3.1 Electronic Conduction and Localization

The electronic conduction of a material can be roughly characterized by a plot of the energy versus density of states. In an insulator, all the bands will be either completely filled or empty, prohibiting any electric current flow. A conductor will have partially filled bands through which conduction will take place [20]. Figure 3.1

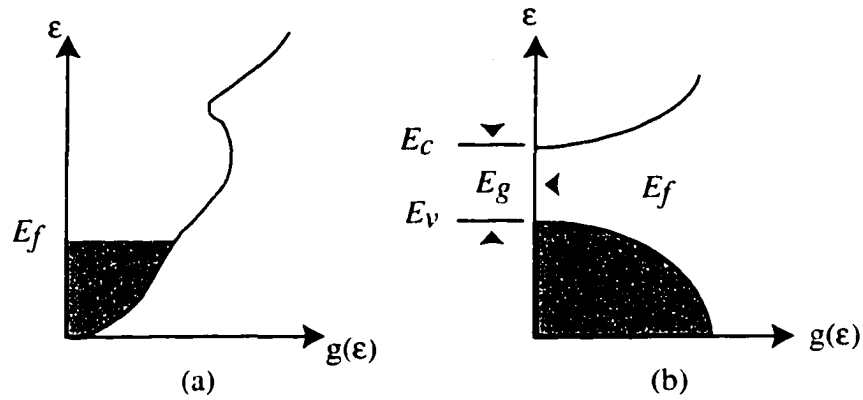


Figure 3.1: Electron density of states for normal metal (a) and insulator (b).

displays a density of states diagram for a normal metal and an insulator. In this figure  $E_f$  is the Fermi energy level,  $E_v$  is the top of the filled band in the insulator (valence band),  $E_c$  is the bottom of the empty band (conduction band), and  $E_g$  is the energy gap between the valence and conduction bands in the insulator. In order for current to flow in the insulator electrons must be activated above the energy gap into the conduction band. Materials with small energy gaps through which this type of conduction is common are known as semiconductors.

The situation becomes more complicated when disorder is introduced into the lattice. Anderson [26] showed that the introduction of a random potential at each well in a crystalline lattice can dramatically alter the conduction properties of the material. The random potential has the effect of destroying the phase coherence of the wave function as it passes from one potential well to the next and reducing the density of states at mid band. If the disorder is greater than the width of the band a wave function which would otherwise span the lattice can become localized around a point  $r_0$  in space. This phenomena is known as Anderson Localization, and is summarized by Mott [27, 28] in the development of the theory of metal-insulator transitions.

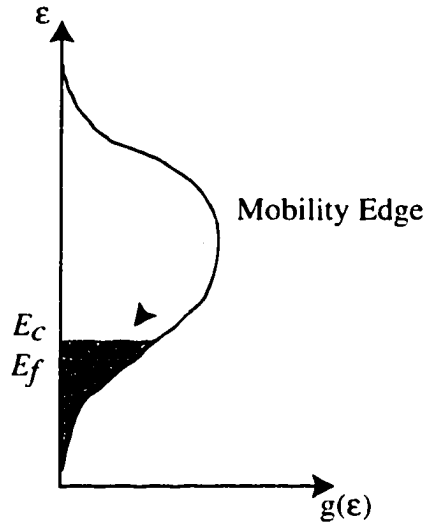


Figure 3.2: Anderson localized states inside conduction band.

If the disorder is not large enough to produce localization throughout the band, Mott [29] showed that states in the band tails could still become localized. These states would then be separated from the extended, non localized, states by a sharp energy cutoff. Cohen [30] coined this energy value,  $E_c$ , the mobility edge. If the energy of a band electron is less than  $E_c$  the electron will be localized. Mott [28] summarizes this behavior as

$$\begin{aligned}\sigma(E) &= 0 \quad (E < E_c), \\ \sigma(E) &> 0 \quad (E > E_c).\end{aligned}\tag{3.1}$$

Figure 3.2 shows a modified density of states diagram for an Anderson localized electron wavefunction. The system depicted will be nonconducting even though the Fermi surface electrons occupy an unfilled band.

In a system with localized states as depicted in Figure 3.2, conduction can occur by excitation of the charge carriers to the mobility edge or by hopping from one localized state to another. For the first case, thermal excitation of the charge

carriers, the conductivity will have the form

$$\sigma = \sigma_0 e^{-(E_c - E_f)/k_B T}. \quad (3.2)$$

The second process, hopping conduction, is described in the following section.

## 3.2 Hopping Conduction

Hopping conduction describes the process in which an electron in an occupied state just below the Fermi energy level receives energy from a phonon which enables it to move to a nearby state above  $E_f$ . This conduction process was first proposed by Miller and Abrahams [31] to describe impurity conduction in doped and compensated semiconductors. The electron movement is described as a series of hops from one localized state to the next, where hopping is assumed to occur between nearest neighbor sites only. The conductivity of this process was found to be

$$\sigma = \sigma_3 e^{-\epsilon_3/k_B T} \quad (3.3)$$

where  $\epsilon_3$  is the smallest energy difference between neighboring sites. This value can be estimated from the density of states at the Fermi energy level.

$$\begin{aligned} g(E_f)dE &= \frac{N(E_f + dE) - N(E_f)}{V} \\ dE &= \frac{N(E_f + dE) - N(E_f)}{g(E_f)V} \\ \Delta E_{min} &= \frac{1}{g(E_f)V}. \end{aligned} \quad (3.4)$$

Here  $N(E)$  is the number of states with energy less than or equal to  $E$ ,  $V$  is the volume of the site and  $\Delta E_{min}$  is the minimum energy difference between states, corresponding to  $N(E_f + dE) - N(E_f) = 1$ . For nearest neighbor hopping  $V \sim a^3$ , where  $a$  is the distance between nearest neighbors. This gives

$$\epsilon_3 \sim \frac{1}{g(E_f)a^3} \quad (3.5)$$

for nearest neighbor hopping.

Mott [23] first examined the consequences of removing the requirement that hopping occur only between nearest neighbor sites. He argues that the energy difference between states,  $\epsilon_3$  of the previous work, can be reduced by increasing the volume over which a state is chosen. For a given hopping radius,  $R$ , the minimum energy difference is determined by equation (3.4) which now takes the form

$$\Delta E_{min} = \frac{1}{(4\pi/3)R^3g(E_f)}. \quad (3.6)$$

An electron hopping over a large distance, however, will be required to tunnel through a classically forbidden region. The conductivity must therefore contain a factor associated with this tunneling, given as

$$\sigma \propto e^{-2\alpha R} \quad (3.7)$$

where  $1/\alpha$  is the decay length of the localized wave function. Combining equations (3.3), (3.6), and (3.7) yields

$$\sigma \propto \exp\left[-2\alpha R - \frac{3}{4\pi k_B T R^3 g(E_f)}\right]. \quad (3.8)$$

Equation (3.8) describes the process of variable range hopping. At a given temperature the electron will tunnel over a distance  $R$  which provides the least resistance, maximizing the conductivity. This distance is therefore found by maximizing  $\sigma$  with respect to  $R$ .

$$\frac{d\sigma}{dR} = \left(-2\alpha + \frac{9}{4\pi k_B T R^4 g(E_f)}\right) \exp\left[-2\alpha R - \frac{3}{4\pi k_B T R^3 g(E_f)}\right]. \quad (3.9)$$

Setting  $d\sigma/dR = 0$  gives

$$\begin{aligned} 2\alpha &= \frac{9}{4\pi k_B T R^4 g(E_f)}, \\ R &= \left(\frac{9}{8\pi\alpha k_B T g(E_f)}\right)^{1/4}. \end{aligned} \quad (3.10)$$

Substituting this value of  $R$  back into equation (3.8) yields

$$\begin{aligned}\sigma &\propto \exp\left[-2\alpha\left(\frac{9}{8\pi\alpha k_B T g(E_f)}\right)^{1/4} - \frac{3}{4\pi k_B T\left(\frac{9}{8\pi\alpha k_B T g(E_f)}\right)^{3/4} g(E_f)}\right], \\ &= \exp\left[-\left\{\frac{\alpha^3}{k_B g(E_f)}\left(\frac{2 \times 9}{\pi} + \frac{2}{9\pi}\right)/T\right\}^{1/4}\right], \\ \sigma &= A \exp\left[-\left(\frac{T_0}{T}\right)^{1/4}\right], \quad \text{or}\end{aligned}\tag{3.11}$$

$$\ln \sigma \propto -T^{-1/4}.$$

The final result of equation (3.11) is Mott's  $T^{-1/4}$  law for variable range hopping conductivity. Experimental results often obtain an exponential factor somewhat higher than  $1/4$  [24], and it has been argued that the inclusion of electron - electron interactions will change the factor to  $1/2$  [32]. The theory thus modified can be stated

$$\ln \sigma \propto -T^{-\nu}, \quad 1/4 \leq \nu \leq 1/2.\tag{3.12}$$

### 3.3 Variable Range Hopping in Granular Metals

The theory of hopping conduction in granular metals [25] is a slightly modified version of theory developed in the preceding section. The model system here is a random mixture of nanometer sized conducting and insulating grains. The conduction across the system is from one conducting grain to the next. For a volume concentration of the conductor greater than the percolation threshold metallic conduction is predicted. Hopping conduction will occur when the metal volume concentration falls beneath the percolation threshold.

Within the insulating regime, electron flow from one metal particle to the next will occur by tunneling through an insulating gap. The conductance between two grains,  $i$  and  $j$ , can then be written as

$$G_{ij} = G_0 \exp(-2\chi S_{ij} - E_{ij}/k_B T).\tag{3.13}$$

In this equation  $\chi$  is the tunneling constant,  $S_{ij}$  is the distance between the particles, and  $E_{ij}$  is the activation energy required to move an electron from particle  $i$  to  $j$ . This activation energy is a result of the charging energy of the particle.

$$W = QV = Q^2/\kappa C \quad (3.14)$$

where  $C$  is the capacitance of the particle and  $\kappa$  is the effective dielectric constant.

The capacitance of an isolated spherical particle is  $C = 4\pi a$ . The activation energy for the addition of an electron to a small metallic grain is then

$$E_{ij} \approx e^2/4\pi\kappa a. \quad (3.15)$$

For a dielectric constant of  $3\epsilon_0$  and a particle radius of 10 nm the activation energy is

$$\begin{aligned} E_{ij} &\approx e \left( \frac{e}{4\pi 3(4\pi \times 10^{-7} c^2)^{-1} 10^{-8}} \right) \\ &\approx e \left( \frac{3(1.6 \times 10^{-19})}{10^{-17}} \right) \end{aligned} \quad (3.16)$$

$$E_{ij} \approx 50\text{meV}.$$

In a randomly mixed granular material there is expected to be a distribution of particle sizes throughout the matrix. As is evident from equation (3.15) the charging energy will be smaller for a larger particle. Minimizing the charging energy will require an increase in the tunneling distance as more particles are sampled. As in the previous section, maximizing the conductivity results in an optimum temperature dependent tunneling distance.

The calculation is performed using the critical path method [33] as outlined by Sheng [25]. In a granular conductor-insulator system the conductance between two grains will contribute significantly to the overall conductivity only if

$$G_0 \exp[-2\chi S_{ij} - E_{ij}/k_B T] = G_{ij} \geq G_C \quad (3.17)$$

where  $G_C$  is the conductance of the entire conduction path. Taking the natural logarithm of both sides of equation (3.17) gives

$$\ln(G_0/G_C) \geq 2\chi S_{ij} + E_{ij}/k_B T. \quad (3.18)$$

Equation (3.18) sets a limit on the maximum tunneling distance,  $S_m$ , and particle charging energy,  $E_m$ .

$$\begin{aligned} S_m &= (1/2\chi) \ln(G_0/G_C), \text{ and} \\ E_m &= k_B T \ln(G_0/G_C). \end{aligned} \quad (3.19)$$

It is now necessary to consider the formation requirement of a percolating network. One such requirement is that the number of bonds emanating from a site must exceed a critical bond percolation number,  $b_c$  [34]. The number of bonds a particular site is able to form will increase with the density of states in the vicinity of the Fermi level,  $g(E_f)$ , the maximum possible tunneling distance,  $S_m$ , and maximum activation energy,  $E_m$ . At the percolation threshold this number of bonds is a dimensionless constant. It is then reasonable to assume

$$b_c = f g(E_f) E_m S_m^3 \quad (3.20)$$

where  $f$  is a dimensionless proportionality constant.

As an example consider two systems of the same dimensionality, both at the percolation threshold. The two must then have the same  $b_c$ . If one of the systems has a larger  $E_m$ , for example, it must also have a smaller  $S_m$  or  $g(E_f)$  than the other in order to remain at the percolation threshold. Equation (3.20) is the simplest way to derive a dimensional number from these three quantities. This result has been confirmed in a detailed calculation by Sheng and Klafter [35].

Substituting (3.19) into (3.20) gives

$$\begin{aligned} \frac{b_c}{f g(E_f)} &= \frac{k_B T}{(2\chi)^3} [\ln(G_0/G_C)]^4, \text{ or} \\ \ln(G_c) &\propto -T^{-1/4} \end{aligned} \quad (3.21)$$

Again, experimental measurements often find the exponential factor to be  $1/2$  [24, 25]. Sheng argues this is caused by an interpolation between low temperature hopping,  $T^{-1/4}$ , and high temperature activation,  $T^{-1}$ , behaviors.

# Chapter 4

## Computer Simulation

This final chapter of the theoretical work develops a computer model of the conduction across iron polyimide nanocomposites based upon percolation theory. Percolation theory provides a framework from which to explore the metal-insulator transition, as well as enabling the calculation of transport properties at the transition. The transition point, the percolation threshold, can be calculated by treating the individual iron particles as randomly distributed conducting spheres within an insulating matrix and searching for conduction paths across the system as the volume percentage of iron particles within the matrix increases. The point at which direct contact conduction first occurs is the percolation threshold. A computer model to perform this calculation has been developed and will be presented in this chapter. The model also performs calculations of the sample resistivity at the percolation threshold or as a function of iron volume concentration. In addition, the effects of spin dependent tunneling are incorporated enabling calculations of the TMR.

## 4.1 Two-Dimensional Percolation Simulation

The model developed here is based upon close packing of iron particles within the polyimide matrix. For the two-dimensional case, spherical iron particles are randomly added to unfilled sites on a trigonal lattice. The percolation threshold is determined by finding the concentration at which a connected network first forms across the system. Conduction is assumed between nearest neighbor pairs only.

The system is searched for the existence of a percolating network each time a particle is added to the matrix. The occupancy of lattice sites which are nearest neighbors to the location of the added particle is determined. Occupied sites on neighboring lattice positions are grouped with the original site into a cluster. The occupancy of all sites neighboring the cluster is then determined and occupied sites are added to the cluster. This process is continued until all the neighboring sites of the cluster are vacant. At this point it is determined if the cluster spans the system. A spanning cluster is recognized as one which contains particles at both extrema of the system. If a spanning cluster is found the system, by definition, percolates and the percolation density is given by the fraction of lattice sites which contain iron particles. If the cluster does not span the system an additional particle is added to the system, beginning a new search.

Figures 4.1 through 4.3 displays the results from three separate runs for the calculation of the percolation threshold for a 50x50 trigonal array. In these figures the particle size is scaled to equal the lattice parameter, such that nearest neighbor particles will touch. The trigonal lattice is displayed in gray under the spherical particles. Particles that are members of the spanning cluster are shown in black while particles in the system which are not members of the spanning cluster are drawn in gray. The data shown in Figure 4.1 and 4.3 percolates across the system in both the horizontal and vertical direction. In contrast, Figure 4.2 only percolates in

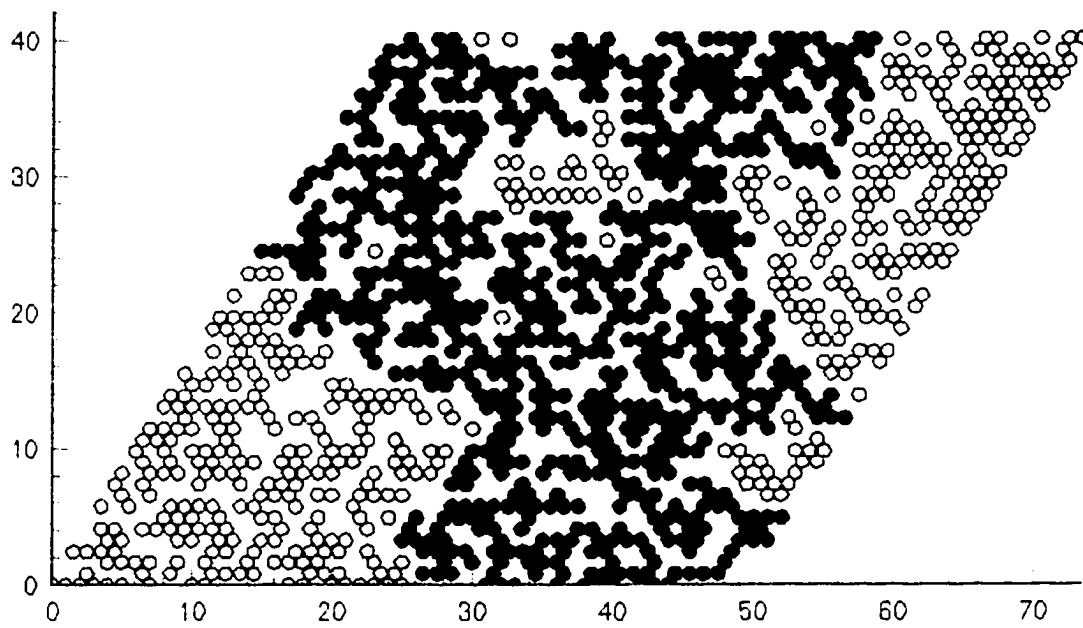


Figure 4.1: Percolation simulation results for 50x50 trigonal array. Calculated percolation threshold  $p_c = 50.5\%$ .

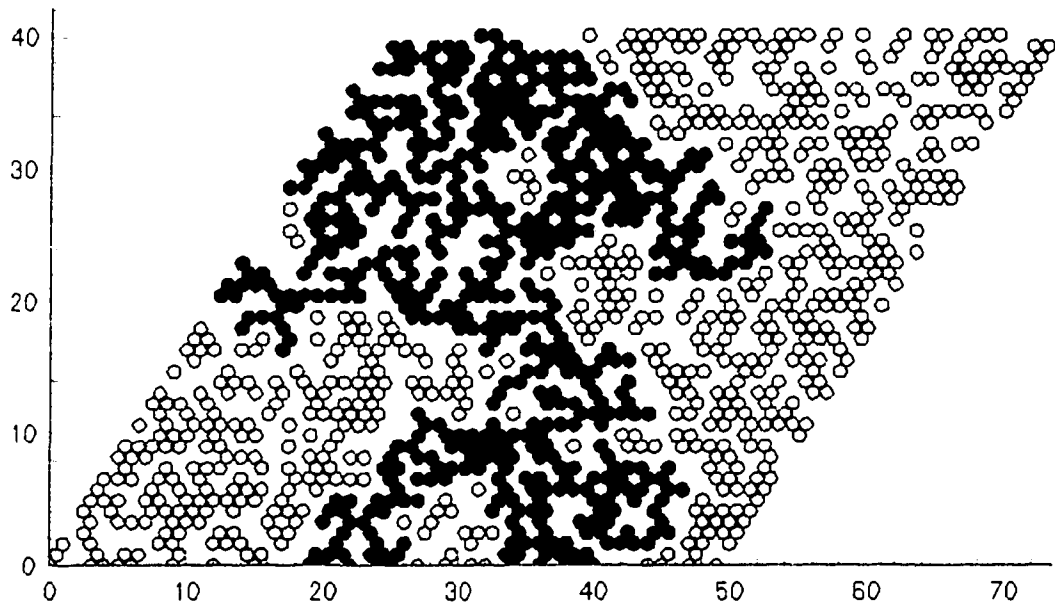


Figure 4.2: Percolation simulation results for 50x50 trigonal array. Calculated percolation threshold  $p_c = 49.1\%$ .

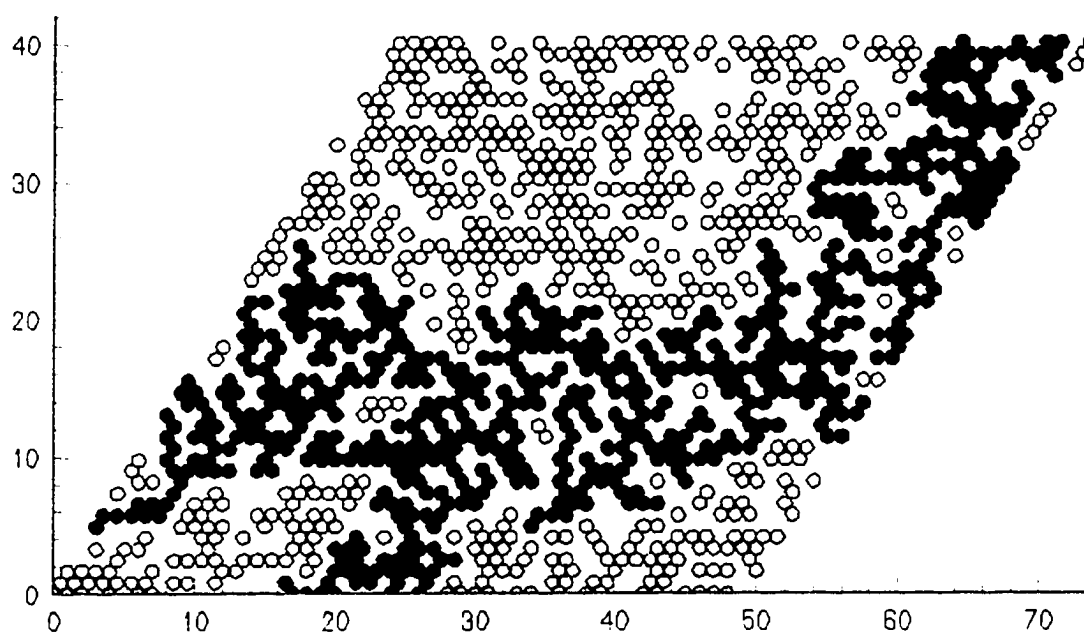


Figure 4.3: Percolation simulation results for 50x50 trigonal array. Calculated percolation threshold  $p_c = 49.96\%$ .

Table 4.1: Calculated results of average percolation threshold and standard deviation for trigonal lattices.

Lattice Size	10x10	15x15	20x20	25x25	30x30	35x35	40x40	45x45	50x50
$\bar{p}_c$	0.516	0.515	0.514	0.505	0.498	0.497	0.4997	0.4996	0.502
$\sigma$	0.078	0.055	0.056	0.043	0.040	0.034	0.034	0.028	0.025

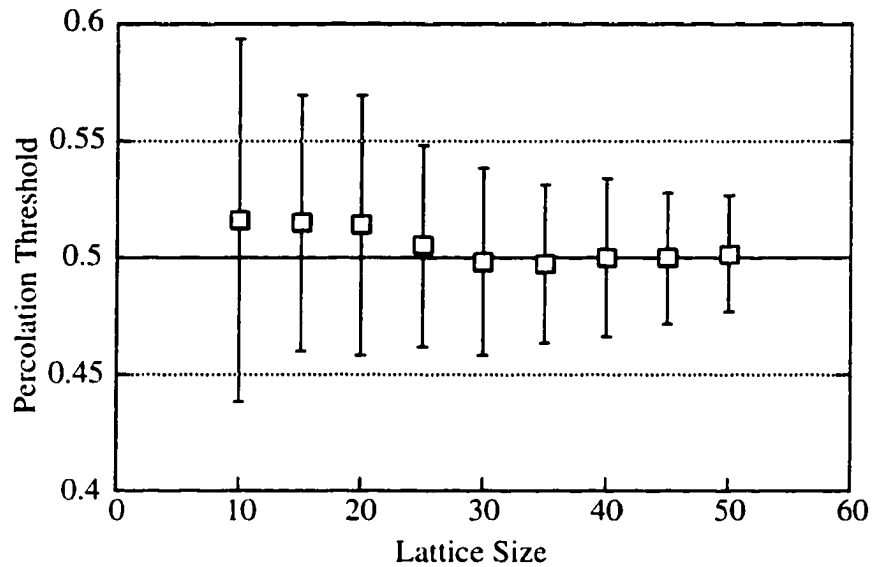


Figure 4.4: Graph of calculated average percolation threshold and standard deviation for trigonal lattices.

the vertical direction.

The finite size of the simulation has introduced some errors into the calculation. It is known that the percolation threshold for a trigonal lattice is  $p_c = 0.5$  exactly [1]. The values calculated in Figures 4.1 thru 4.3 are seen to closely approximate this value, with an error of less than 2%.

The results of repeated simulation runs for the 50x50 array give an average  $\bar{p}_c = 0.502$  with  $\sigma = 0.025$ . Table 4.1 and Figure 4.4 show the average percolation threshold and standard deviation for various lattice sizes. The results clearly converge to the exact value of 0.5.

The agreement between the known exact value of  $p_c$  and the value calculated through the Monte Carlo simulation described above gives confidence in the model and enables its use as a building block in more complicated calculations as described below.

## 4.2 Three-Dimensional Percolation Simulation

The two dimensional percolation model described in the previous section can be expanded into three dimensions in a straight forward manner. Particles are again randomly added to an underlying lattice, with conduction only between nearest neighbor occupied sites. For this work the hexagonal close-packed (hcp) lattice was used. This lattice describes one of the natural stacking arrangements for hard spheres and is therefore appropriate for the consideration of spherical iron particles in a noninteracting matrix. The lattice is constructed by first stacking two dimensional trigonal arrays directly above each other to form a hexagonal lattice. Two such hexagonal lattices are then interpenetrated to form the hexagonal close-packed lattice. The second hexagonal lattice is displaced from the first such that each trigonal net rests in the depressions left in the center of every other triangle of the layer beneath it [20]. If the ratio of the height of the hexagonal array to the length of the lattice vector in the plane of the trigonal array  $c/a = \sqrt{8/3}$  the lattice is an ideal hcp structure. The ideal hcp lattice was used throughout this work.

Figure 4.5 displays a hcp lattice composed of five stacked 10x10 trigonal lattices. The number of nearest neighbors in this lattice, for sites not on a boundary, is twelve. This compares to six nearest neighbors in the two dimensional trigonal lattice. The increase in the number of nearest neighbors suggests that a smaller volume fraction of sites need to be filled in order for the system to percolate.

Figure 4.6 displays two views of the results for the calculation of the percolation

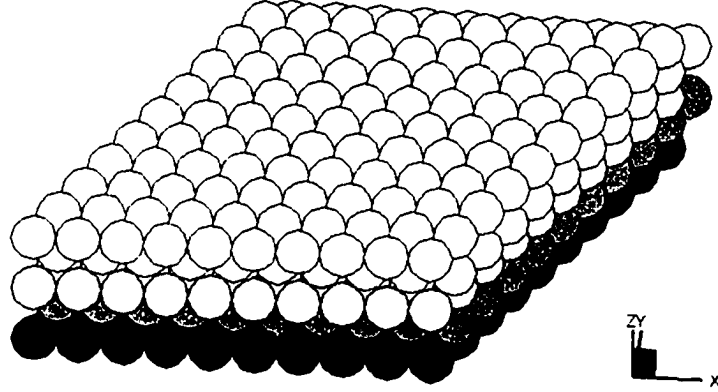


Figure 4.5: HCP lattice composed of five stacked 10x10 trigonal lattices.

threshold in a 4x4x4 hcp lattice. In this figure black circles correspond to the unfilled lattice sites. The particles which form the percolating network are drawn in white while other particles in the system are colored gray. The percolation criteria for this simulation was the formation of a connected network along the z-axis. Note that this system does not percolate along the x or y axes. The calculated percolation threshold of 28.12% is well below the 50% value obtained in the two dimensional simulation. The results of a second simulation run using the same percolation criteria are shown in Figure 4.7. Here the percolation threshold is calculated as 18.75%. This system is seen to percolate along both the y and z axes.

As in the two dimensional case, the finite lattice size introduces considerable errors into the calculation of  $p_c$ . In the two dimensional case it was shown in Table 4.1 and Figure 4.4 that increasing the lattice size reduces the variability of the calculation, with the calculated results converging to the true value of  $p_c$ . The corresponding data for the HCP lattice is shown in Table 4.2 and Figure 4.8. For lattice sizes above 15x15x15  $\bar{p}_c$  remains within 0.5% of 20% with the standard deviation decreasing with increasing lattice size. The percolation threshold for an infinite ideal HCP lattice

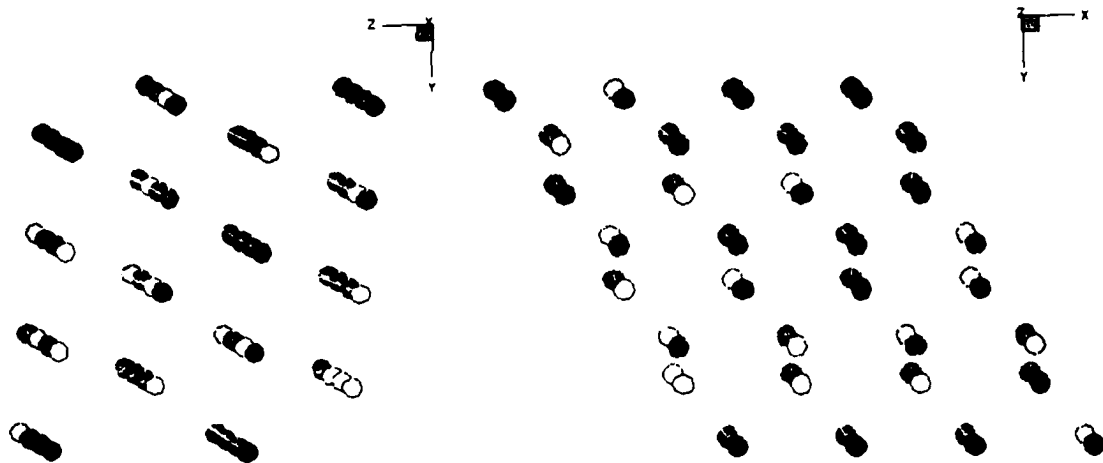


Figure 4.6: Percolation simulation results for 4x4x4 HCP array. Calculated percolation threshold  $p_c = 28.12\%$ .

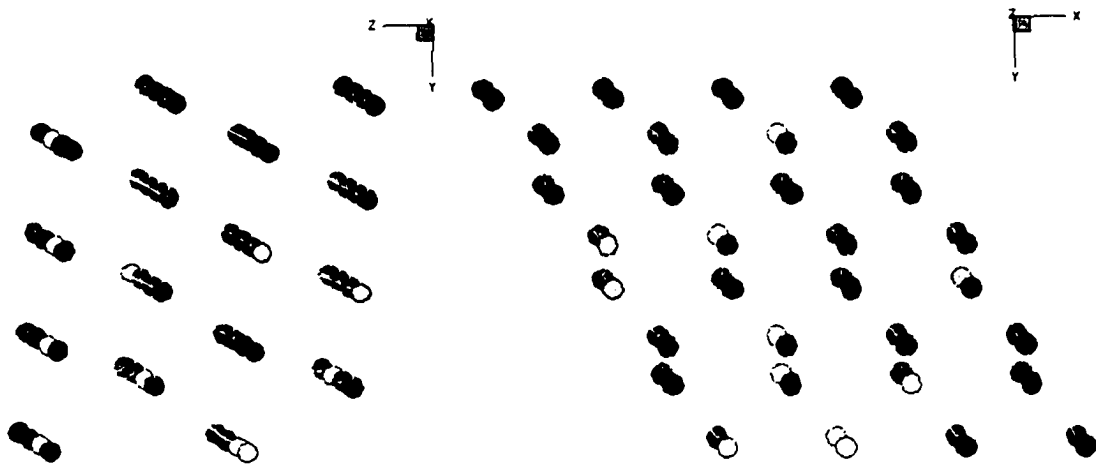


Figure 4.7: Percolation simulation results for 4x4x4 HCP array. Calculated percolation threshold  $p_c = 18.75\%$ .

Table 4.2: Calculated results of average percolation threshold and standard deviation for hexagonal close-packed lattices.

Lattice Size	10x10 x10	15x15 x15	20x20 x20	25x25 x25	30x30 x30	35x35 x35	40x40 x40	45x45 x45	50x50 x50
$\bar{p}_c$	0.215	0.206	0.204	0.204	0.203	0.201	0.201	0.201	0.201
$\sigma$	0.031	0.023	0.015	0.011	0.008	0.007	0.007	0.007	0.006

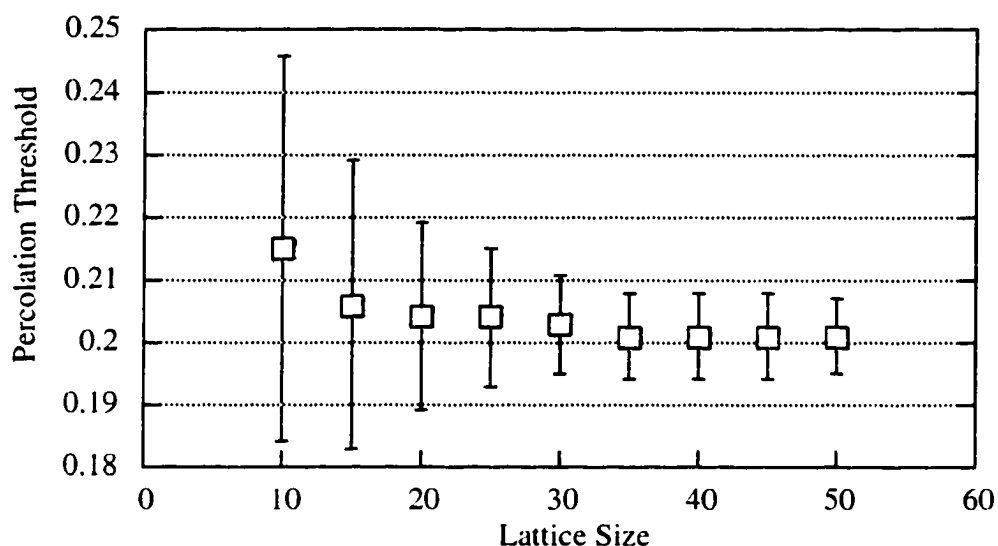


Figure 4.8: Graph of calculated average percolation threshold and standard deviation for HCP lattices.

is inferred by extrapolating the finite lattice data out to ever increasing lattice size. Using this approach the simulation data predicts a percolation threshold of approximately  $20.1\% \pm 0.6\%$  for an ideal HCP lattice. At an iron volume concentration well above this calculated value of  $p_c$  metallic conduction across the system is anticipated. Similarly, dielectric behavior is expected for iron volume concentrations well below 20%. Near the critical value  $p_c$  a transition between the two regimes should be seen.

The experimental work of the following chapter will concentrate on measuring the electronic transport properties across the percolation threshold in bulk iron polyimide composites. In particular, measurement of tunneling and hopping conduction

will be performed for samples with iron volume concentrations near the percolation threshold. First, the simulation model developed here will be used to predict some of these transport properties.

### 4.3 Resistance Calculations in Iron Polyimide Composites

The results from the previous sections can be built upon to provide a means for calculating the electronic transport properties in iron polyimide composites. In this section calculations of the sample resistivity at the percolation threshold are performed. In addition, a simple calculation for the tunneling magnetoresistance across a granular sample is presented based upon the results of the previous sections combined and those of Chapter 2.

The calculations in this section proceed directly from the two dimensional percolation calculations of Section 4.1. The network of conducting particles in the insulating matrix is analyzed using mesh current analysis [36]. An unknown current is assumed to flow clockwise around each triangle (mesh) of the lattice, as indicated in Figure 4.9. The total resistance around mesh  $i$  is represented as  $R_{ii}$ , and resistances in common between meshes  $i$  and  $j$  are labelled  $R_{ij}$ . The resistance across the network is a function of the resistance between nearest neighbor sites,  $R_{nn}$ . For this work the resistance in arbitrary units is taken as  $R_{nn} = 1$  if both sites are filled. If either of both of the neighboring sites are empty the resistance between the sites is taken as  $R = 10^6$ . It is now necessary to apply Kirchhoff's second, or voltage, law to each mesh of the circuit. Kirchhoff's voltage law states

$$\sum_j \varepsilon_j = \sum_k R_k I_k. \quad (4.1)$$

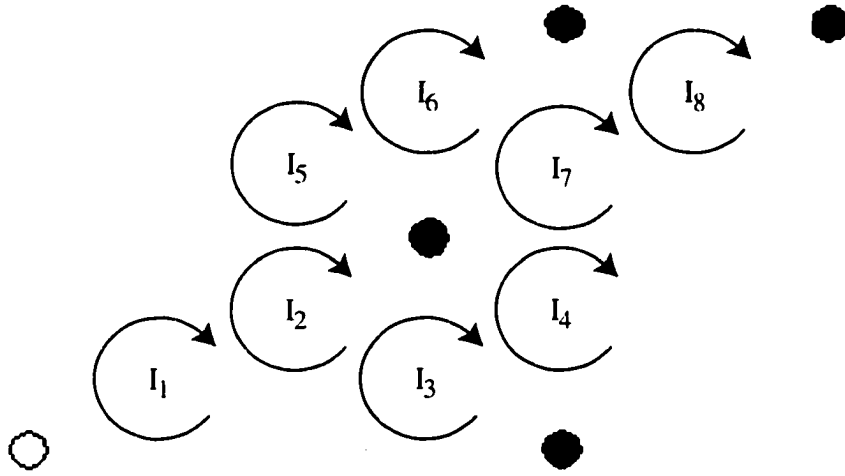


Figure 4.9: Mesh current analysis for 3x3 trigonal array.

Applying Kirchhoff's voltage law to the circuit of Figure 4.9 gives the set of equations

$$\begin{aligned}
 \varepsilon_1 &= R_{11}I_1 - R_{12}I_2 - R_{19}I_9, \\
 \varepsilon_2 &= -R_{21}I_1 + R_{22}I_2 - R_{23}I_3 - R_{25}I_5, \\
 \varepsilon_3 &= -R_{32}I_2 + R_{33}I_3 - R_{34}I_4, \\
 \varepsilon_4 &= -R_{43}I_3 + R_{44}I_4 - R_{47}I_7, \\
 \varepsilon_5 &= -R_{52}I_2 + R_{55}I_5 - R_{56}I_6 - R_{59}I_9, \\
 \varepsilon_6 &= -R_{65}I_5 + R_{66}I_6 - R_{67}I_7, \\
 \varepsilon_7 &= -R_{74}I_4 - R_{76}I_6 + R_{77}I_7 - R_{78}I_8, \\
 \varepsilon_8 &= -R_{78}I_8 + R_{88}I_8.
 \end{aligned} \tag{4.2}$$

In the case presented here the electromotive force around any mesh,  $\varepsilon_j$ , is zero. The driving force is external to the trigonal lattice, as drawn in Figure 4.10. This adds one additional mesh to the network and one corresponding equation to the set

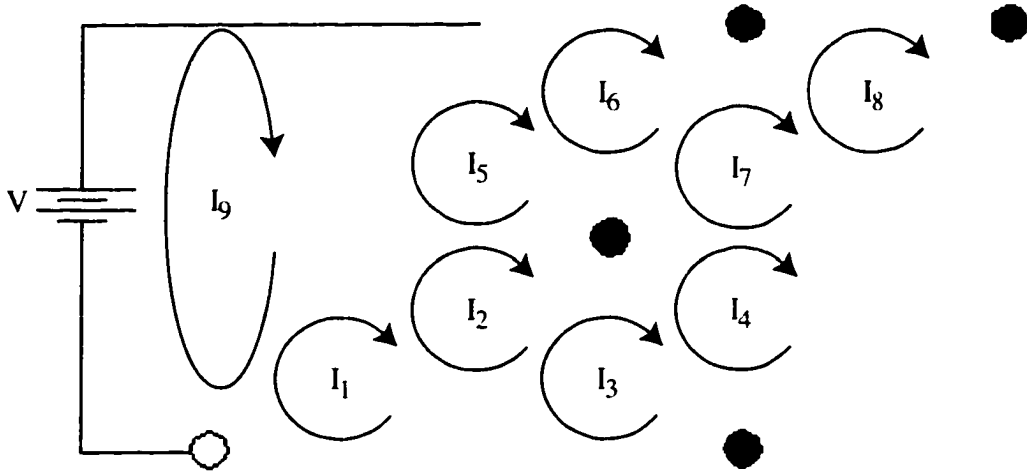


Figure 4.10: Mesh current analysis for 3x3 trigonal array with external drive.

of equation (4.2).

$$\varepsilon_9 = -R_{19}I_1 - R_{59}I_5 + R_{99}I_9. \quad (4.3)$$

A final point used for the calculation of the resistance across the lattice is to set the resistance between lattice points at the measurement boundaries equal to zero. For the lattice pictured in Figure 4.10 this would mean zero resistance along the top and bottom edges. Using these conventions the matrix equation for the network

voltage of Figure 4.10 is

$$\begin{pmatrix} 0 \\ 0 \\ 0 \\ 0 \\ 0 \\ 0 \\ 0 \\ 0 \\ 0 \\ V \end{pmatrix} = \begin{pmatrix} 2 \times 10^6 & -10^6 & 0 & 0 & 0 & 0 & 0 & 0 & -10^6 \\ -10^6 & 3 \times 10^6 & -10^6 & 0 & -10^6 & 0 & 0 & 0 & 0 \\ 0 & -10^6 & 1 + 10^6 & -1 & 0 & 0 & 0 & 0 & 0 \\ 0 & 0 & -1 & 1 + 2 \times 10^6 & 0 & 0 & -10^6 & 0 & 0 \\ 0 & -10^6 & 0 & 0 & 3 \times 10^6 & -10^6 & 0 & 0 & -10^6 \\ 0 & 0 & 0 & 0 & -10^6 & 1 + 10^6 & -1 & 0 & 0 \\ 0 & 0 & 0 & -10^6 & 0 & -1 & 1 + 2 \times 10^6 & -10^6 & 0 \\ 0 & 0 & 0 & 0 & 0 & 0 & -10^6 & 2 \times 10^6 & 0 \\ -10^6 & 0 & 0 & 0 & -10^6 & 0 & 0 & 0 & 2 \times 10^6 \end{pmatrix} \begin{pmatrix} I_1 \\ I_2 \\ I_3 \\ I_4 \\ I_5 \\ I_6 \\ I_7 \\ I_8 \\ I_9 \end{pmatrix}. \quad (4.4)$$

In order to calculate the resistance across the lattice the drive voltage is taken to be unity and the unknown mesh currents are solved for by multiplying through by the conductance matrix  $[G] = [R]^{-1}$ . The resistance across the lattice is given by  $R_l = V_9/I_9$ . Since all elements of the voltage vector are zero except for  $V_9 = 1$ ,  $I_9 = [G]_{99}$  and  $R_l = [G]_{99}^{-1}$ .

For the resistance matrix in equation (4.4)  $[G]_{99} = 800003/1600000$ . This gives the calculated lattice resistance as  $R_l = [G]_{99}^{-1} = 1.9999925$ . In this case the resistance across the lattice shown in Figure 4.10 is easily found by inspection to be exactly 2.0. The calculated results are seen to be quite accurate, although the use of a finite resistance between unoccupied sites on the lattice causes the mesh current analysis to slightly underestimate the resistance across the lattice. The error is extremely small, less than 0.003% in this case.

Although the example performed above is a trivial case, the methodology can be systematically extended to an arbitrary size lattice. The only constraint here is the required computer memory which can be quite high. The size of the matrix to be inverted, for an  $n$  by  $n$  lattice, is  $1 + 2(n - 1)(n - 1)$ , or approximately  $2(n - 1)^2$  for

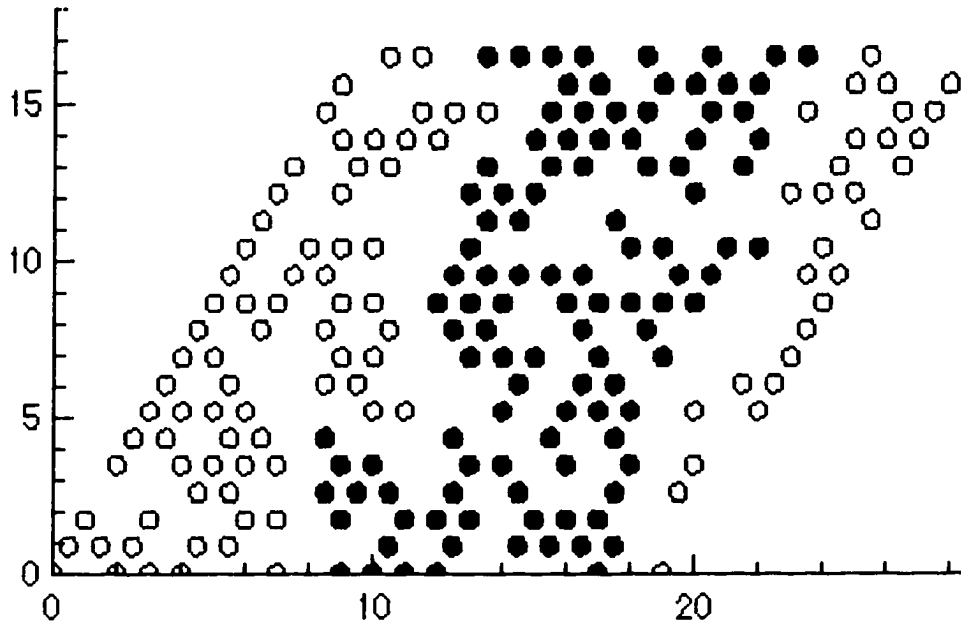


Figure 4.11: Percolation simulation for 20x20 trigonal lattice. Calculated  $p_c = 52.5\%$  and calculated  $R/R_{nn} = 13.4$ .

large  $n$ . The inversion of a matrix by standard methods requires loading the entire matrix in RAM. For a  $2(n-1)^2$  by  $2(n-1)^2$  matrix this necessitates the storage of  $4(n-1)^4$  double precision floating point numbers. For a 32 bit processor this equates to roughly 185 Mbytes of RAM for a 50x50 trigonal lattice, and 3.1 Gbytes for a 100x100 lattice. In this work the maximum lattice size was limited to 45x45 in order to accommodate the accessible computer systems.

Figures 4.11 and 4.12 display the percolation simulation and resistance calculation results from two separate runs on a 20x20 trigonal lattice. In each case the resistance is calculated along the vertical axis and is normalized to the resistance between nearest neighbor occupied sites.

The calculated resistance as a function of grid size is given in Figure 4.13. This graph displays the calculated mean resistance and standard deviation for ten separate

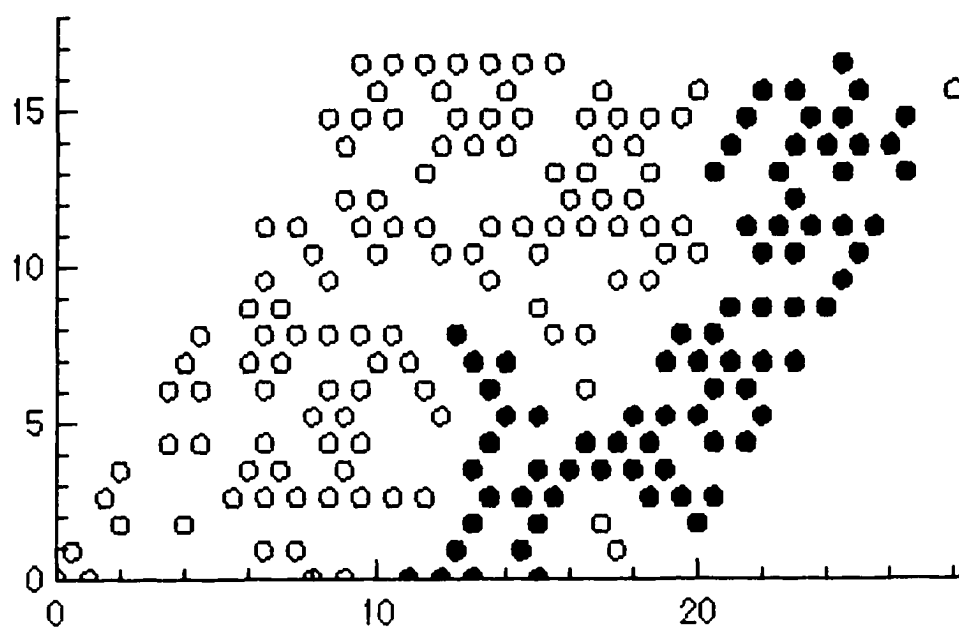


Figure 4.12: Percolation simulation for 20x20 trigonal lattice. Calculated  $p_c = 48.25\%$  and calculated  $R/R_{nn} = 19.5$ .

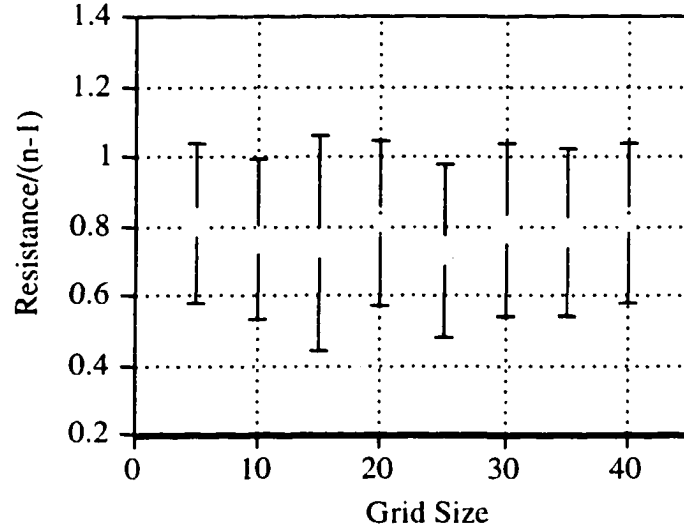


Figure 4.13: Calculated resistance as a function of grid size.

runs at each grid size. The values are divided by the number of possible bonds along an edge of the mesh,  $n-1$ , showing that the resistance scales roughly linearly with the grid size.

## 4.4 Model and Simulation Results for Tunneling Magnetoresistance

Calculation of tunneling effects are incorporated into the model of Section 4.3 using the results of Chapter 2. The resistance between neighboring sites is no longer fixed but related to the nearest neighbor magnetization directions by

$$G = G_{fbf}(1 + P_{fb}^2 \cos \theta). \quad (2.14)$$

The resistance between sites when either or both of the sites is empty is again taken as  $R = 10^6$ , or  $G = 10^{-6}$ . In equation (2.14),  $G_{fbf}$  and  $P_{fp}$  are defined in Chapter 2 to be the mean ferromagnet-barrier-ferromagnet tunneling conductance and the effective

ferromagnet-barrier spin polarization, respectively. As discussed in Chapter 2 several values of the effective spin polarization have been reported. For iron reported values range from 0.45 [3] to 0.19 [4]. The work of J. M. Maclaren indicates that the value of  $P_{fb}$  is not constant but dependent upon both the barrier height and thickness [5]. These results are summarized in Table 2.2 and Figures 2.4 - 2.5.

An initial estimate of the tunneling magnetoresistance across the iron polyimide composite samples of the current study was performed by incorporating equation (2.4) into the computer simulation discussed above. A fixed value of  $P_{fb} = 0.264575$ ,  $P_{fb}^2 = 0.07$ , was chosen for the effective ferromagnet-barrier spin polarization. This value of  $P_{fb}$  lies within the range detailed above and agrees with early experimental measurements of the conductance variation across a single tunneling junction [2].

The calculation of the resistance across the lattice was performed at the calculated percolation threshold with the assumption that the resistance between nearest neighbor occupied sites follows the form of equation (2.14). The calculation of the resistance in the unmagnetized state was performed by assigning a random direction to the magnetization vector at each site. The calculation was then performed a second time with all magnetization vectors aligned along a fixed axis. The simulation results for the tunneling magnetoresistance is then simply given by

$$\frac{\Delta R}{R} = \frac{(R_{B=Bmax} - R_{B=0})}{R_{B=0}} \quad (4.5)$$

where  $B = Bmax$  is the state with all magnetization directions aligned and  $B = 0$  is the state with random orientation of the magnetization vectors.

Table 4.3 reports the calculated tunneling magnetoresistance across two-dimensional iron polyimide composite samples at the iron percolation threshold. The table also individually reports the resistance of the unmagnetized and magnetically saturated states. In each case the data were averaged over twenty consecutive runs at each grid

Table 4.3: Calculated tunneling magnetoresistance in two dimensional iron polyimide composites at the percolation threshold.

Lattice Size	10x10	15x15	20x20	25x25	30x30	35x35	40x40	45x45
$R_{B=0}$	6.68	10.09	13.50	17.14	20.97	24.41	26.57	33.89
$\sigma$	2.09	3.22	4.73	4.63	6.77	8.59	9.30	9.77
$R_{B=B_{max}}$	6.22	9.45	12.59	15.96	19.53	22.72	24.81	31.59
$\sigma$	1.92	3.03	4.41	4.33	6.28	7.96	8.69	9.10
$\Delta R/R_{B=0}$	0.067	0.064	0.067	0.070	0.068	0.069	0.066	0.068
$\sigma$	0.012	0.011	0.009	0.006	0.007	0.006	0.006	0.005

size. The calculated magnetoresistance is seen to remain nearly constant across the range of grid sizes, with the standard deviation of the calculated results decreasing with increasing grid size.

Figure 4.14 displays a plot of the tunneling magnetoresistance tabulated in Table 4.3. The percentage change in resistance is nearly constant across the various grid sizes. The average value of 6.74% is shown on the graph as a dashed line. This value of the TMR is significantly less than given by equation (2.3), rewritten below.

$$\frac{\Delta G}{G} = \frac{G_{\parallel} - G_{\#}}{G_{\parallel}} = \frac{R_{\#} - R_{\parallel}}{R_{\#}} = \frac{2PP'}{1 + PP'} = \frac{2P^2}{1 + P^2}. \quad (2.3)$$

In this equation the value of  $P^2 = 0.07$  yields  $\Delta R/R = 13.1\%$ . This value is roughly twice that calculated by the simulation model presented above. The difference corresponds to the absence of a forced antiferromagnetically aligned state between neighboring particles in the computer simulation. The results tabulated in Table 4.3 and plotted in Figure 4.14 correspond to the difference between a random spin orientation across the sample and the magnetically saturated state. Equation (2.3) gives the maximum change in conductance across the barrier, corresponding to tunneling between ferromagnetic and antiferromagnetic alignment between the ferromagnetic layers. Such an alignment will occur if the coercive field of the material on either side of the barrier is different. As the system is cycled through a hysteresis loop

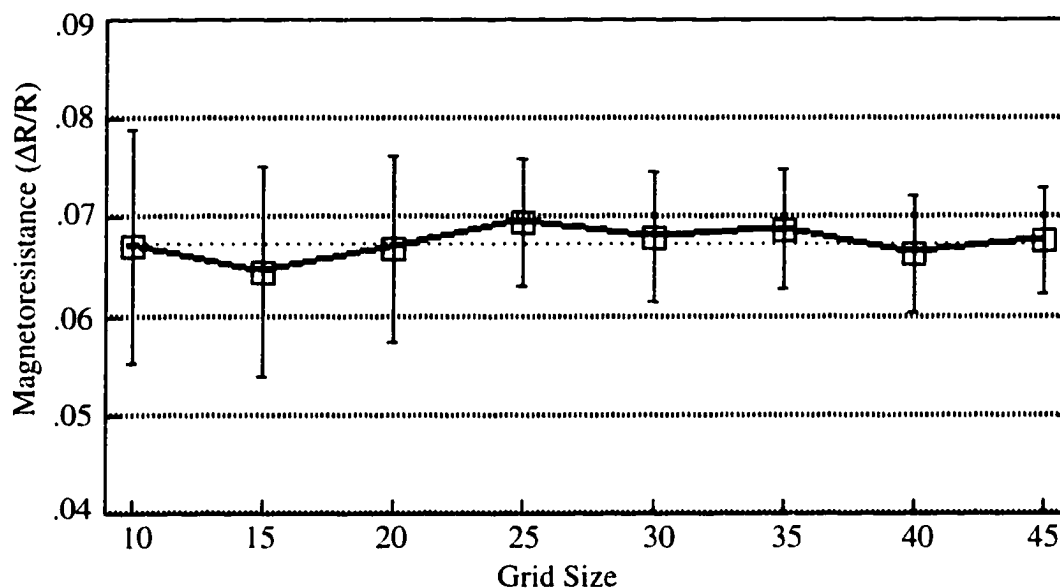


Figure 4.14: Calculated magnetoresistance as a function of grid size.

the softer material will reverse its magnetization direction at a lower field level. The magnetic moment of the harder layer will remain in opposition to the applied field until the larger coercive field is applied. The field region between the two coercivities will then correspond to an antiferromagnetic alignment of the two magnetic layers. The presence of an antiferromagnetically aligned state between neighboring sites is unlikely to occur in the iron polyimide composites of the present study, resulting in a predicted maximum TMR of roughly 1/2 that given by the calculations of chapter 2.

# Chapter 5

## Experiment

The theoretical model for electronic conduction in iron polyimide nanocomposites presented in the previous chapters predicts some very interesting transport properties in these systems. In particular, tunneling magnetoresistance and variable range hopping conduction are anticipated for samples fabricated at iron volume concentrations near the percolation threshold. In this chapter a sample fabrication procedure is developed and the experimental methods for identification of tunneling magnetoresistance and variable range hopping are described.

The important first step in detecting TMR and VRH in iron polyimide composites is the sample fabrication procedure. Whereas most research in TMR materials has focused on thin film multilayers [7-10], the sample fabrication procedure incorporated here is compression molding of fine ferromagnetic powders in a nonconducting polyimide matrix. Compression molded TMR devices may have significant advantages over sputtered systems, including ease of fabrication and lowered production costs. The first section of this chapter will detail this unique approach to TMR material fabrication.

A detailed study of the physical properties of compression molded iron poly-

imide composites will follow the sample fabrication procedure. Experimental methods for the measurements of the density, particle distribution, magnetization, and magnetoresistance are presented. In addition, experimental measurements for the temperature dependence of the conductance and magnetoconductance are described.

A critical variable in determining the magnitude of the TMR is the average iron particle separation distance. This separation distance, equivalent to the barrier thickness described in chapter 3.3, is dependent upon several sample fabrication parameters including iron particle size and premolding material processing. In the final section of this chapter a technique utilizing high energy ball milling to optimize this tunneling distance will be described.

## 5.1 Sample Fabrication Procedure

Iron polyimide composites were manufactured through ball milling and compression molding of powdered Fe with a high performance polyimide [13] in powdered form. The commercially available Fe powder has a nominal purity of 99.5 at. % and particle size of 6 – 10 $\mu$ m [37]. Samples with Fe volume fractions of 0.15, 0.20, 0.23, 0.28, 0.34, 0.44, 0.54, and 0.64 have been prepared by combining the appropriate amounts of Fe and polyimide in a hardened steel vial with two 6 mm diameter stainless steel balls with a ball-to-powder weight ratio of 1:5. The vial was sealed in an argon atmosphere to minimize oxidation of the iron. The material was then milled for 10 minutes in a SPEX model 8000-D high energy ball mill. Research performed by other authors has shown that a similar milling procedure with a higher ball-to-powder weight ratio and longer milling times can be used to reduce micron sized particles into nanophase materials [38, 39]. The primary goal here is to guarantee a complete mixture of the two powders and only secondarily to reduce the iron particle size. After ball milling, the powder was removed from the vial and poured into a mold. The

bulk sample was prepared by compression molding the mixed powders at 300° C for 30 minutes under 3.5 MPa of external compressive load. The sample size as removed from the mold was approximately  $2.5 \times 2.5 \times 0.6 \text{ cm}^3$ .

The density of the samples is measured by applying Archimedes' principle [40]. The mass of the sample is measured twice, first in air and then with the sample submerged in de-ionized water. According to Archimedes' principle the buoyancy, measured as the difference between the weight in air and in water, is equal to the weight of the fluid that the body displaces. This can be restated by dividing through by the constant  $g$ . In this form Archimedes' principle states that the difference in mass between the two measurements is equal to the mass of the fluid that the body displaces. The volume of the fluid displaced is then found by dividing the mass of the fluid by its density. For high purity de-ionized water the density is 1.0 gm/cc so that the density of the sample is given by

$$\rho = \frac{m}{V} = \frac{m_a}{m_a - m_w}. \quad (5.1)$$

Figure 5.1 displays the experimentally measured density of the as molded samples along with the full packing density, calculated by summing the product of the volume fraction of the polyimide and its density ( $\rho = 1.376 \text{ gm/cc}$ ) with the volume fraction of iron and its density ( $\rho = 7.86 \text{ gm/cc}$ ). It is clear from this data that the samples with Fe volume fractions less than 50% are tightly packed, while some voids exist in the higher iron volume percentage samples. It has previously been found that a much higher molding pressure is required in order to obtain complete packing in samples with high iron volume percentages [41, 42].

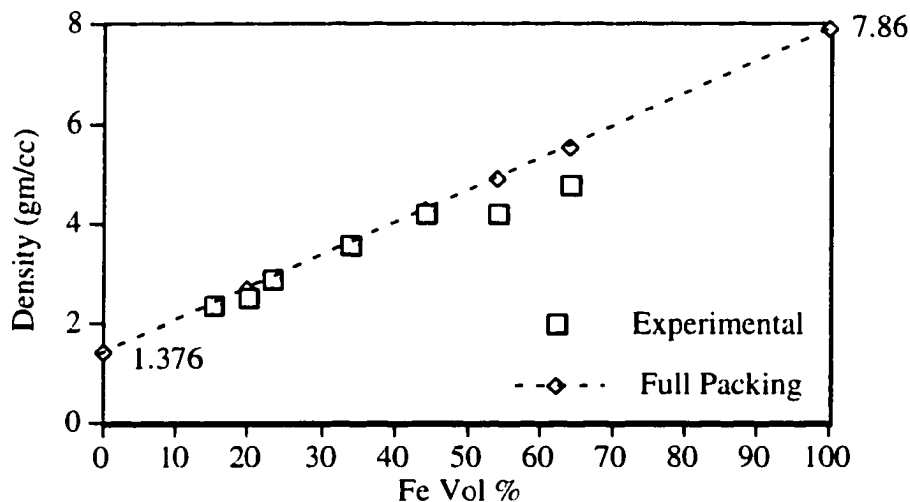


Figure 5.1: Experimentally measured density and full packing density as a function of iron volume percent for iron polyimide composite samples

## 5.2 Optical and Scanning Electron Microscopy

Optical micrographs of the samples were acquired using a Leica model MEF4M microscope. The as molded samples were hand polished to a smooth surface by dry sanding, the final stage using 2400 grit sandpaper. Optical microscopy can provide important information concerning iron particle size and distribution throughout the sample, but does not give definitive results for the elemental distribution of the materials. In order to verify the iron distribution throughout the sample scanning electron microscopy (SEM) has been performed. Scanning electron microscopy utilizes a finely focused electron beam to irradiate the sample under test. Images are typically formed by measuring the secondary electron (SE) or backscattered electron (BE) emission at each point across the scan area. An important feature of electron microscopy is the ability to perform elemental analysis on micron length scales. The x-rays emitted as a result of electron bombardment at a specific location on the sample can be analyzed with an energy dispersive x-ray spectrometer (EDS). Qualitative x-ray microanalysis

is performed by matching the detected x-rays to the known characteristic x-ray peaks of the elements [43].

### 5.3 Magnetic Force Microscopy Measurement System

Magnetic force microscopy (MFM) is a powerful tool for imaging surface magnetic fields at length scales down to 10 nm [44]. A subset of Scanning probe microscopy (SPM), MFM utilizes an atomically sharp probe to interact with the sample under test. The work described here was performed using a Digital Instruments Nanoscope IIIa scanning probe system with a MultiMode™ [45] microscope.

A schematic diagram of the experimental setup for MFM is displayed in Figure 5.2. The sample under test is mounted on a three axis piezoelectric tube scanner directly under the probe tip. During a scan the position of the probe tip, formed at the end of a cantilever, is monitored using a deflected laser beam. MFM is performed in TappingMode™ [45]. In this test configuration the cantilever is excited at its resonant frequency and the amplitude and phase of the tip oscillations are monitored. As the sample under test interacts with the probe tip a dampening of the oscillations will occur. The scanning probe microscope uses feedback from the photodetector output to change the vertical position of the sample such that the oscillations of the probe tip remain constant [44, 46].

In order to obtain an MFM image two interleaved scans are performed. The probe tip is first brought into contact with the sample and a scan line acquired. During this scan the atomic forces between the sample and the probe tip are responsible for tip deflections, and the topology of the sample is recorded. A second scan along the same line is then performed using LiftMode™ [45]. A fixed liftoff is added to the

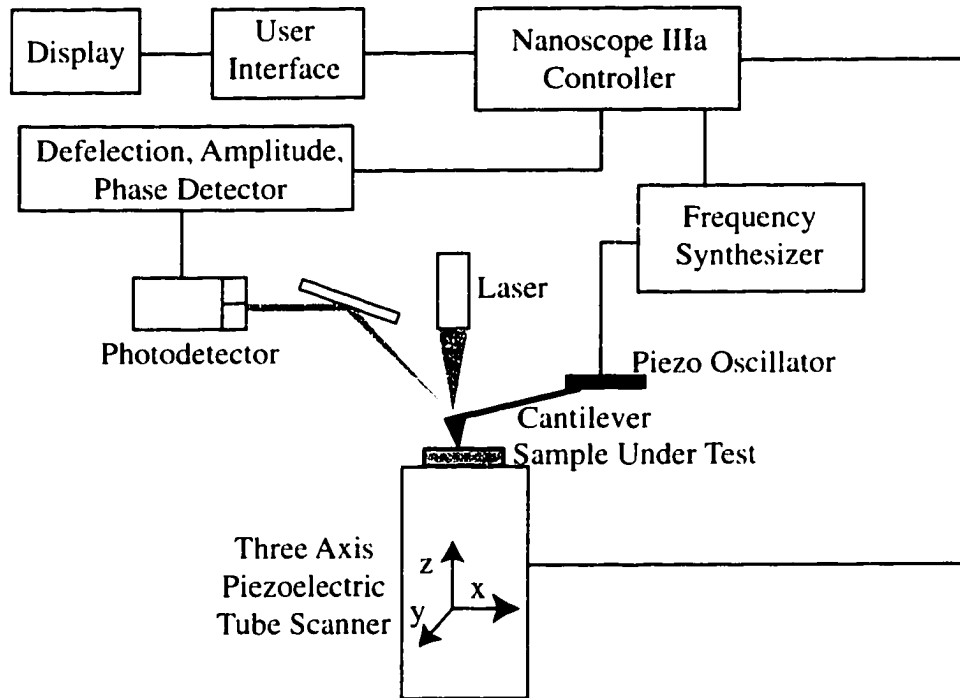


Figure 5.2: Schematic diagram of experimental setup for magnetic force microscopy.

measured topology for each scan point along the line. The liftoff, typically 50–200nm, is large enough to decouple atomic forces between the sample and the probe tip. The probe tip, however, is coated with a magnetic thin film and will thus be influenced by magnetic field gradients. Localized magnetic moments in the sample will create such field gradients at the probe tip location.

The MFM probe-sample interaction can be modeled as that of a vibrating mass in a magnetic potential,

$$V = \frac{k}{2}(x - h)^2 + U(h). \quad (5.2)$$

Here  $k$  is the spring constant of the cantilever,  $h$  is the height of the probe tip above the sample surface, and  $U(h)$  is the magnetic potential energy. The frequency shift caused by the interaction of the probe tip with magnetic sources in the sample is found by expanding the potential to second order about the potential minimum.

$$V = V_0 + (x - h) \left. \frac{\partial V}{\partial x} \right|_{x=x_0} + \frac{1}{2}(x - h)^2 \left. \frac{\partial^2 V}{\partial^2 x} \right|_{x=x_0} + \dots \quad (5.3)$$

As the potential is expanded about  $\left. \frac{\partial V}{\partial x} \right|_{x=x_0} = 0$ , and since a constant potential will not influence the dynamics of the problem, the potential can be written

$$V \approx \frac{1}{2}(x - h)^2 \left( k + \left. \frac{\partial^2 U}{\partial^2 x} \right|_{x_0} \right). \quad (5.4)$$

The lagrangian is thus given by

$$L = \frac{1}{2}m\dot{x}^2 - \frac{1}{2}(x - h)^2 \left( k + \left. \frac{\partial^2 U}{\partial^2 x} \right|_{x_0} \right) \quad (5.5)$$

and Lagrange's equation is

$$m\ddot{x} + (x - h) \left( k + \left. \frac{\partial^2 U}{\partial^2 x} \right|_{x_0} \right) = 0. \quad (5.6)$$

The solution to equation (5.6) is

$$(x - h) = e^{-i\omega t} \quad (5.7)$$

with  $\omega = \left( \frac{k}{m} + \frac{1}{m} \left. \frac{\partial^2 U}{\partial^2 x} \right|_{x_0} \right)^{1/2}$ .

Taking  $\omega_0 = \sqrt{k/m}$ , the frequency of oscillation can be written

$$\omega = \omega_0 \sqrt{1 + \frac{1}{k} \frac{\partial^2 U}{\partial^2 x}}. \quad (5.8)$$

Assuming that the frequency shift caused by the magnetic potential is small, the square root can be expanded as

$$\omega = \omega_0 \left( 1 + \frac{1}{2} \frac{1}{k} \frac{\partial^2 U}{\partial^2 x} + \dots \right) \quad (5.9)$$

$$\omega \approx \omega_0 + \frac{1}{2} \frac{\omega_0}{k} \frac{\partial^2 U}{\partial^2 x}, \quad (5.10)$$

such that

$$\Delta f \approx \frac{f_0}{2k} \frac{\partial^2 U}{\partial^2 x}. \quad (5.11)$$

In calculating  $U$ , the magnetization of the MFM probe tip can be estimated as that of a magnetic dipole of strength  $m_{eff}$  [47]. The magnetic potential is then given by [48]

$$U = -\vec{m}_1 \cdot \vec{B} = -\vec{m}_1 \cdot (-\nabla \phi_m) = \vec{m}_1 \cdot (\nabla \frac{\vec{m}_2 \cdot \vec{x}}{r^3}). \quad (5.12)$$

Here  $m_1$  is the moment of the probe tip and  $m_2$  is the moment of the particle under test. For the specific case  $m_1 \parallel m_2 \parallel \vec{x}$ ,

$$U_x = \vec{m}_1 \cdot \nabla \frac{\vec{m}_2}{x^2} = -\frac{2m_1 m_2}{x^3}. \quad (5.13)$$

Substituting equation (5.13) into (5.11) yields,

$$\Delta f \approx -\frac{12f_0 m_1 m_2}{kx^5}. \quad (5.14)$$

Several of the variables in equation (5.14) are available in the literature. The value of  $m_1$  has been estimated from equation (5.11) based upon measured frequency

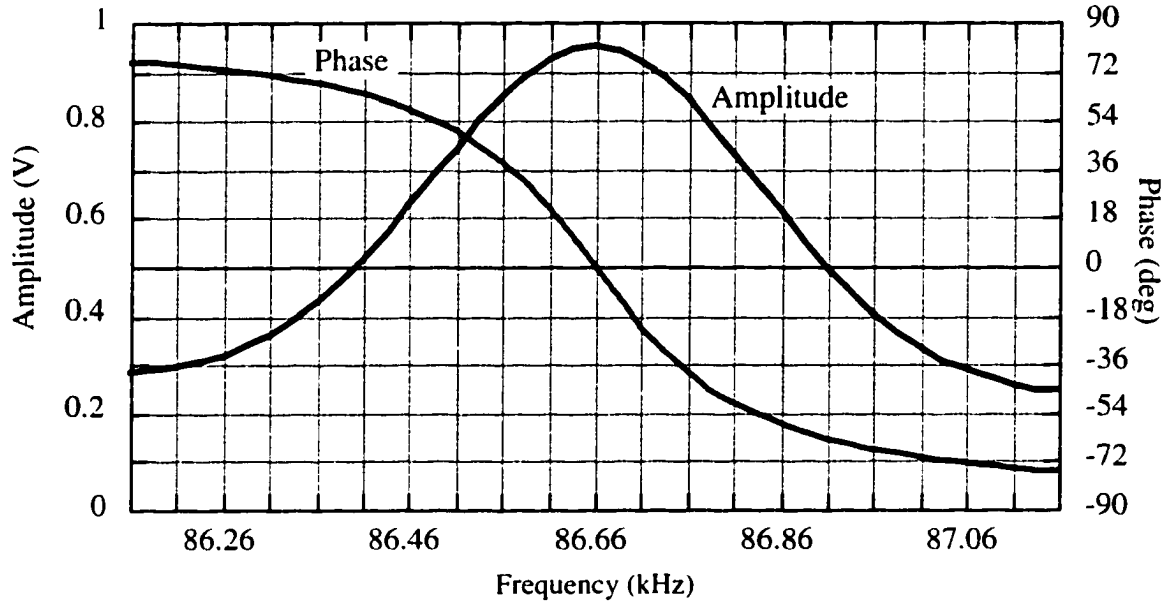


Figure 5.3: Amplitude and phase of cantilever oscillation as a function of drive frequency.

shifts from a known magnetic source [47, 49]. The cited works give  $m_1 \approx 10^{-12}$  emu. The value of the spring constant  $k$  is also found in the literature as  $k \approx 5 \times 10^3$  dyne/cm [46, 47].

The resonant frequency of the MFM cantilever was experimentally measured by monitoring the cantilever vibration amplitude and phase as a function of drive frequency using the experimental setup shown in Figure 5.2. Figure 5.3 displays typical experimental results for the MFM probe tips used in this study. The resonance frequency of  $f_0 = 86.66$  kHz is clearly identified in the data.

The last unknown variables in equation (5.14) are  $m_2$ , the magnetic moment of the particle under test, and  $x$ , the distance between the probe tip and the magnetic particle. In the iron polyimide composites considered here the magnetic particles are iron. The magnetic moment of a small iron particle can be estimated as that of a uniformly magnetized sphere. The fields are dipolar both asymptotically and close to

the sphere, with magnetic dipole moment [48]

$$\vec{m} = \frac{4\pi a^3}{3} \vec{M}. \quad (5.15)$$

Here  $a$  is the radius of the sphere and  $\vec{M}$  is the magnetization inside the sphere. Using the iron saturation magnetization of  $M_s = 1.714$  emu/cc [50] and a particle diameter of 100 nm gives

$$m_2 = 1714 \text{ emu/cc} \cdot \frac{4\pi}{3} (0.5 \times 10^{-5} \text{ cm})^3 \approx 9 \times 10^{-13} \text{ emu}. \quad (5.16)$$

The value of  $x$  is found from the liftoff used in the interleaved magnetic force scan. Taking a liftoff of 200 nm and assuming the the surface of the iron particle is in the plane of the sample surface (with the particle center 50 nm below the surface), gives  $x = 250$  nm.

Substituting these values into equation (5.14) yields

$$\begin{aligned} \Delta f &\approx -\frac{12 \times 87 \times 10^3 \times 10^{-12} \times 9 \times 10^{-13}}{5 \times 10^3 (2.5 \times 10^{-5})^5} \\ &\approx -20 \text{ Hz}. \end{aligned} \quad (5.17)$$

Similarly, the frequency shift for a 1  $\mu\text{m}$  diameter particle scanned at 300 nm from the surface ( $x = 800$  nm) would be  $\Delta f \approx -60\text{Hz}$ .

The calculated frequency shift for a line scan across a 100 nm iron particle with a liftoff of 200 nm is displayed in Figures 5.4 and 5.5. The particle is assumed magnetically saturated, with  $m = \frac{4\pi a^3}{3} M_s$ . In Figure 5.4 the magnetization direction is taken perpendicular to the sample surface. Figure 5.5 shows the results when the magnetization direction is parallel to the surface and along the scan line. The calculation was performed with Mathematica<sup>TM</sup> using equation (5.11) and  $U$  given as in equation (5.12). The particle center is located at probe position zero.

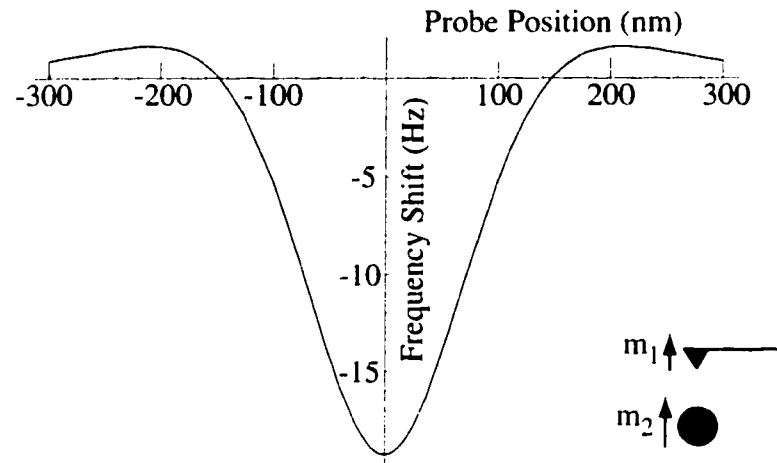


Figure 5.4: Calculated MFM frequency shift for 100 nm diameter iron particle with  $\vec{M}$  perpendicular to surface.

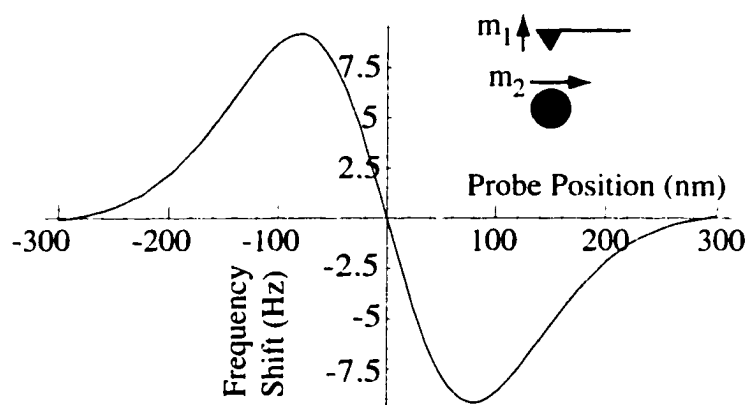


Figure 5.5: Calculated MFM frequency shift for 100 nm diameter iron particle with  $\vec{M}$  parallel to surface.

## 5.4 Magnetization Measurement System

Magnetization data on the iron polyimide samples was obtained using a vibrating sample magnetometer. A cube of  $0.25 \times 0.25 \times 0.25 \text{ cm}^3$  was cut from each of the original samples using a high speed diamond blade saw. Magnetization measurements were performed on these samples using a Lakeshore Model 7300 VSM and an iron core magnet with two inch pole faces. The samples were demagnetized before the applied field was ramped between  $\pm 1.0$  Tesla. A schematic diagram of the experimental setup is depicted in Figure 5.6.

A computer program was written in the Labview<sup>TM</sup> computer programming language to automate data acquisition, storage and retrieval.

## 5.5 Magnetoresistance Measurement System

Magnetoresistive data was acquired using a Linear Research Model LR700 A.C Resistance Bridge. Samples of dimension  $0.6 \times 0.6 \times 2.0 \text{ cm}^3$  were cut from the as

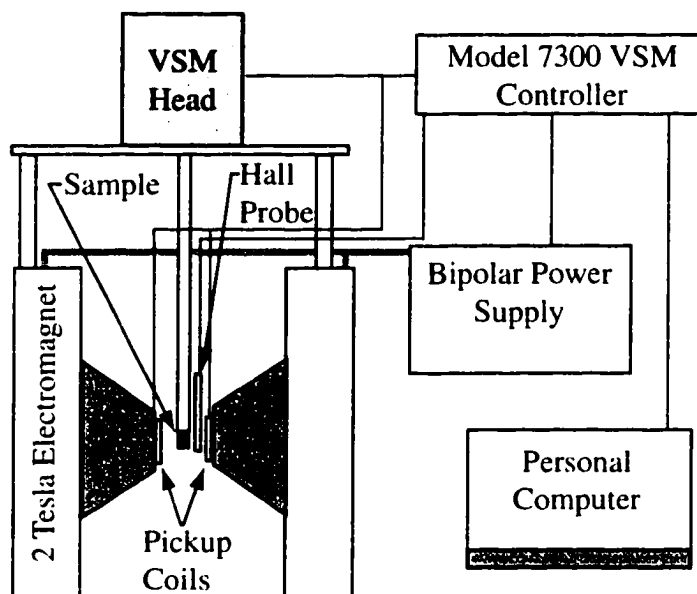


Figure 5.6: Experimental setup for magnetization measurements with vibrating sample magnetometer.

molded material using a high speed diamond blade saw. Electrical connections to these samples were made with a conductive silver epoxy in a four lead configuration. The resistance measurements were performed on the demagnetized sample and as an external field of  $\pm 0.5$  Tesla was applied along the long axis of the samples. A simplified schematic of the setup is displayed in Figure 5.7.

The Labview<sup>TM</sup> computer programming language was again used to control

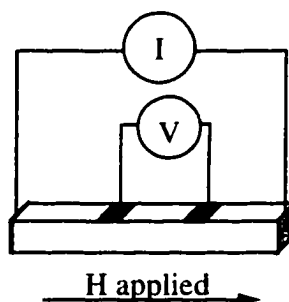


Figure 5.7: Simplified experimental setup for magnetoresistance measurements.

the experimental flow and automate data acquisition, storage and retrieval.

## 5.6 Experimental Setup for Temperature Dependence Measurements

The temperature dependence of the resistivity for the composite samples was determined using a CTI-Cryogenics Model 22 closed cycle helium refrigerator. Temperature measurements were performed using a copper-constantan thermocouple attached to the sample, and resistance measurements were acquired using a Linear Research Model LR700 A.C Resistance Bridge. Temperature and resistance data were acquired as the sample chamber was cooled from room temperature to a minimum of approximately 25 Kelvin, and then again as the sample was warmed back to room temperature. Minimal variation in the data was observed between the data acquired during cooling and warming cycles of the sample.

Magnetoresistance data was acquired at varying sample temperature by incorporating the variable temperature system described above with the magnetoresistance measurement system described in section 5.5. Figure 5.8 displays the experimental setup. The cryostat neck is mounted between the pole faces of the electromagnet. A Lake Shore model 805 temperature controller was used to maintain a constant temperature at the sample location. The controller measures the temperature and rate of change of the temperature in order to determine the input current to a heating element within the cryostat. The temperature set point is reached when equilibrium between the cooling power of the helium refrigerator and the heat input is achieved at the programmed temperature.

A comparison between Figures 5.7 and 5.8 shows that the sample orientation has been changed between the room temperature magnetoresistance measurements

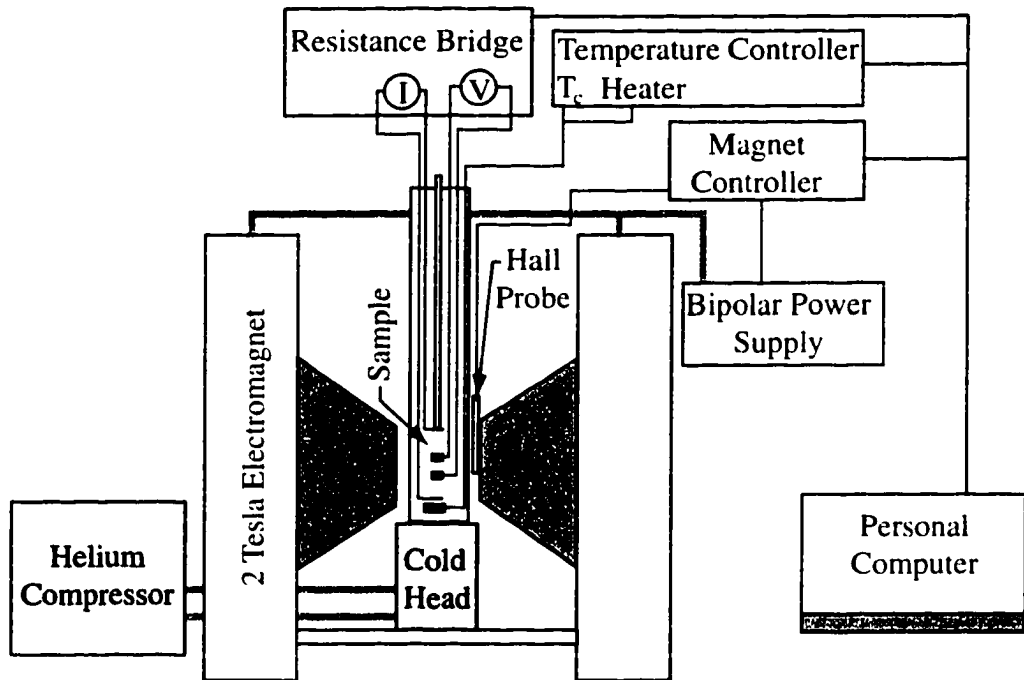


Figure 5.8: Experimental setup for measurement of temperature dependence of magnetoresistance.

performed in air and the variable temperature measurements taken within the cryostat. In the former case, the current flow and long axis of the sample were aligned with the applied field. In the latter, the current and long axis of the sample are perpendicular to the applied field. This change in sample orientation was required due to the limited space within the cryostat.

As in the previous sections, computer control of the experimental procedure was achieved over the IEEE bus using the Labview<sup>TM</sup> computer programming language.

## **5.7 Material Processing through High Energy Ball Milling**

In the preceding sections the fabrication and testing of iron polyimide nanocomposites has been described. This section describes a process designed to improve the magnetic field sensing qualities of the material. It has been shown that an important parameter in determining the change in resistance across a ferromagnet-insulator-ferromagnet junction is the insulator thickness. In the present study this corresponds to the distance of closest approach of neighboring particles. As shown in Figure 2.5, reducing the interparticle separation is predicted to greatly enhance the conductance ratio. In a randomly mixed composite this interparticle separation is related to the volume concentration of the conductor and the particle size. At a given volume fraction, a reduction in the particle size will reduce the average interparticle separation and is thus expected to increase the magnetoresistance of the material.

In an effort to increase the magnetoresistance of iron polyimide composites high energy ball milling of the powdered material was employed. High energy ball milling has been shown to be a viable technique to reduce the diameter of fine particles

[38, 39, 51]. As described above, a reduction in the iron particle size is expected to reduce the average interparticle separation and thereby increase the conductance ratio across the junction.

High energy ball milling was employed through the use of a SPEX model 8000-D shaker mill. Appropriate masses of iron and polyimide powders were combined in dual hardened steel vials with four 6 mm and two 12 mm diameter hardened steel ball bearings in each vial. The resulting ball to powder weight ratio was approximately 3:1. The vials were sealed in an argon filled glove bag to minimize oxidation of the iron. The sealed vials were then removed from the glove bag and loaded into the ball mill. Ball milling was performed for 4 and 8 hours on 2 separate powder mixtures, each with an iron volume fraction of 0.20. Small amounts of powder were extracted in an argon environment from the 4 hour sample after milling times of 1.2, and 3 hours. Magnetization measurements were performed on the milled powders using the vibrating sample magnetometer system discussed in section 5.4 and pictured in Figure 5.6.

Iron polyimide composite samples were fabricated through compression molding. As compared to the unmilled powders, a higher molding pressure was required in order to reach the full packing density. All milled samples were molded at 11 MPa as compared to 3.5 MPa for the unmilled materials.

# Chapter 6

## Results and Discussion

In this chapter the experimental methodologies introduced in the previous chapter are used to present experimental verification of tunneling magnetoresistance and variable range hopping conduction in iron polyimide nanocomposites. Optical, scanning electron, and magnetic force microscopy data are presented which indicate the presence of nanoscale tunneling junctions within composites fabricated with iron volume fractions near the percolation threshold. Electronic transport measurements on these samples show a clear peak in the magnetoresistance near the percolation threshold, in agreement with the theory of tunneling magnetoresistance. In addition, variable range hopping conduction is observed in the temperature dependence of the resistance for samples with iron volume fractions near the percolation threshold. Experimental data is also presented for the temperature dependence of the magnetoresistance, and the effect of material processing through high energy ball milling.

Throughout this chapter the experimental results are discussed in the context of the theories of variable range hopping and tunneling magnetoresistance, developed in chapters 2-4.

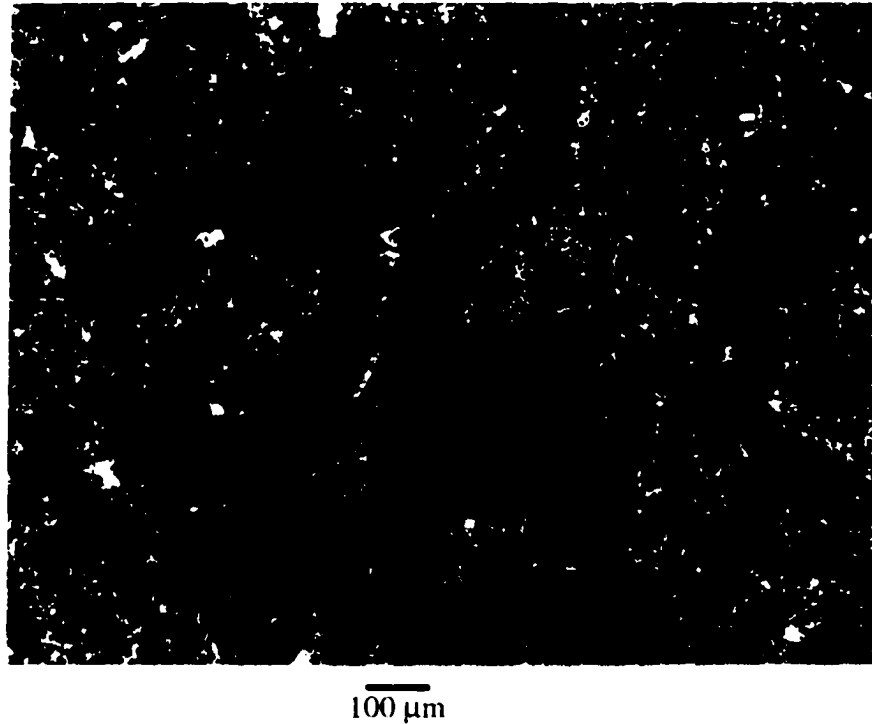


Figure 6.1: Optical micrograph of 20% Fe volume percent composite.

## 6.1 Microscopy Studies

Figure 6.1 displays an optical micrograph taken from the sample containing a 20% iron volume concentration. The iron particles appear bright in the reflected light image. On a large scale, the iron is seen to be well distributed throughout the sample. On a smaller scale, however, the iron particles appear to coalesce into networks of connected chains across the sample. This self arrangement of the iron particles is most likely due to an attractive magnetic force between neighboring ferromagnetic particles. The ferromagnetic particles will tend to align with the dipolar field in the material. Mixing of the ferromagnetic powder with the polyimide distributes the iron particles globally across the sample while the local attractive force has a tendency to

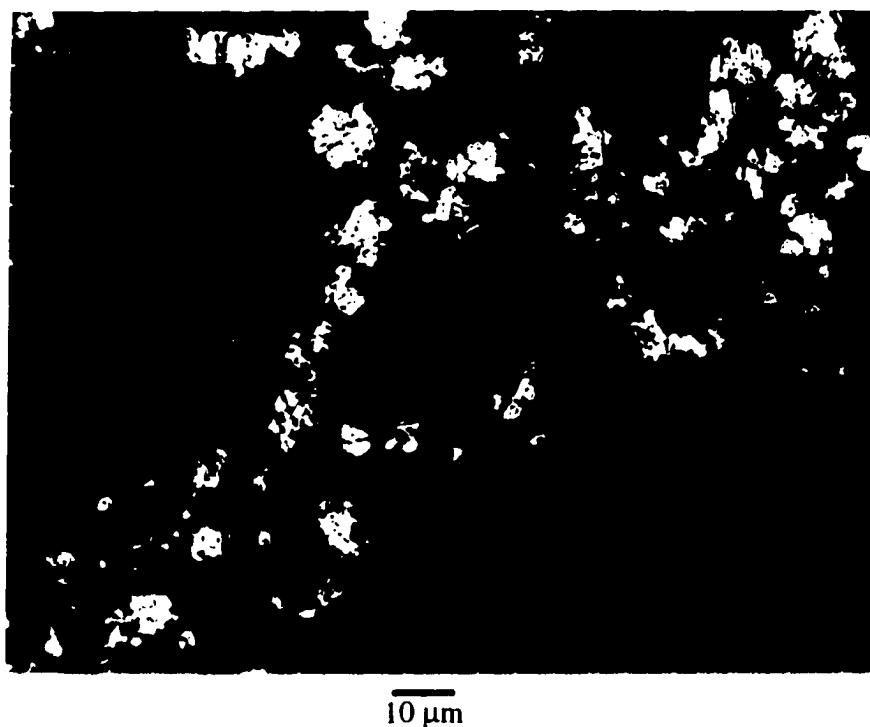


Figure 6.2: High magnification optical micrograph of 20% Fe volume percent composite.

align neighboring particles.

Figure 6.2 displays a higher magnification image of the same sample. The average particle size is seen to agree with the nominal size of approximately  $6\text{-}10\ \mu\text{m}$ . The chain like conduction paths across the sample are clearly evident in this figure.

The networks of contacting or nearly contacting iron particles observed in Figures 6.1 and 6.2 will carry the conduction electrons across the sample. Small gaps in these connected chains are the source of the tunneling gaps across which magnetoresistive and hopping effects will be observed.

Figure 6.3 displays a backscattered electron image along with an EDS map of iron across the scan area. The backscattered electron image looks very similar



Figure 6.3: SEM and EDS images of iron polyimide composite.

to the high magnification optical micrograph. For the SEM image an area with a large concentration of strong electron backscattering was chosen so as to make the EDS image easier to interpret. By comparing the EDS and backscattered image it is clear that the bright areas of the backscattered electron image correspond to areas of high iron concentration. The large bright area in the image corresponds to a cluster of iron particles with a cross sectional area of approximately  $500 \mu\text{m}^2$ . Much smaller individual iron particles with dimensions on order of  $1 \mu\text{m}$  are also identified in both the backscattered and EDS images. EDS on the darker, background areas of the backscattered image found the majority contribution to be from carbon, in agreement with the physical composition of the polyimide [13].

In order to isolate nanoscale particles and tunneling gaps between particles, magnetic force microscopy studies were performed. Figure 6.4 displays topographic and LiftMode<sup>TM</sup> magnetic force images for a 34% Fe Vol. composite sample acquired with the scanning probe microscope described in section 5.3. An applied magnetic field of  $\approx 2 \text{ kOe}$  was applied in the direction normal to the sample surface during data acquisition. The external magnetic field is used to rotate and saturate the

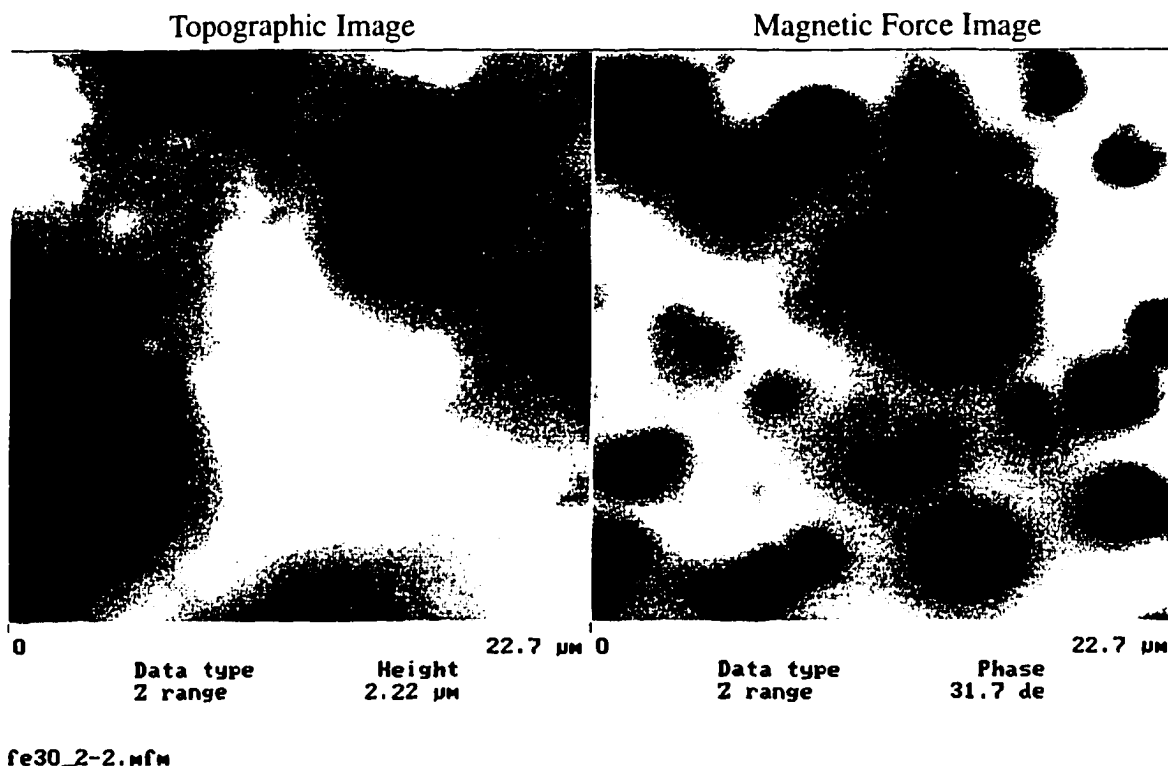


Figure 6.4: Scanning probe topographic and magnetic force images for 34% Fe Vol. sample. External field applied perpendicular to sample surface.

magnetization of the iron particles in the sample. The scan geometry for each particle is therefore equivalent to that shown in Figure 5.4, such that a drop in the frequency at the location of the center of the magnetic particles is anticipated.

With reference to Figure 5.2, the MFM data is displayed as a phase shift between the piezo oscillator driving the cantilever and the photodetector output measuring its displacement. The correlation between the measured phase shift and the theoretical frequency shifts calculated in section 5.3 is through the cantilever resonance curve shown in Figure 5.3. A close inspection of the data reveals a phase shift of approximately 0.5 degree/Hz at resonance.

The MFM graph in Figure 6.4 displays a phase range of approximately 30 degrees, corresponding to a 60 Hz frequency shift. The circular dark regions correspond to the magnetized particles which, by equation (5.14) will produce the observed negative frequency shifts. The size of the individual particles appears to be on the order of  $5 \mu\text{m}$ , consistent with the optical and scanning electron measurements of the previous section.

In the absence of an applied field the magnetization of the individual particles may not be given by the saturation value. In large particles magnetic domains will form to reduce the magnetostatic energy,  $(1/8\pi) \int_V H^2 dv$ , of the crystal [52]. The magnetic moment  $\vec{m}_2$  will then be proportional to the volume of the magnetic domain instead of that of the entire particle. If the particle size is sufficiently small, however, the increase in exchange energy between atoms with different magnetization directions will be greater than the reduction in magnetostatic energy achieved by forming a domain wall. The result will be a single domain particle. In this case equation (5.15) is correct (assuming spherical particles). Only the direction of the magnetization vector can change. The critical size for domain wall formation in iron has been estimated in the literature as  $\approx 30 \text{ nm}$  [52, 53]. As has been observed in the previous microscopy data, a large fraction of the particles are much larger than this critical size. It is anticipated, however, that the composite samples will contain some particles in this size range and therefore some single domain particles.

Figure 6.5 displays optical and MFM images over the same area in a 20% Fe. Vol. sample. A magnetic field of 2 kOe was applied normal to the sample surface and then removed before the MFM data were acquired. The iron particles are clearly evident in both figures, showing up as bright areas in the optical micrograph and areas of negative phase shift in the magnetic force image. The magnetic force data were acquired with a lift-off of 150 nm.

As previously mentioned, it is anticipated that intermixed with the large,  $\approx$

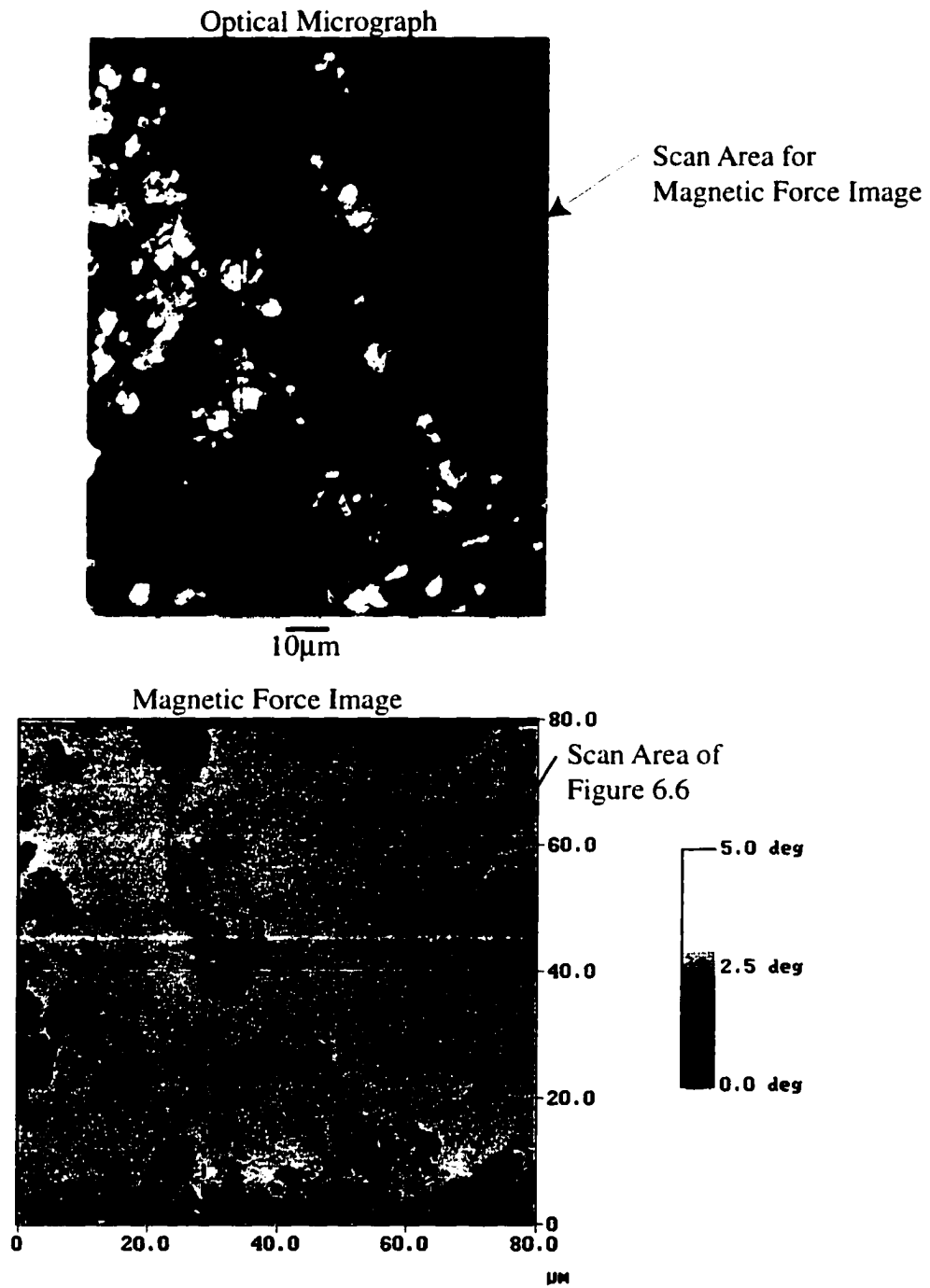


Figure 6.5: Optical and magnetic force images for 20% Fe Vol. sample. MFM data acquired in absence of external field.

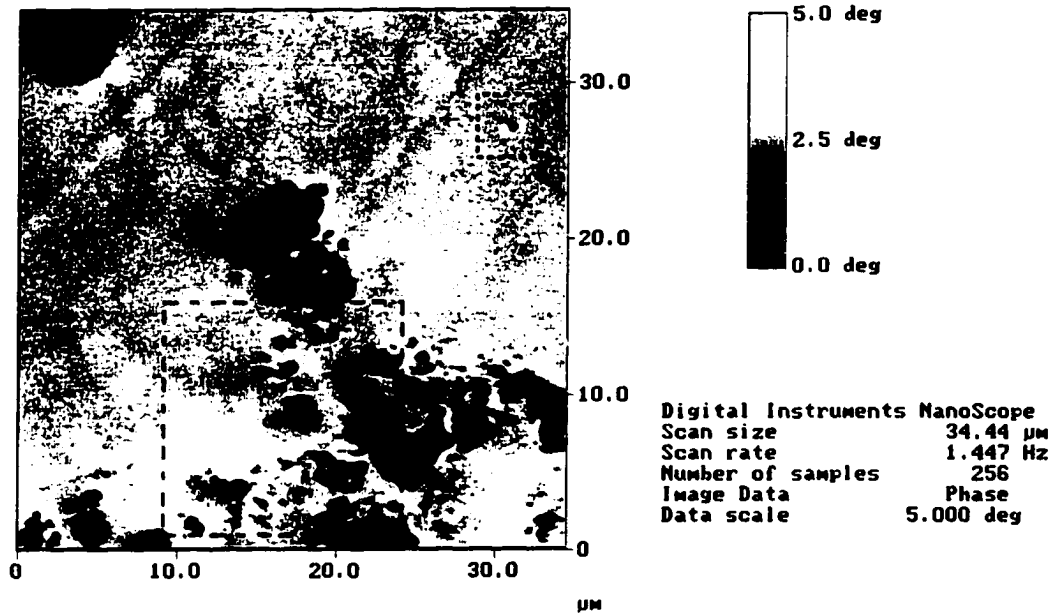


Figure 6.6: Magnetic force image of 20% Fe Vol. sample over  $35^2 \mu\text{m}^2$  area with 150 nm lift-off.

5  $\mu\text{m}$ . particles much smaller particles on the order of 10-100 nanometers exist in the iron polyimide composite samples. In section 3.3 it was found that particles in this size range will contribute to variable range hopping in the granular materials. In addition, it was shown in chapter 2 that tunneling magnetoresistance requires interparticle distances on this same length scale. The identification of such particles and interparticle gaps is shown in Figures 6.6 - 6.8. Each successive MFM image is taken at an increased magnification from the preceding figure, beginning with the 80  $\mu\text{m}$  scan of Figure 6.5.

The high resolution of the magnetic force microscope data in Figures 6.6 - 6.8 has imaged several particles with length scales on the order of 100 nm. In the upper right hand corner Figure 6.6 an isolated single domain particle can be seen. In Figure 6.9 this portion of the figure is more closely examined. The MFM signature appears to

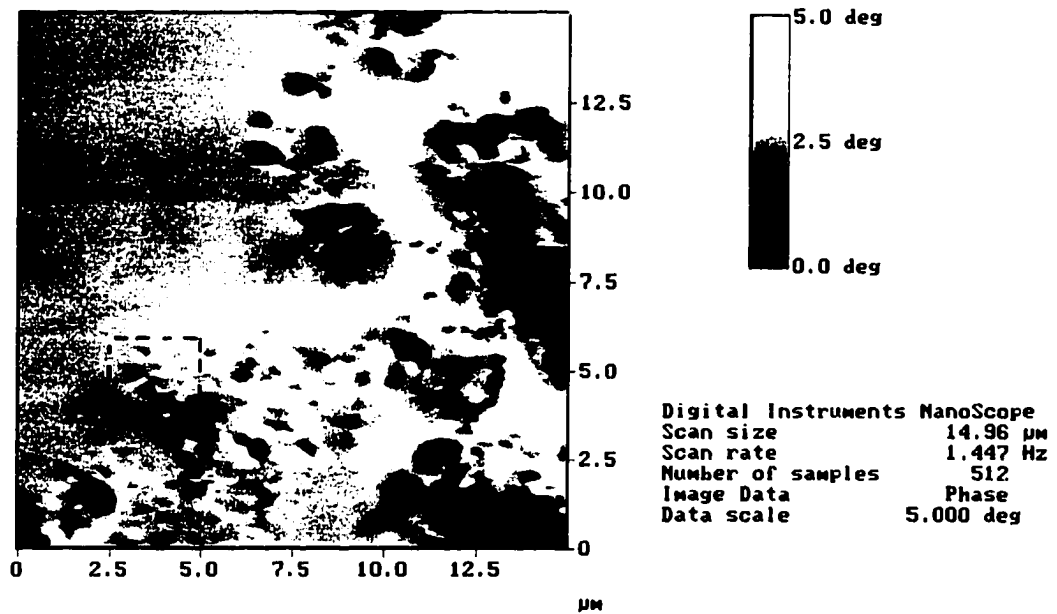


Figure 6.7: Magnetic force image of 20% Fe Vol. sample over  $15^2 \mu\text{m}^2$  area with 100 nm lift-off.

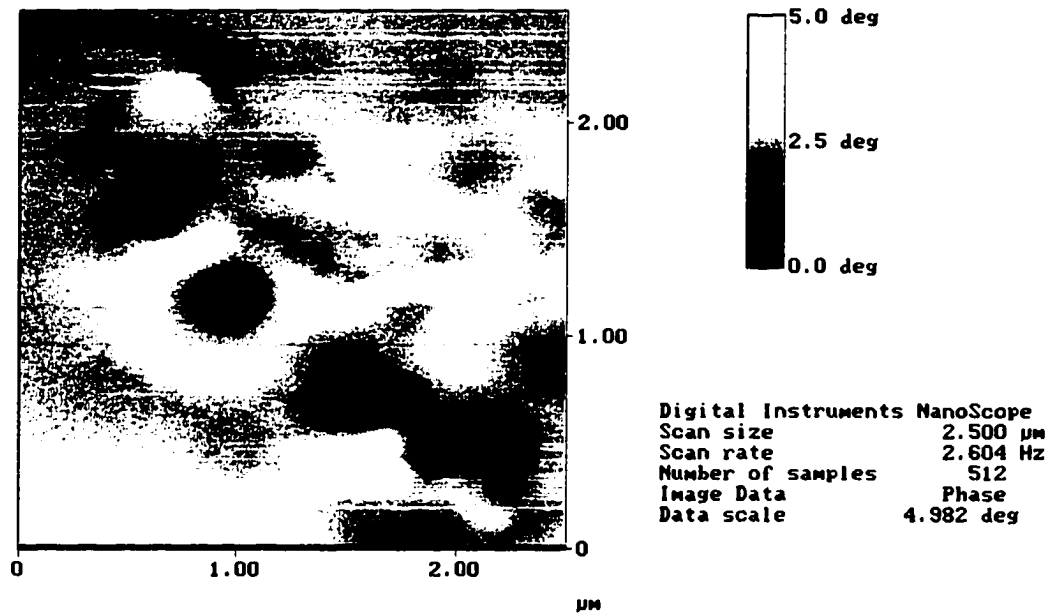


Figure 6.8: Magnetic force image of 20% Fe Vol. sample over  $2.5^2 \mu\text{m}^2$  area with 75 nm lift-off.

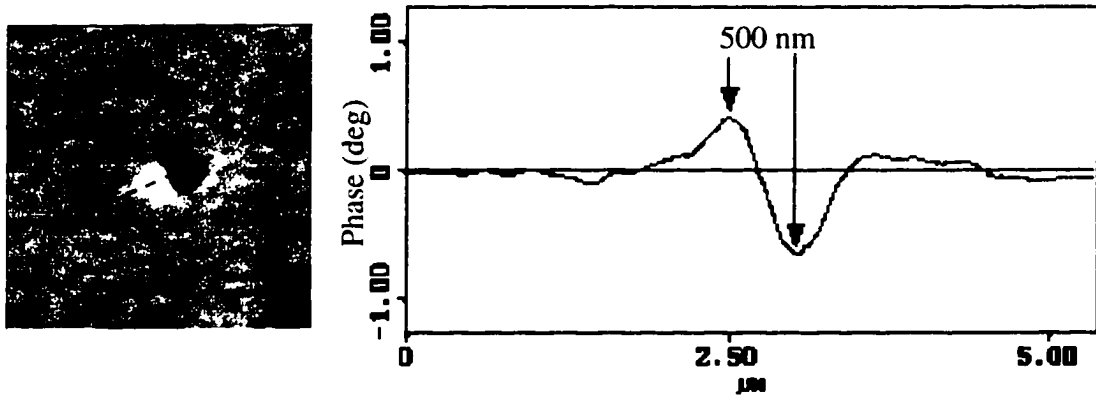


Figure 6.9: Magnetic force image and line scan across single particle identified in Figure 5.11.

be that of a single domain particle with magnetization parallel to the sample surface, as can be seen by comparison with Figure 5.5.

Figure 6.10 displays two separate line scans across the magnetic force data displayed in Figure 6.8. Several nanophase iron particles can be identified. Line 1 is drawn across a single particle with magnetization parallel to the sample surface. Line 2 is drawn so as to cross several particles. A particle with magnetization parallel to the surface can be identified in the upper right hand corner, at  $1 \mu\text{m}$  on the line. A particle with magnetization perpendicular to the surface (as depicted in Figure 5.4) follows immediately, at approximately  $1.4 \mu\text{m}$ . Continuing along line 2, a more complicated multi-component pattern consistent with that of a multidomain particle [54] is observed starting at about  $1.8 \mu\text{m}$ .

It can be assumed that electron flow along paths such as highlighted in line 2 of Figure 6.10 will contribute to the electronic conduction of the iron polyimide composites fabricated with iron volume fractions near the percolation threshold. In chapters 2-4 it was theorized that conduction along such paths will result in tunneling magnetoresistance and variable range hopping phenomena. The experimental verification of these conduction mechanisms is presented in the following sections. First,

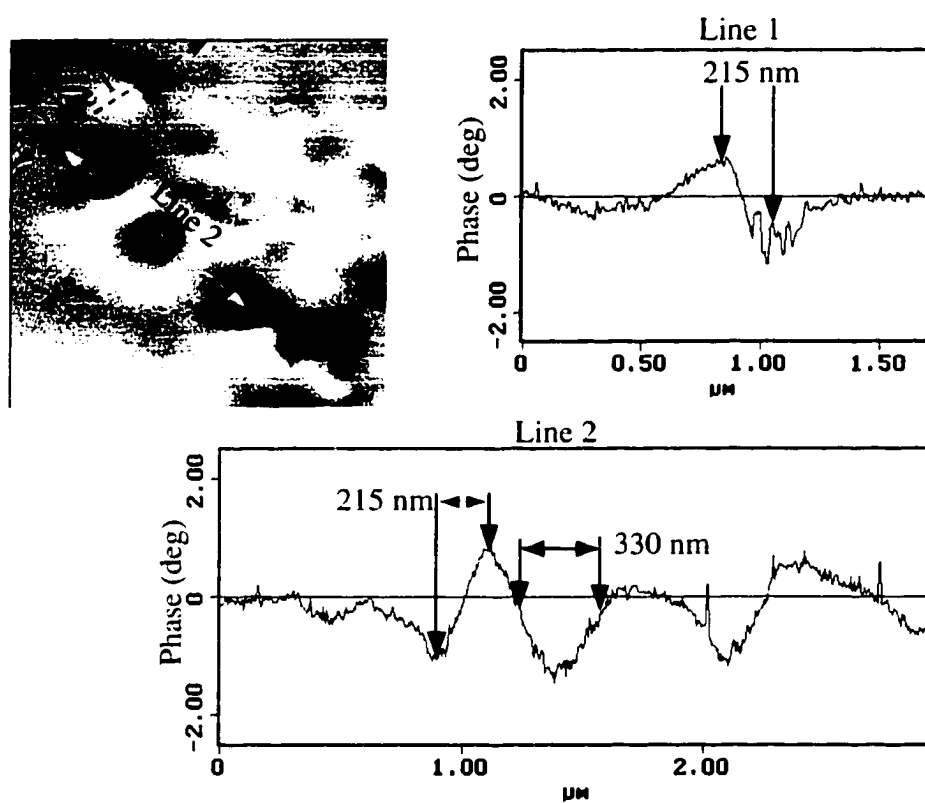


Figure 6.10: Identification of closely spaced nanophase iron particles in iron polyimide composite with 20% Fe Vol.

however, the bulk magnetic properties of the composite materials are examined.

## 6.2 Magnetization Data

The magnetization curves for iron polyimide samples with Fe Vol. fractions of 0.15, 0.20, 0.23, 0.34, 0.44, 0.54, and 0.64 are displayed in Figure 6.11. The applied field axis has been corrected by the demagnetization field within the cubic samples, with  $H_d$  estimated as that of a sphere,  $H_d = \frac{4\pi}{3}M$ . The figure also contains data acquired on a 0.99999 iron thin sheet magnetized along the long axis. The demagnetization field is taken as zero for this sample. The curves are typical of a soft magnetic material, with the saturation magnetization increasing with amount of iron in the composite. A complete hysteresis loop for the 20% Fe vol. sample is displayed in Figure 6.12. An insert in the figure displays the low field region of the curve.

Table 6.1 lists the measured saturation magnetization, remanence, and coercivity of the samples used in this study. As discussed above, the saturation magnetization increases roughly linearly with the volume percentage of iron in the composite. The remanence of the composite samples also displays an increasing trend with percentage iron. The coercivity, however, appears to be nearly independent of the iron volume concentration, with only a slight trend of decreasing coercivity with volume concentration observed. All of the composite samples have a coercivity in the range  $16 \leq H_c \leq 20$ . An invariance of coercivity with packing fraction is predicted if the magnetic hardness is dominated by crystal anisotropy, as is the case with spherical iron particles. Shape anisotropy dominated coercivity, on the other hand, leads to a decreasing coercivity with increasing volume fraction [55]. The data presented in Table 6.1 suggest that the dominant factor for the iron polyimide composites of this study is crystal anisotropy and secondarily shape anisotropy. This can be explained by the presence of elongated or flattened iron particles intermixed with mostly spher-

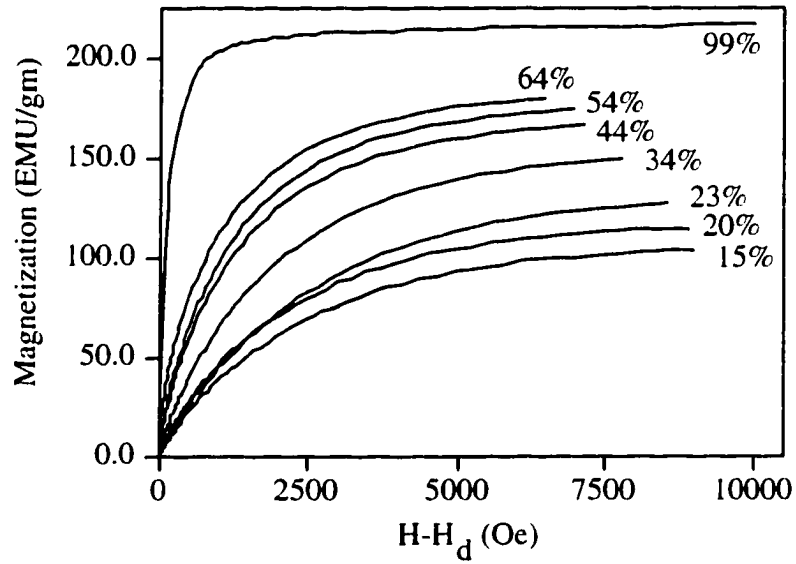


Figure 6.11: Magnetization curves for iron polyimide composite samples with varying Fe volume percentage.

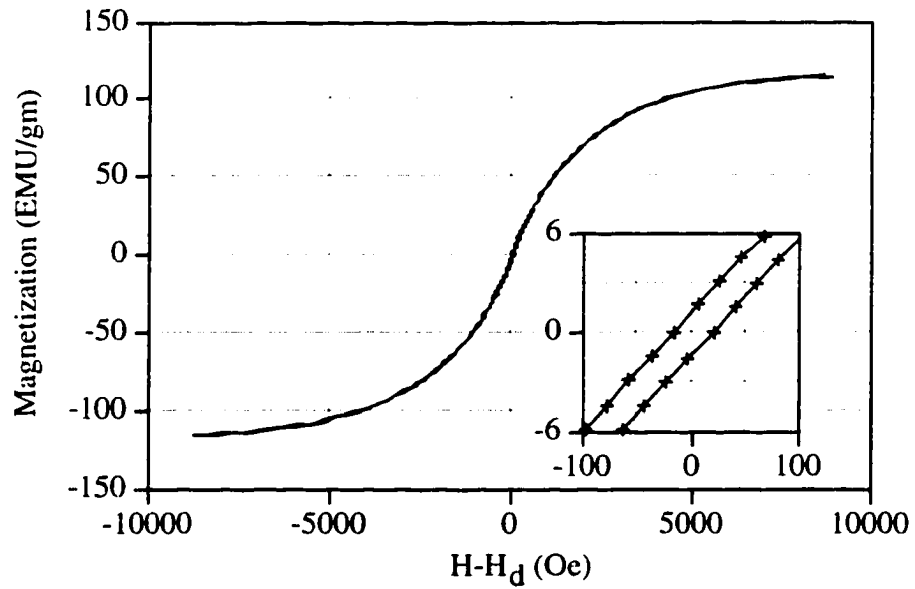


Figure 6.12: Hysteresis loop for 20% Fe Vol. composite sample.

Table 6.1: Magnetization data of iron polyimide composites with varying Fe volume concentration.

Fe Vol. %	$M_s$ (EMU/gm)	$M_r$ (EMU/gm)	$H_c$ (Oe)
15	104	1.15	20
20	115	1.23	18.5
23	127	0.95	15.8
34	150	2.10	18.0
44	166	4.00	17.6
54	175	4.25	16.0
64	180	10.7	16.6
100	217	3.85	3.20

ical ones. Such a mixture of iron particles is evidenced in the microscopy data of section 6.1.

### 6.3 Magnetoresistance Data

Table 6.2 lists the room temperature resistivity and the magnetoresistance at 0.5 Tesla,  $(R_{0.5} - R_0)/R_0$ , of iron polyimide composite samples manufactured with 0.15, 0.20, 0.23, 0.28, 0.34, and 0.64 Fe Vol. fraction. The table also contains reference data for a pure iron sample. Considerable sample to sample variation in the resistivity is observed for samples with low iron volume concentrations. The conduction path for these samples is along the meandering networks of particles as depicted in Figures 6.1 and 6.2. A uniform current flow across the sample does not exist, such that the placement of the probe leads can dramatically alter the measured resistance. The meandering networks of particles also appears to allow the sample to remain conducting well below the predicted percolation threshold. As the volume percentage increases beyond the percolation threshold the resistivity drops dramatically and becomes much more stable as continuous direct conduction paths across the sample are formed along with an accompanying uniform current flow.

Table 6.2: Room temperature resistivity and magnetoresistance at 0.5 Tesla of iron polyimide composite samples.

Fe Vol.%	Resistivity (Ohm-m)	Magnetoresistance $(R_{0.5} - R_0)/R_0$
15	6.1 : 3.7	-0.03 : -0.027
20	10.0 : 16.7 : 2190	-0.041 : -0.034 : -0.031
23	2.04 : 5.1	-0.021 : -0.020
28	$2.49 \times 10^{-2}$	-0.008
34	$2.78 \times 10^{-4}$	-0.0018
64	$9.28 \times 10^{-7}$	+0.0012
100	$9.61 \times 10^{-8}$ [56]	+0.003 [57]

In terms of the magnetoresistance, all samples with Fe Vol. % less than 64% show a negative magnetoresistance associated with spin dependent tunneling through insulating polyimide barriers. Figure 6.13 displays the magnetoresistance of the samples normalized to the resistance in the demagnetized state. A peak in the negative magnetoresistance is recorded for the 20% sample. In section 4.2 the percolation threshold for hexagonal close packing of iron particles was calculated as 20.1 %  $\pm$ 0.6%. The experimental data in Figure 6.13 and Table 6.2 can then be interpreted as showing a peak in the magnetoresistance at the percolation threshold of the system.

The peak value of the magnetoresistance in the iron polyimide composites, 4.1%, is consistent with the expected TMR for a randomly mixed iron insulator system at the percolation threshold. In section 4.4 the theoretical TMR for granular iron insulator system at the percolation threshold was calculated as 6.7%. Many possible sources can account for a lower experimental value than theoretically predicted, including spin flip scattering [9], parallel conduction paths [58], and band structure effects at the surface of the ferromagnetic particles [5]. It should be noted that a large variation in the calculated results is possible based upon the choice of the effective ferromagnet-barrier spin polarization, as discussed in section 4.4. In section 2.4 it was shown that along with the band structure of the ferromagnetic material, both

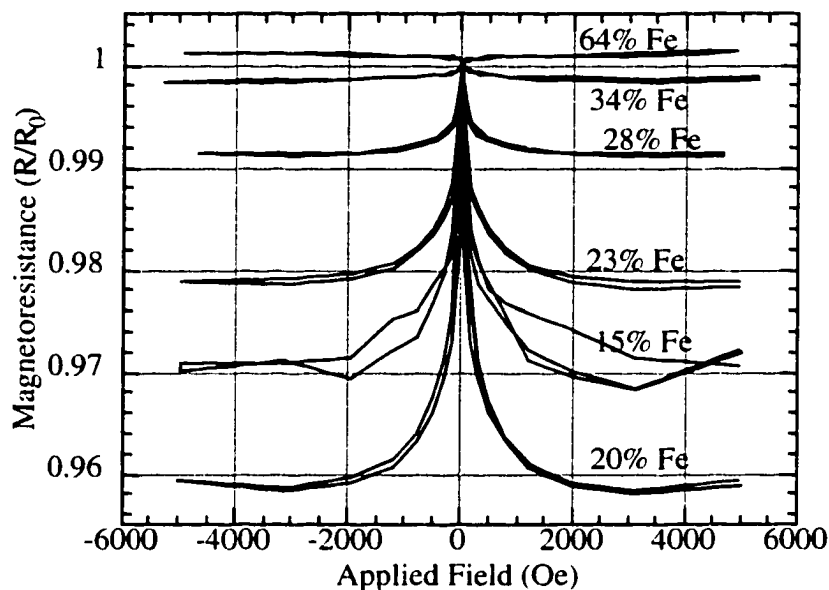


Figure 6.13: Magnetoresistance curves for iron polyimide composite samples.

the barrier height and thickness strongly effect the effective polarization. The quoted results were calculated assuming a value of  $P_{fb}^2 = 0.07$ .

Once the iron volume percentage increases above the predicted percolation threshold of 20% a portion of the conduction is expected to occur through connected paths which do not contain tunneling gaps. The presence of these connected paths greatly enhances the conductivity of the samples and reduces the net TMR effect. These percolating paths are responsible for the drop in TMR beyond 20% as displayed in Figure 6.13 and Table 6.2. As the percentage of iron in the sample continues to increase more connected paths appear and a transition to bulk ferromagnetic behavior occurs. In most bulk ferromagnets an increase in the resistance is observed as the angle between the current and the magnetic saturation direction of any domain decreases. This anisotropic magnetoresistive (AMR) is due to spin-orbit coupling which causes the electron cloud about each nucleus to deform slightly as the magnetic saturation direction rotates. The deformation of the electron cloud produces an increased

scattering of the conduction electrons traveling across the lattice, thereby increasing the resistance [57]. A transition between negative tunneling magnetoresistance and positive bulk anisotropic magnetoresistance is observed as the iron volume percentage increases from 34% to 64%.

The experimental work and interpretation presented above is consistent with the work of Milner and Gerber [11, 12] on granular thin film iron-insulator systems. These authors found a peak magnetoresistance of about 0.6% and 4.5% for  $\text{Ni}_x(\text{SiO}_2)_{100-x}$  and  $\text{Co}_x(\text{SiO}_2)_{100-x}$  respectively at  $x \approx 0.46$  for the Ni and  $x \approx 0.41$  for the Co systems. In this work the samples were prepared by coevaporation of the starting materials using two independent electron beam guns. The samples had dimensions of 8 x 2 mm with a thickness of 100 nm. In calculating the percolation threshold it is reasonable to assume a two dimensional system. In section 4.1 the percolation threshold for a trigonal lattice was calculated as 0.5, in agreement with the known exact value. The data can therefore be interpreted as showing a peak in the magnetoresistance at a volume fraction just below the percolation threshold of the system, a common phenomena in granular TMR systems.

A plot of the magnetization and magnetoresistance for the 20% Fe sample is given in Figure 6.14. As predicted, the resistance is a maximum in the initial demagnetized state. The application of an external field causes the electron spin directions to gain coherence as they rotate toward the direction which minimizes the Zeeman energy. As described in chapter 2 and given in equation (2.14),  $G = G_{fbf}(1 + P_{fb} \cos \theta)$ . The conductance across a tunneling gap is proportional to the cosine of the angle between the spin vectors of the neighboring ferromagnets. Coherence in the electron spins across the sample therefore results in a reduced resistance as the magnitude of  $\theta$  decreases. The resistance continues to drop with increasing field into magnetic saturation where the minimum resistance is observed. Reducing the external field strength now brings the sample out of saturation, increasing the average

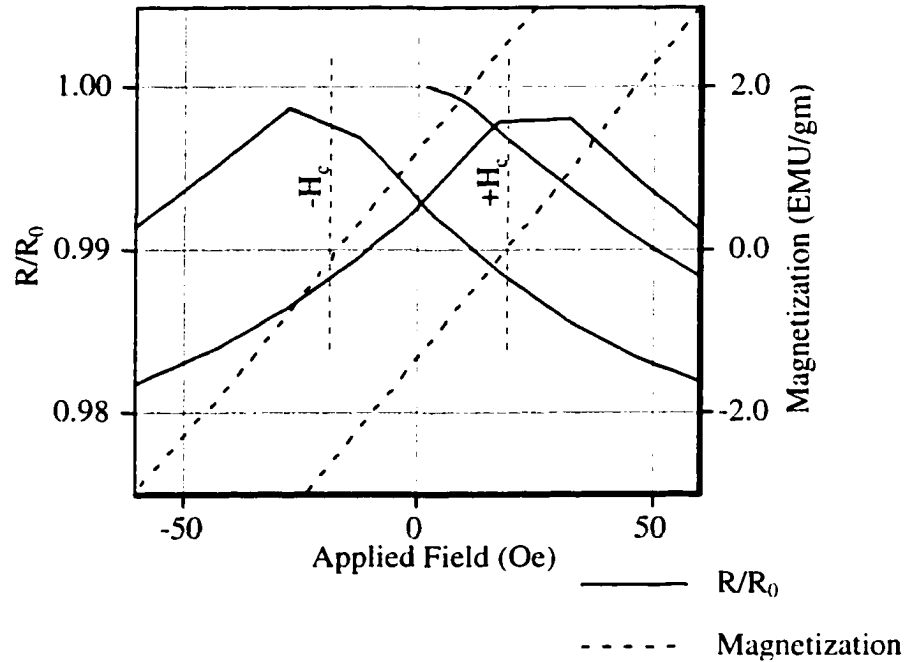


Figure 6.14: Magnetization and magnetoresistance for 20% Vol. Fe composite sample.

angle between the spin direction on neighboring particles. The resulting increase in resistance is apparent in Figure 6.14. The hysteresis effects are also quite clear, with the peak resistance of the sample occurring at the positive and negative coercive fields as the sample is cycled through the hysteresis loop.

## 6.4 Variable Range Hopping

Figure 6.15 displays the temperature dependence of the resistivity for composite samples fabricated with 0.20, 0.23, 0.28, 0.34, 0.44, and 0.64 Fe vol. fractions. The plot also shows reference data for pure iron [56]. As noted previously, the room temperature resistivity drops dramatically as the iron volume concentration increases beyond the percolation threshold. Figure 6.15 shows that the temperature coefficient of the resistivity also changes sign as the percolation threshold is crossed.

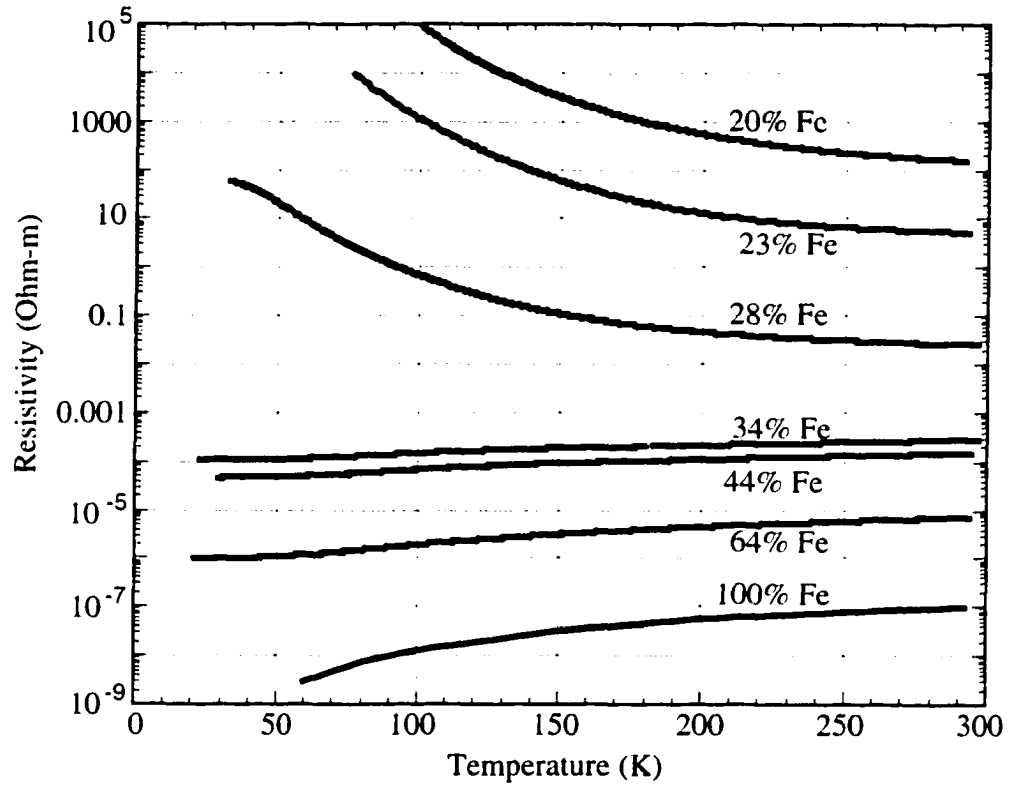


Figure 6.15: Resistivity versus temperature for iron polyimide composite samples.

In the samples with iron concentrations beneath the percolation threshold conduction across the sample must occur through insulating tunneling gaps. In section 3.3 conduction across such a system through variable range hopping was described. For small particles thermal activation is required to overcome the charging energy for adding an electron to an isolated metallic grain. The existence of a distribution of particle sizes throughout the matrix then leads to an optimum temperature dependent tunneling distance and a resistivity of the form  $\ln \rho \propto T^{-\nu}$ , with  $1/4 \leq \nu \leq 1/2$ .

The microscopy studies described in sections 5.2, 5.3, and 6.1 have confirmed the existence of a large variation in iron particle size down into the nanometer regime. The resistivity data for samples near the percolation threshold is therefore expected to obey the theory summarized above and detailed in Chapter 3. In Figure 6.16 the experimental data for the 20% sample is fit to this theoretical model. The curve fit contains a constant term independent of the temperature to account for the nearly temperature independent resistance across large iron clusters. In the plot every tenth experimental point is shown along with a solid line for the curve fit. The experimental results are seen to fit well to a  $T^{-1/2}$  dependence, in agreement with the theory.

Experimental measurements of hopping conduction performed by several other authors support the results presented here. Sheng et al., for example, found  $\ln \sigma \propto -T^{-1/2}$  for  $\text{Ni}_x(\text{SiO}_2)_{100-x}$  with  $.08 \leq x \leq .44$  over a temperature range  $16 \leq T(\text{K}) \leq 400$  [14]. Roth's work with electrically conducting polymers found that the exponential factor could not be precisely determined, with the experimental data fitting well to  $\ln \rho \propto T^{-\nu}$  over the range  $1/4 \leq \nu \leq 1/2$  [15].

The transition between phonon assisted hopping conduction and metallic type conduction occurs between 28% and 34% iron volume percent. All the samples with iron volume fractions greater than 30% display a positive coefficient of resistivity with increasing temperature. This temperature dependence is well understood in terms of electron-phonon scattering in the metal [59].

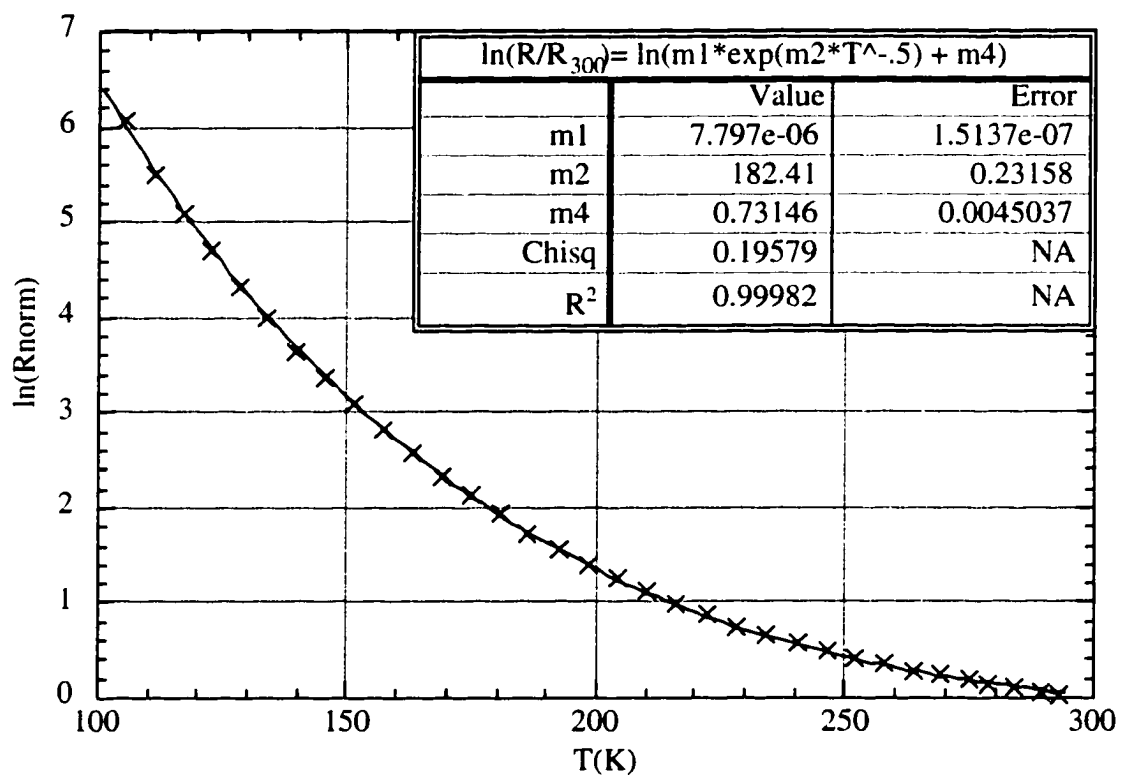


Figure 6.16: Curve fit of the temperature dependence of resistivity for 20% iron sample.

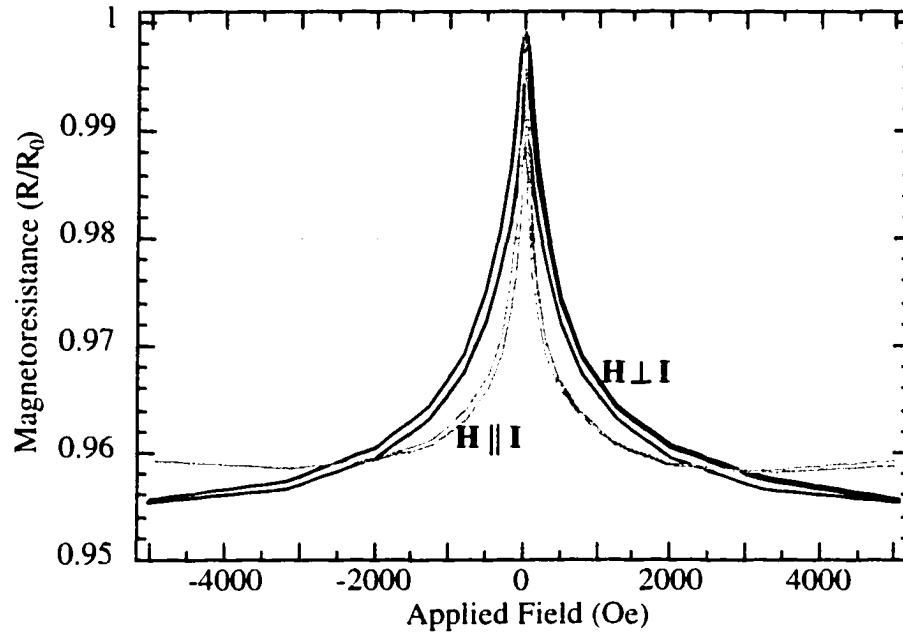


Figure 6.17: Effect of sample orientation on measured magnetoresistance.

## 6.5 Temperature Dependence of Magnetoresistance

The previous section showed that the transport properties of iron polyimide composites are highly temperature dependent. Samples with iron volume fractions near the percolation threshold display an increase in resistivity of 2-3 orders of magnitude as the temperature is lowered from room temperature to 100 Kelvin. In this section the temperature dependence of the magnetoresistance is analyzed.

As discussed in the previous chapter, the sample orientation was changed between the room temperature magnetoresistance measurements performed in air and the variable temperature measurements taken within the cryostat. A comparison of the in-air measurements with those taken at room temperature within the cryostat, displayed in Figure 6.17, shows the effect of sample orientation on the measured magnetoresistance. The in-air data, with the magnetization along the long axis and parallel to the current direction, shows a rapid drop in the resistance at low fields. As

the applied field magnitude increases beyond approximately 3 kOe a slight increase in the resistance is detected. This increase in the resistance appears to be due to the anisotropic magnetoresistive (AMR) effect [57], described in section 6.3. For parallel alignment of the current and magnetic field the effect is observed as a slight increase in the resistance at high fields, where the larger GMR is near saturation. The data acquired for the sample in the cryostat, with the applied field perpendicular to the current flow, does not show any increase in the resistance. With this orientation, however, the demagnetization field is much larger. A correspondingly larger applied field is therefore required to achieve the same sample magnetization as compared to the parallel alignment. The resulting data for the perpendicular magnetization displays a slower drop in the resistance with applied field but a larger GMR in the high field region due to the absence of positive AMR.

Magnetoresistance data was acquired on the 20% iron sample at temperatures of 295, 175, and 130 Kelvin. The temperature setpoint was programmed into the temperature controller and the system allowed to reach equilibrium before data acquisition was initiated. The temperature and heating element current were monitored during each magnetization cycle to verify that the applied field did not effect the temperature control circuitry.

Figure 6.18 displays the effect of the sample temperature on the magnetoresistance of the 20% Fe sample. The change in resistance is seen to increase with decreasing temperature, from approximately 4.4% at 295 K to 6.6% at 130 K. Note that, as shown in Figure 6.15,  $R_0$  for the sample increases nearly two order of magnitude over this temperature range. The experimental equipment was limited to a maximum resistance measurement of  $2 M\Omega$ , which precluded the acquisition of data at lower temperatures.

A decrease in the magnetoresistance of ferromagnet-insulator-ferromagnet systems with increasing temperature has been observed in the past [7, 9, 10, 58, 60]. A

theoretical basis for the effect described by Shang et al. attributes the temperature dependence to a temperature dependence in the electron polarization given by  $P \propto (1 - \alpha T^{3/2})$  [58]. At temperatures well below the Curie temperature the excitation of spin waves is known to reduce the spontaneous magnetization from its saturation value by an amount proportional to  $T^{3/2}$ . This temperature dependence of the magnetization is known as the Bloch  $T^{3/2}$  law [61], and is the basis for the  $T^{3/2}$  dependence in the Shang polarization term [58]. Increasing the temperature results in a lower magnetization (polarization) which, by equation (2.3), reduces the conductance ratio. Although the cited works are for thin film multilayer systems, a similar mechanism appears to occur in the granular composite samples of the present study. This mechanism is independent of the temperature dependence of the resistivity, discussed in the previous section.

## 6.6 Material Processing Results

The saturation magnetization, remanence, and coercivity of 20% iron powders ball milled for 0, 1, 2, 3, 4, and 8 hours are listed in Table 6.3. The data show a strong trend of increasing coercivity with ball milling time. A similar increase in coercivity with milling time was observed by Giri in iron-polyethylene samples and attributed to the creation of single domain iron particles strongly bonded to the polyethylene matrix [38]. The increasing coercivity with milling time in the present study is believed to be due to the same mechanism.

It is known that the coercivity of fine particles increases with decreasing size, reaching a maximum at the critical size for the formation of single domain particles [55]. As discussed in section 6.1, the critical diameter for spherical iron particles has been estimated as  $\approx 30$  nm [52, 53]. High energy ball milling reduces the average particle size toward this critical diameter, thereby increasing the coercivity toward

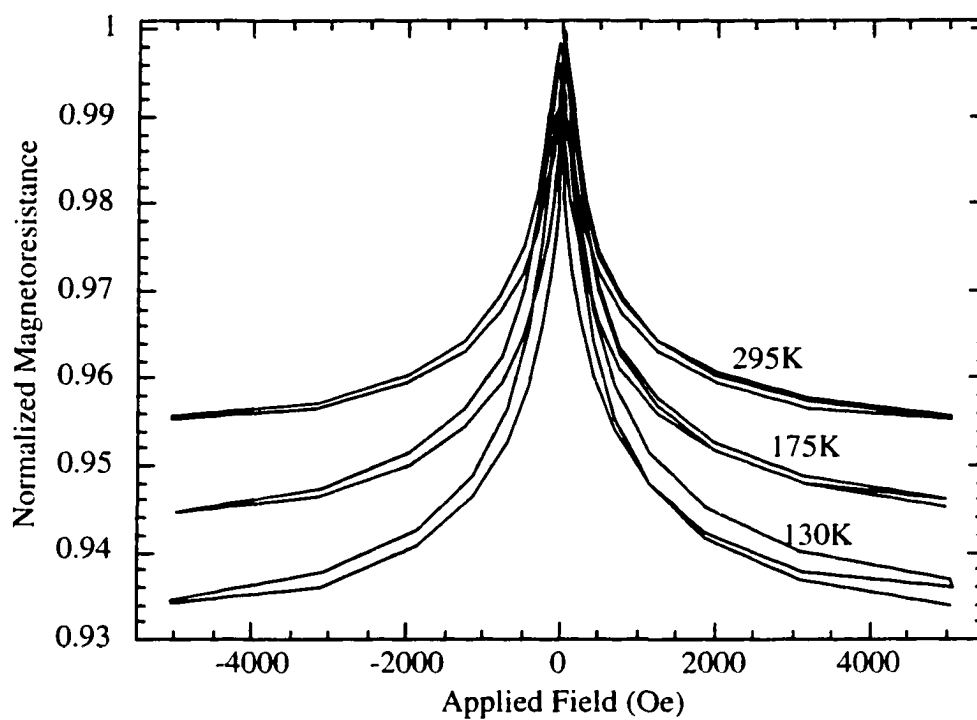


Figure 6.18: Temperature dependence of magnetoresistance for iron polyimide composite with 20% Fe Vol.

Table 6.3: Magnetization data of 20% iron powders with varying ball milling times.

Milling Time (hr)	$M_s$ (EMU/gm)	$M_r$ (EMU/gm)	$H_c$ (Oe)
0	115	1.23	18.5
1	125	1.41	21.4
2	128	1.94	23.4
3	116	1.88	27.5
4	113	2.35	32.4
8	112	3.12	44.7

its maximum value. The intrinsic coercivity of spherical single-domain iron particles with easy axes aligned with the field is  $2K/M_s = 2(4.8 \times 10^5)/1714 = 560$  Oe [52].

Microscopy studies on the milled composites revealed a dramatic change in the particle distribution as compared to samples fabricated from unmilled powders. Figure 6.19 compares an unmilled 20% iron composite and a 20% sample milled for 8 hours. An increase in the number of the smallest particles reduces the average particle size in the milled sample. In addition, a striking change occurs in the distribution of the iron particles throughout the composites. High energy ball milling of the iron and polyimide powders destroys the chain-like networks of iron particles across the sample. This redistribution of the iron particles was observed in all samples studied.

In section 6.3 the chain like conduction paths of the unmilled composite samples were found to allow electron flow at volume concentrations beneath the anticipated percolation threshold. The room temperature resistivity was shown to remain nearly unchanged for samples between 0.15 and 0.23 iron volume fractions, with considerable sample to sample variation for the 0.15 and 0.20 samples. Initial results suggest that the redistribution of the iron particles with high energy ball milling significantly effects the electron transport across the samples. The ball milled samples become insulating very near 20% iron volume concentration. Indeed, the very high resistance of the sample ball milled for 4 hours precluded data acquisition with the LR700 AC resistance bridge. The sample milled for 8 hours showed a significantly lower

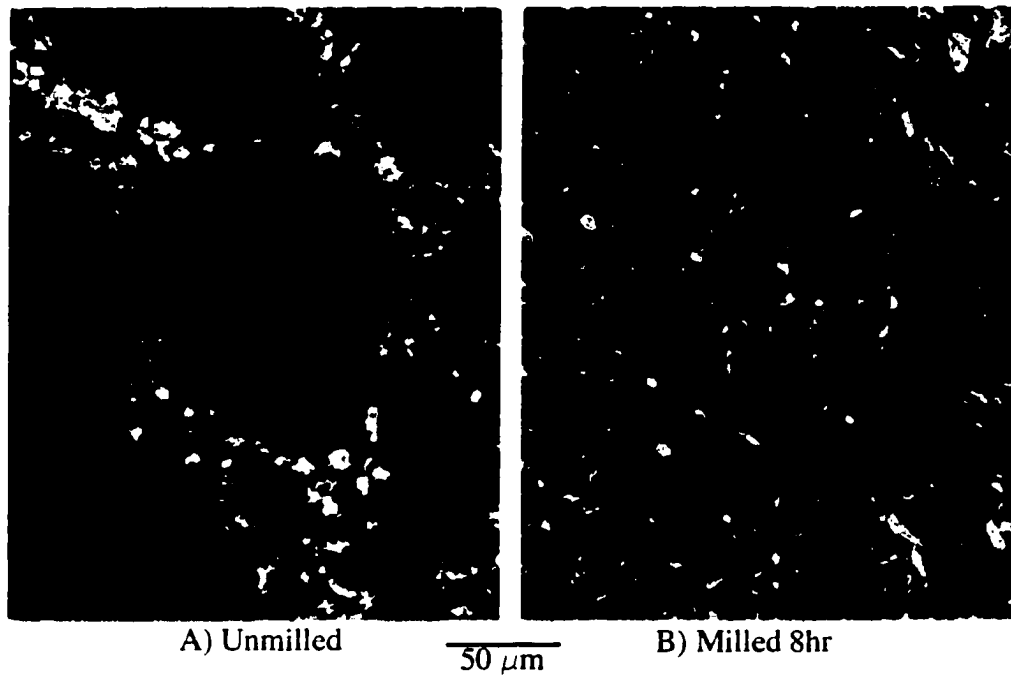


Figure 6.19: Optical micrographs of milled and unmilled 20% Fe composite samples.

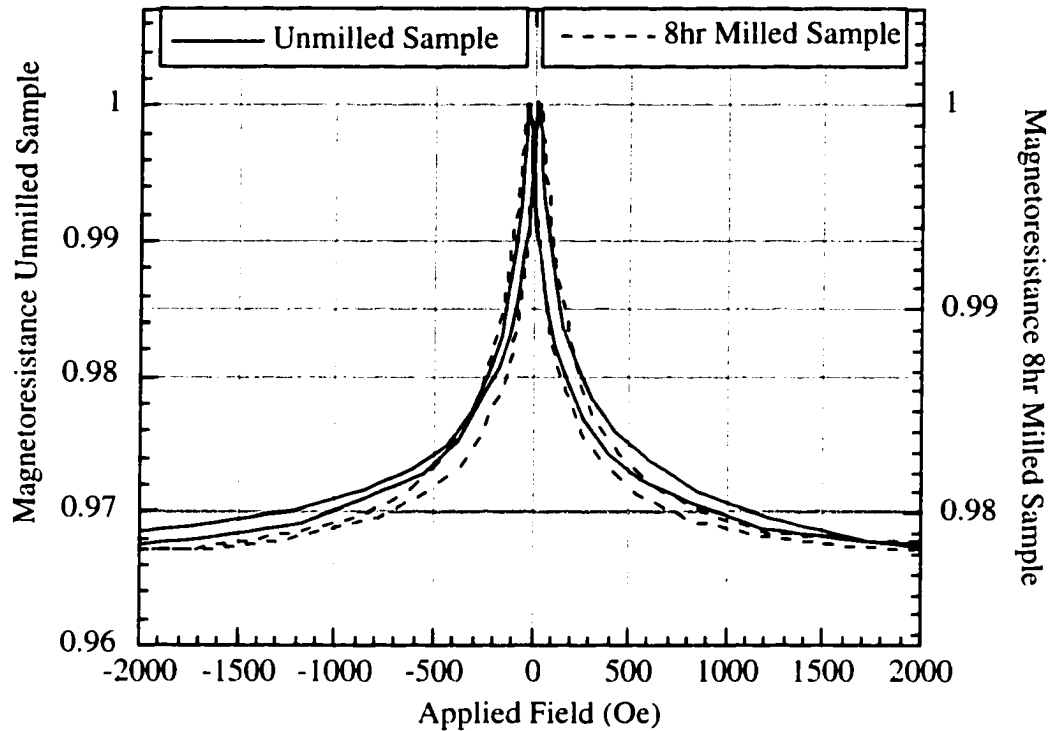


Figure 6.20: Magnetoresistance of milled and unmilled 20% Fe composite samples.

resistance, believed to be due to a slightly larger iron volume concentration caused by experimental variation in the sample preparation procedure. The density of the 4 hour and 8 hour samples was found to be 2.665 gm/cc and 2.679 gm/cc, corresponding to 19.9% and 20.1% iron volume percentages respectively.

Magnetoresistance measurements on the 8 hour sample found a TMR of 2.5% at 0.5 Tesla. Figure 6.20 displays the experimental results for the magnetoresistance of the 8 hour milled sample in comparison with the unmilled 20% sample. The vertical scale for the two plots has been changed to emphasize the overall shape of the magnetoresistance curves.

In Figure 6.21, the low field region of the data plotted in Figure 6.20 is examined. The higher coercivity of the milled sample produces a shift in the resistance peaks toward higher field levels. As discussed in section 6.3, the resistance increases

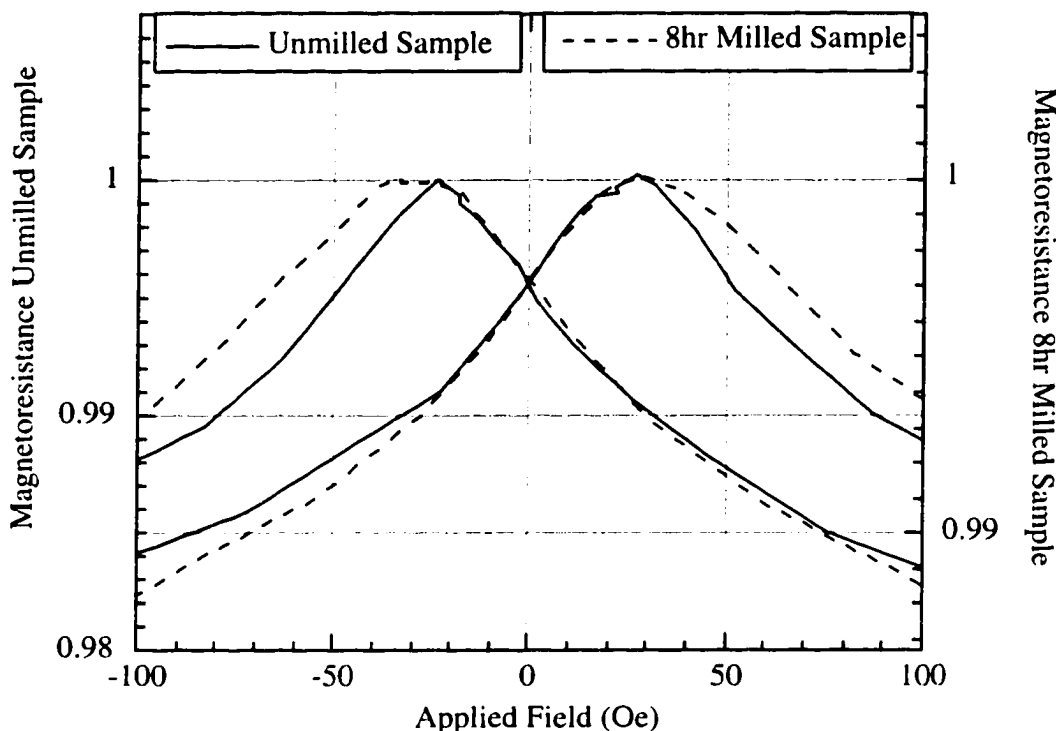


Figure 6.21: Low field magnetoresistance of milled and unmilled 20% Fe composite samples.

as the sample is taken out of saturation until the positive/negative coercive field is reached. A decrease in average particle size and an increase in the particle size distribution results in broader resistance peaks at higher field levels for the milled sample.

The 2.5% TMR of the milled sample is significantly lower than that found in the 20% unmilled sample. The redistribution of the iron particles, as shown in Figure 6.19, is expected to alter the percolation threshold of the system. The maximum TMR may then occur at a volume concentration shifted from the unmilled studies. It is anticipated that a peak in the TMR of the milled samples will occur at a slightly higher volume concentration, accounting for the loss of the meandering particle networks seen in the unmilled samples. A detailed experiment to more fully investigate the

magneto-resistance versus volume percent for milled samples is being planned. In this future study the volume fraction of iron will be controlled to 0.1% or better in the vicinity of 20%.

# Chapter 7

## Summary and Conclusions

### 7.1 Summary

Research in the area of tunneling magnetoresistance has grown rapidly in recent years due to potential magnetic sensor and digital storage applications. It has been shown that the tunneling current across a ferromagnet-insulator-ferromagnet system is strongly dependent upon the relative magnetization direction of the two ferromagnets. An external field causes the magnetization directions of the ferromagnets to align and results in a characteristic drop in the resistivity of the junction.

In this dissertation a new method for the fabrication of TMR materials via compression molding of powdered ferromagnetic iron with a high performance polyimide has been introduced. The procedure can be used to produce bulk TMR samples at low cost from commercially available raw materials. It has been shown that the percent change in the resistance with applied magnetic field depends critically on the volume percentage of ferromagnetic material in the composite. A peak in the TMR occurs at a volume concentration just beneath the percolation threshold of the ferromagnetic material. The highest recorded room temperature conductance ratio for the iron poly-

imide composites is -4.5% at 20% iron volume concentration, increasing to -6.5% at 130 Kelvin. This conductance ratio is lower than has been achieved in thin film multilayers fabricated through cryogenic evaporation techniques [10], but is comparable to other granular TMR systems fabricated through coevaporation of ferromagnetic and insulating materials using two independent electron beam guns [11, 12]. The ease of sample fabrication and lowered production costs of the compression molded composites described here may make them advantageous for many applications. In addition, future work described below has potential to enhance the TMR of the compression molded composites, reducing the sensitivity gap versus the more exotic thin film materials.

Along with tunneling magnetoresistance, iron polyimide composites near the percolation threshold were found to exhibit variable range hopping (VRH) conduction. A temperature dependence of the conductivity of the form  $\ln \sigma \propto -T^{-1/2}$  was observed for iron polyimide composites with iron volume fractions near the percolation threshold. The strong temperature dependence resulted in an increase in the resistivity of several orders of magnitude as the temperature was lowered from room temperature to 100 Kelvin. This instability of the resistance with varying temperature may limit the application of the material for magnetic storage or sensor applications. Any future applications of the material will need to incorporate this strong temperature dependence of the resistivity into the measurement scheme.

A theoretical model describing the electronic transport in iron polyimide composites has been developed in this work. The model predicts the observed tunneling magnetoresistance and hopping conduction in systems fabricated near the percolation threshold of the ferromagnetic material. A computer simulation incorporating the theoretical models has also been developed and used to successfully predict the percolation threshold and conductance ratio of the composites.

## 7.2 Future Perspectives

Further development in the research of compression molded TMR materials should be concentrated on optimizing desirable transport properties based upon the theoretical models presented in this work. In particular, improvements in the conductance ratio of the TMR could be used to develop the composites into useful electronic materials. Material processing through high energy ball milling, described in sections 5.7 and 6.6, is a first attempt at improving the TMR based upon model predictions. Along with continuation of this work, the extension of the sample fabrication for other ferromagnetic materials is planned. Mechanical alloying and systems with more than one ferromagnetic material may greatly enhance the TMR of the composite materials.

Further development of the theoretical models and computer simulation are also needed to optimize desirable transport properties. A better determination of the band structure at the surface of the ferromagnetic material and the barrier height of the polyimide is required in order to improve the accuracy of the models. The computer simulation can also be greatly enhanced. Simulations incorporating the combined effect of contact conduction and tunneling channels in a full three dimensional lattice could enhance the development of new electronic materials based upon ferromagnet-polyimide composite systems.

# Bibliography

- [1] M. Plischke and B. Bergersen, *Equilibrium Statistical Physics*, World Scientific, Singapore, 1994.
- [2] M. Julliere, Phys. Lett. **54A**, 225 (1975).
- [3] M. Stearns, JMMM **5**, 167 (1977).
- [4] J. Slonczewski, Phys. Rev. B **39**, 6995 (1989).
- [5] J. MacLaren, X. Zhang, and W. Butler, Phys. Rev. B **56**, 11827 (1997).
- [6] Y. Qi, D. Xing, and J. Dong, Phys. Rev. B **58**, 2783 (1998).
- [7] J. Moodera, L. Kinder, T. Wong, and R. Meservey, Phys. Rev. Lett. **74**, 3273 (1995).
- [8] K. Inomata, K. Tusu, and Y. Saito, Phys. Rev. Lett. **74**, 1863 (1995).
- [9] J. Moodera and L. Kinder, J. Appl. Phys. **79**, 4724 (1996).
- [10] J. Moodera, J. Nowak, and J. van de Veerdonk, Phys. Rev. Lett. **80**, 2941 (1998).
- [11] A. Milner, A. Gerber, B. Groisman, M. Karpovsky, and A. Gladkikh, Phys. Rev. Lett. **76**, 475 (1996).

- [12] A. Gerber, A. Milner, B. Groisman, M. Karpovsky, and A. Gladkikh, *Phys. Rev. B* **55**, 6446 (1997).
- [13] R. Bryant, *High Perform. Polym.* **8**, 607 (1996).
- [14] P. Sheng, B. Abeles, and Y. Arie, *Phys. Rev. Lett.* **31**, 44 (1973).
- [15] S. Roth, Hopping conduction in electrically conducting polymers, in *Hopping Transport in Solids*, edited by M. Pollak and B. Shklovskii, pages 377–395, Elsevier Science Publishers B.V, Netherlands, 1991.
- [16] P. Tedrow and R. Meservey, *Phys. Rev. Lett.* **26**, 192 (1971).
- [17] P. Tedrow and R. Meservey, *Phys. Rev. B* **7**, 318 (1973).
- [18] D. Papaconstantopoulos. *Handbook of the Band Structure of Elemental Solids*, Plenum Press, New York, 1986.
- [19] J. Sakurai, *Modern Quantum Mechanics*, Addison-Wesley Publishing Company, Inc., New York, 1985.
- [20] N. W. Ascroft and N. D. Mermin, *Solid State Physics*, Saunders College Publishing, New York, 1976.
- [21] R. Landauer, *IBM J. Res. Dev.* **1**, 223 (1957).
- [22] M. Büttiker, *IBM J. Res. Dev.* **32**, 317 (1988).
- [23] N. Mott, *Non-Cryst. Solids* **1**, 1 (1968).
- [24] T. Castner, Hopping conduction in the critical regime approaching the metal-insulator transition, in *Hopping Transport in Solids*, edited by M. Pollak and B. Shklovskii, pages 1–47, Elsevier Science Publishers B.V, Netherlands, 1991.

- [25] P. Sheng, Electronic transport in granular metal films, in *Nanophase Materials*, edited by G. Hadjipanayis and R. Siegel, pages 381–398, Kluwer Academic Publishers, Netherlands, 1994.
- [26] P. Anderson, *Phys. Rev.* **109**, 1492 (1958).
- [27] N. Mott, *Conduction in Non-Crystalline Materials*, Oxford University Press, New York, 1987.
- [28] N. Mott, *Metal-Insulator Transitions*, Taylor and Francis, New York, 1990.
- [29] N. Mott, *Phil. Mag.* **13**, 989 (1966).
- [30] M. Cohen, H. Fritzsche, and S. Ovshinsky, *Phys. Rev. Lett.* **30**, 699 (1969).
- [31] A. Miller and S. Abrahams, *Phys. Rev.* **120**, 745 (1960).
- [32] A. F. Efros and B. L. Shklovskii, *J. Phys.* **C1**, L49 (1975).
- [33] V. Ambegaokar, B. I. Halperin, and J. S. Langer, *Phys. Rev. B* **4**, 2612 (1971).
- [34] V. K. Shante, *Phys. Lett.* **43A**, 249 (1973).
- [35] P. Sheng and J. Klafter, *Phys. Rev. B* **27**, 2583 (1983).
- [36] A. Walton, *Network Analysis and Practice*, Cambridge University Press, Cambridge, 1987.
- [37] Alfa Aesar Research Chemicals, *Metals and Materials*, 1997, Stock No. 10214.
- [38] A. Giri, *J. Appl. Phys.* **81**, 1348 (1997).
- [39] T. Shen, C. Koch, T. Tsui, and G. Pharr, *J. Mater. Res.* **10**, 2892 (1995).

- [40] D. Halliday, R. Resnick, and J. Walker, *Fundamentals of Physics*, pages 452–453. John Wiley & Sons, Inc., New York, 1993.
- [41] M. Namkung, R. Bryant, B. Wincheski, and A. Buchman. *J. Appl. Phys.* **81**, 4112 (1997).
- [42] M. Namkung, B. Wincheski, R. Bryant, and A. Buchman. *J. Appl. Phys.* **83**, 6474 (1998).
- [43] J. Goldstein et al., *Scanning Electron Microscopy and X-Ray Microanalysis*. Plenum Press, New York, 1992.
- [44] S. Manalis, K. Babcock, J. Massie, V. Elings, and M. Dugas. *Appl. Phys. Lett.* **66**, 2585 (1995).
- [45] MultiMode, TappingMode, and LiftMode are trademarks of Digital Instruments. Tapping Mode and LiftMode. V. Elings and J. Gurley. U.S. Patent No. 5,266,801 and U.S. Patent No. 5,308,974. Digital Instruments, Santa Barbara, CA.
- [46] Digital Instruments, Santa Barbara, California 93103. *MultiMode<sup>TM</sup> Scanning Probe Microscope Instruction Manual*. 1996.
- [47] K. Babcock, V. Elings, M. Dugas, and S. Loper. *IEEE Trans. Magn.* **30**, 4503 (1994).
- [48] J. Jackson, *Classical Electrodynamics*, chapter 5, John Wiley & Sons, Inc., New York, 1975.
- [49] K. Babcock, V. Elings, J. Shi, D. Awshalom, and M. Dugas, *Appl. Phys. Lett.* **69**, 705 (1996).
- [50] B. Cullity, *Introduction to Magnetic Materials*, chapter Appendix 5, Addison-Wesley Publishing Company, Inc., New York, 1972.

- [51] K. Liu, J. Zhang, and G. Chen, *J. Mater. Res.* **13**, 1198 (1998).
- [52] B. Cullity, *Introduction to Magnetic Materials*, chapter 9, Addison-Wesley Publishing Company, Inc., New York, 1972.
- [53] A. Morrish, *The Physical Principles of Magnetism*, chapter 7, John Wiley & Sons, Inc., New York, 1965.
- [54] J. Shi, D. Awschalom, P. Petroff, and K. Babcock, *J. Appl. Phys.* **81**, 4331 (1997).
- [55] B. Cullity, *Introduction to Magnetic Materials*, chapter 11.3. Addison-Wesley Publishing Company, Inc., New York, 1972.
- [56] D. Lide, editor. *CRC Handbook of Chemistry and Physics*, pages 12-33. CRC Press Inc., Boca Raton, 1991.
- [57] B. Cullity. *Introduction to Magnetic Materials*, chapter 8.9. Addison-Wesley Publishing Company, Inc., New York, 1972.
- [58] C. Shang, J. Nowak, R. Jansen, and J. Moodera, *Phys. Rev. B* **58**, 2917 (1998).
- [59] N. W. Ascroft and N. D. Mermin, *Solid State Physics*, chapter 26, Saunders College Publishing, New York, 1976.
- [60] C. Tanaka, J. Nowak, and J. Moodera, *J. Appl. Phys.* **81**, 5515 (1997).
- [61] N. W. Ascroft and N. D. Mermin, *Solid State Physics*, chapter 33. Saunders College Publishing, New York, 1976.

# Vita

## Russell Arthur Wincheski

Born in Chicago, Illinois, March 6, 1967. Graduated from Oswego High School in Oswego, Illinois, June 1985. Graduated from College of William and Mary in Williamsburg, Virginia, May 1990 with B.S. in physics. During college the author participated in several research programs for undergraduates with the College of William and Mary and the National Aeronautics and Space Administration. After graduating from the College of William and Mary, the author continued research on electromagnetic nondestructive evaluation techniques for aerospace materials at the National Aeronautics and Space Administration's Langley Research Center. In August of 1996 the author entered the College of William and Mary as a graduate student in the Physics Department. Received M.S. in physics in December 1996 from the College of William and Mary and proceeded to work towards his PhD.